2^{39}_{68}

COMPARISON OF INPUT CURRENT SPECTRAL COMPONENTS
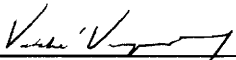
FOR FLYBACK PWM AND RESONANT CONVERTERS

by

Erik M. Kvalheim

Thesis submitted to the Faculty of the

Virginia Polytechnic Institute and State University

in partial fulfillment of the requirements for the degree of

Master of Science
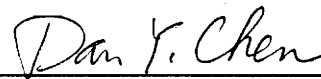
in

Electrical Engineering

APPROVED:

Fred C. Lee

F. C. Lee, Chairman

V. Vorperian   _Dan Y. Chen_

V. Vorpérian   D. Y. Chen

January 29, 1991

Blacksburg, Virginia

COMPARISON OF INPUT CURRENT SPECTRAL COMPONENTS

FOR FLYBACK PWM AND RESONANT CONVERTERS

by

Erik M. Kvalheim

F. C. Lee, Chairman

Electrical Engineering

(ABSTRACT)

Analytical expressions describing the input current spectrum of the flyback Pulse-Width-Modulated, Zero-Current-Switched Quasi-Resonant-Converter, and Zero-Voltage-Switched Quasi-Resonant-Converter are derived in terms of normalized circuit parameters. These analytical results are tested against experimental results. The same numerical example is presented for these three converters in which the input current spectrum is computed for various line/load conditions and the results are mutually compared. Detailed experimental results are presented for the same three converters as well as for the flyback Zero-Voltage-Switched Multi-Resonant-Converter. The effects of any parasitic oscillations in the experimental circuit are also considered.

" .... science is a cruel mistress"

The Big Blue (1988)

Acknowledgements

Table of Contents

List of Illustrations

List of Tables

Chapter 1

INTRODUCTION

One important aspect of designing switching power converters is the design of the input filter to sufficiently attenuate the pulsating current waveform in order to meet stringent electromagnetic interference requirements. To design an input filter properly, certain information needs to be known, such as, how much attenuation is needed over its input current spectrum? These types of questions were often addressed experimentally after a specific converter was built; however, it would be better to have mathematical expressions so that the input current spectrum could be considered in a more general way. In this thesis, analytical equations describing the input current spectrum for the PWM converters, Zero-Current-Switched Quasi-Resonant-Converters (ZCS-QRC), and the Zero-Voltage-Switched Quasi-Resonant-Converters (ZVS-QRC) using a flyback converter as an example. These expressions will be derived in terms of circuit parameters so that they can be used for different operating conditions. By deriving the equations in terms of circuit parameters, the effects of different operating conditions (for instance, line and load conditions) can be seen by examining the equations. All of the analytical results will be tested for accuracy against experimental results.

Also, since each of these power conversion techniques has a different input current waveform, it is expected that each also has a different input current spectrum. For example, the PWM converters have a mostly square-wave input current waveform, while the resonant converters have a more sinusoidal input current waveform. In the frequency domain, the spectrum of the square-wave current shape would be expected to have a higher number of significant harmonics than the spectrum of the sinusoidal-type waveforms. This relationship between the shape of the input current waveform with its spectrum will also be discussed.

The derived analytical expressions will be shown to be very accurate as long as the effects of any circuit parasitics are neglected; however, also in this work, is a study of typical parasitic effects on the input current spectrum. For this study of experimental results, four converters will be studied- each from a different power conversion technique. The experimental circuits tested include the three previously considered, and also the flyback Zero-Voltage-Switched Multi-Resonant-Converter (ZVS-MRC). All experimental results will be shown for the same operating condition so that comparisons among the conversion techniques can be made.

In Chapter 2, a complete analytical description of the input current spectrum of the flyback PWM converter will be derived. The equations will be tested against results obtained from an experimental circuit. Also, a theoretical example will be presented, and spectral plots for different line/load conditions will be shown.

Chapter 3 contains an analytical derivation of the flyback ZCS-QRC. The derived equations will be tested experimentally. A simplification in the description of the input current waveform will be made, and the results will be used in other equations. The same theoretical example as in Chapter 2 will be used to compute the spectrum for the ZCS-QRC case. The results will be compared to the PWM case. Also, an analytical comparison of the normalized spectrum of the ZCS-QRC and the PWM converter will be presented.

Chapter 4 continues with the analytical derivation of the flyback ZVS-QRC. As before, the analytical results will be tested experimentally. Again, the same theoretical example will be used to compute the spectrum of the flyback ZVS-QRC so that it can be compared to both the PWM and ZCS cases.

Chapter 5 is devoted to experimental results. In this chapter, experimental circuits for the flyback PWM, the flyback ZCS-QRC, the flyback ZVS-QRC, and the flyback ZVS-MRC will be built and their respective input current spectral plots shown. Differences between the experimental results ant the projected results are explained in terms of parasitics in the circuits.

Chapter 2

Pulse-Width-Modulated (PWM) Converter

2.1   Introduction

In this chapter, the input current spectrum for the flyback family of PWM converters will be derived. The expression for the spectrum will be a function of only external parameters (such as conversion ratio) and a design parameter of the input current ripple, ξ [2]. The result will be a function expressed in the following form: $f = f(M, \xi, m)$, where m is the Fourier variable.

An experimental test circuit of the flyback PWM converter will be presented. The converter will be run under certain operating conditions and the input current spectrum will be recorded using a spectrum analyzer. The recorded values will be compared against values obtained from the derived equations.

Also, to show the effect of line/load changes on the input current spectrum, a numerical example will be presented. For this example, specifications will be given, and the spectrum for several conditions will be calculated.

2.2 Flyback PWM

Figure 2.1 shows a flyback PWM converter. The converter can be divided into the input and the output. The input section consists of the voltage source, V_g, and the switch, S_1, while the output section consists of diode, D_0, capacitor, C_f, and the load, R_L.

Figure 2.2 shows an equivalent circuit of the flyback PWM converter. This circuit was constructed by reflecting the input (primary) side elements to the secondary side. Notice that L_f is the equivalent magnetizing inductance of the transformer of Fig. 2.1. This inductance, along with the capacitor C_f, create the output filter.

V_i and I_{in} of Fig. 2.2 can be written in terms of the converter of Fig. 2.1. The basic transformations are:

$$V_i = \frac{V_g}{n} \quad , \tag{2.1}$$

$$I_{in} = nI'_{in} \quad , \tag{2.2}$$

where n is defined as the turns ratio.
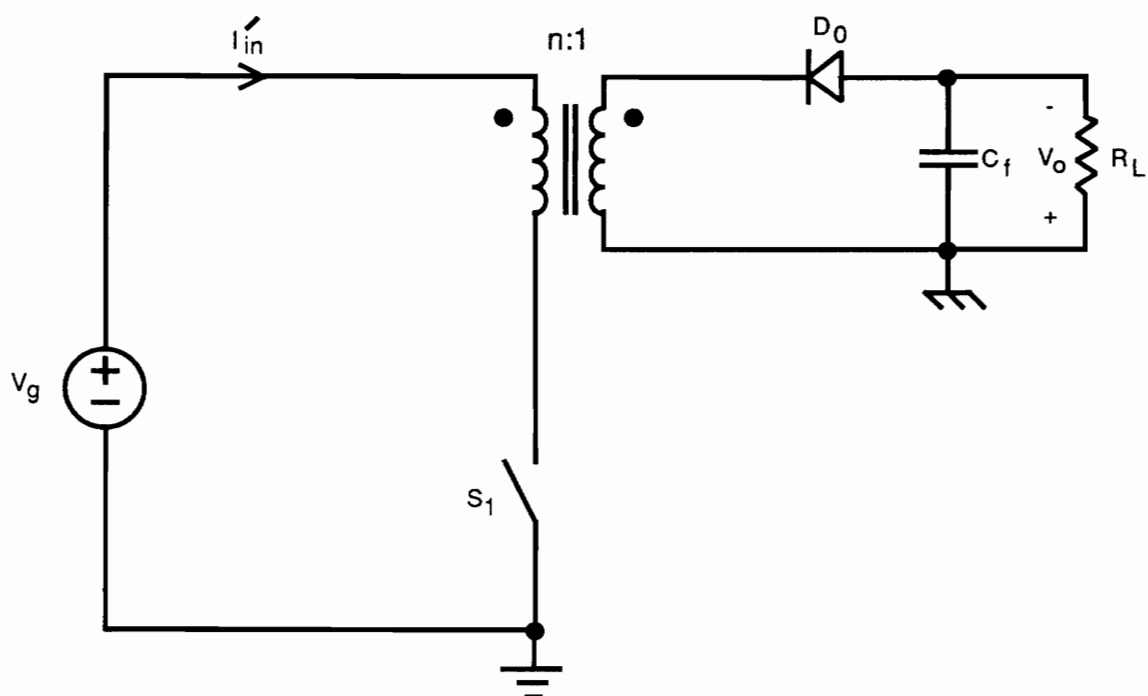
Figure 2.1. Simplified flyback PWM converter
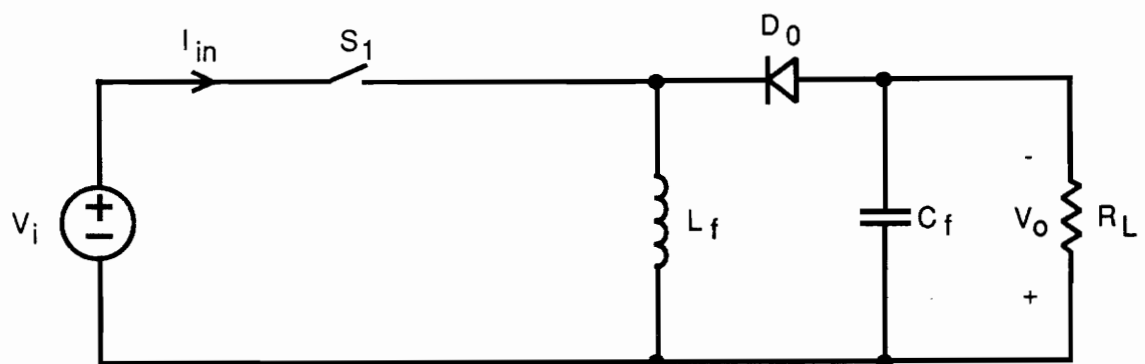
Figure 2.2.   Simplified buck/boost PWM converter

2.3 Input Current Equations

The flyback circuit of Fig.2.2 has only two stages during normal operation: (1) when switch S_1 is on, and (2) when switch S_1 is off. During the interval when the switch is on ($t_{on} = DT_s$), the input current can be written as:

$$I_{in}(t) = I_1 + \frac{\Delta I_{L_f}}{t_{on}} t \qquad 0 < t < T_1 \quad , \tag{2.3}$$

where

$$I_1 = I_x - \frac{\Delta I_{L_f}}{2} \quad , \tag{2.4}$$

and for the flyback converter, the inductor current is known to be:

$$I_x = \frac{I_o}{D'} \quad , \tag{2.5}$$

where ΔI_{L_f} is the ripple current associated with the inductor L_f. During the other interval, when the switch is off, the input current is zero.

Since the inductor current should be represented in terms of a dimensionless percent ripple, ξ, rather than a dimensioned current term [2,4,7], the input current can be written as:

$$I_{in}(t) = \begin{cases} I_x - I_x\xi + 2I_x\xi \dfrac{t}{t_{on}} & 0 < t < t_{on} \\ 0 & t_{on} < t < T_s \end{cases} \quad , \tag{2.6}$$

where ξ can be defined as [2]:

$$\xi = \frac{\Delta I_{L_f}/2}{I_x} \tag{2.7}$$

Incorporating the turns ratio of the transformer shown in Fig. 2.1-- *i.e.*, using (2.1) and (2.2), (2.6) can be used to write the input current equation for the flyback PWM converter as:

$$I'_{in}(t) = \frac{1}{n} \cdot \begin{cases} I_x - I_x\xi + 2I_x\xi \frac{t}{t_{on}} & 0 < t < t_{on} \\ 0 & t_{on} < t < T_s \end{cases} \quad , \quad (2.8)$$

where the following definitions still apply:

$$I_x = \frac{I_o}{D'} \quad , \quad (2.9)$$

$$\xi = \frac{\Delta I_L/2}{I_x} \quad , \quad (2.10)$$

$$t_{on} = DT_s \quad , \quad (2.11)$$

The only variable to be scaled by the turns ratio n is I_x (represented by the $1/n$ term). Notice that reflecting the current to the primary side has no effect on ξ. Theoretical waveforms of the flyback PWM converter are shown in Fig. 2.3.
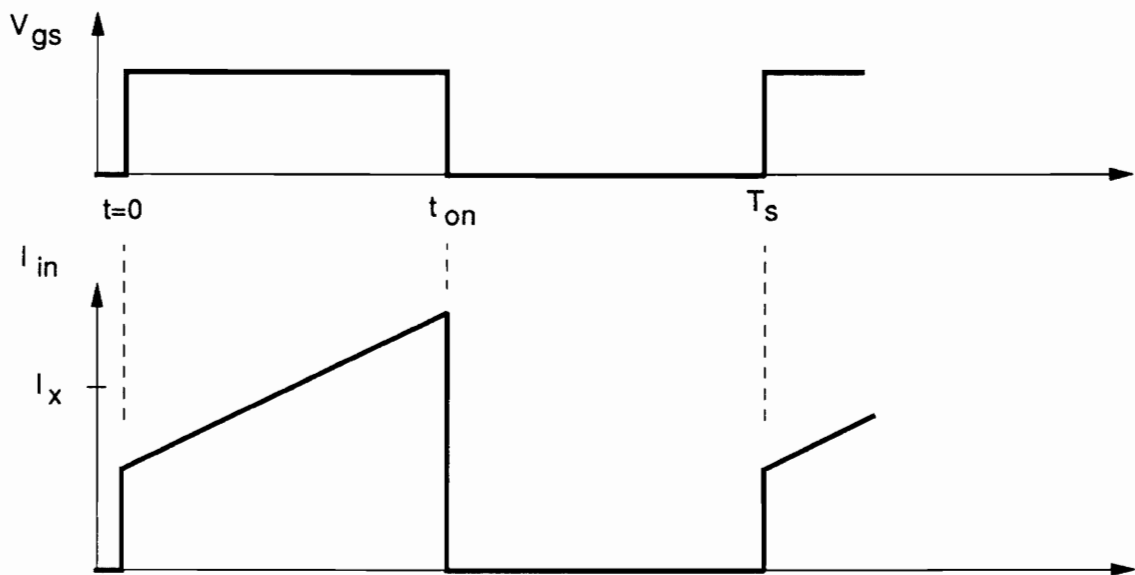
Figure 2.3. Theoretical waveforms of the flyback PWM converter

2.4   General Solution of the Fourier Coefficients

To find the Fourier coefficients of a function $f(t)$, the following equations must be solved [9]:

$$a_m = \frac{2}{T_s} \int_0^{T_s} f(t) \cos x_m t \; dt \qquad m = 0,1,2,... \tag{2.12}$$

$$b_m = \frac{2}{T_s} \int_0^{T_s} f(t) \sin x_m t \; dt \qquad m = 0,1,2,... \tag{2.13}$$

This allows the function $f(t)$ to be rewritten as a collection of sine and cosine terms:

$$f(t) = \sum_{m=0}^{\infty} a_m \cos x_m t + b_m \sin x_m t \; , \tag{2.14}$$

where

$$x_m = 2m\pi f_s \; . \tag{2.15}$$

The magnitude of the mth Fourier coefficient can be written as:

$$c_m = \sqrt{a_m^2 + b_m^2} \qquad m = 0,1,2,... \tag{2.16}$$

To find the input current spectrum, Eq. (2.12) through (2.16) need to be solved with $f(t) = I'_{in}(t)$. Although this will yield correct expressions, it is not the easiest way to solve the equations.

A better representation of $f(t)$ can be found by shifting the time axis to the right until time $t = 0$ corresponds to the time when $I_{in}(t) = I_x$. This shift is shown in Fig. 2.4. Since I_x is the

exact middle of the ramp current, the switch is on for a duration of $t_{on}/2$ on either side of the new $t = 0$ point. Recall that when computing a Fourier series, a time shift is legal as long as the integration still encompasses one period.

Using this shift allows some terms in the integration to be solved with the help of symmetry properties of odd functions. Equation (2.8) can be rewritten as:

$$I'_{in}(t) = \frac{1}{n} \cdot \begin{cases} I_x + pt & -\frac{t_{on}}{2} < t < \frac{t_{on}}{2} \\ 0 & \frac{t_{on}}{2} < t < T_s - \frac{t_{on}}{2} \end{cases} , \qquad (2.17)$$

where

$$p = \frac{2I_x \xi}{t_{on}} . \qquad (2.18)$$

Now, using (2.17) as $f(t)$, (2.12) and (2.13) can now be written as:

$$a_m = \frac{2}{T_s} \frac{1}{n} \int_{-\frac{t_{on}}{2}}^{\frac{t_{on}}{2}} (I_x + pt) \cos x_m t \; dt , \qquad (2.19)$$

$$b_m = \frac{2}{T_s} \frac{1}{n} \int_{-\frac{t_{on}}{2}}^{\frac{t_{on}}{2}} (I_x + pt) \sin x_m t \; dt . \qquad (2.20)$$

Integrating and simplifying:

$$a_m = \frac{2}{m\pi} \frac{I_x}{n} \sin \theta_m , \qquad (2.21)$$

$$b_m = \frac{2}{m\pi} \frac{p}{n} \left[\frac{1}{x_m} \sin \theta_m - \frac{t_{on}}{2} \cos \theta_m \right] , \qquad (2.22)$$

where

$$\theta_m = x_m \frac{t_{on}}{2} = m\pi D = m\pi \frac{M}{M+1} \quad .$$

(2.23)

Equation (2.16) then becomes:

$$c_m = \frac{I_x}{n} c'_m \quad ,$$

(2.24)

where

$$c'_m{}^2 = \frac{4}{m^2\pi^2}\left[\left(1 + \frac{\xi^2}{\theta_m^2}\right)\sin^2\theta_m + \xi^2\cos^2\theta_m - \frac{\xi^2}{\theta_m}\sin 2\theta_m\right] \quad .$$

(2.25)

Equation (2.25) is completely a function of only three parameters: $c'_m = f(M, \xi, m)$, and since it is independent of inductor current, it can be considered to be a normalized representation. The worst-case spectrum for the flyback PWM converter can be found using (2.24) with $M = M_{max}$, $I_o = I_{o,max}$ and $\xi = \xi_c$.
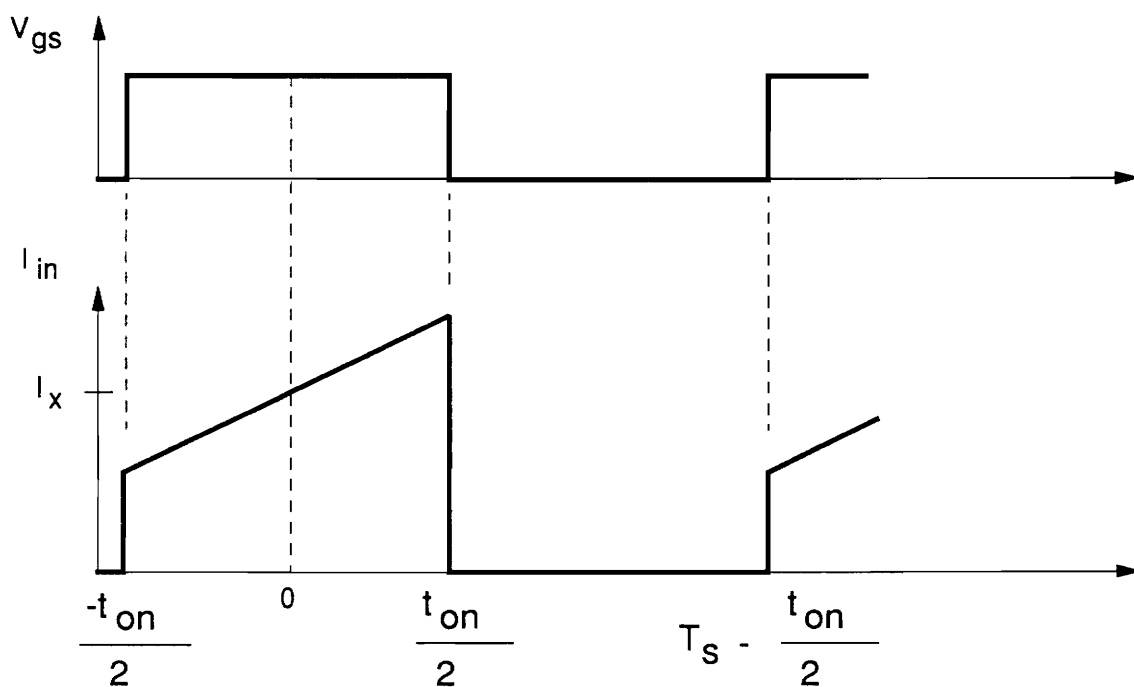
Figure 2.4. Time shifted theoretical waveforms used in the calculation of the Fourier series

2.5 *Experimental Results*

The purpose of this section is to test the analytical results of the previous sections against experimental results. In the previous sections, a complete analytical expression for the input current spectrum of the PWM flyback converter was developed.

The PWM flyback converter of Fig. 2.5 was constructed and tested. The experimental circuit waveforms are shown in Fig. 2.6. The current waveform was fed into the HP8568B spectrum analyzer, and the peak levels of the first twenty harmonics were recorded. The experimental data for the first twenty harmonics obtained from the spectrum analyzer are shown in Table 2.1.

For the analytical results, (2.24) to (2.25) were used with numbers obtained from the actual experimental waveforms of Fig. 2.6. The analytic computations were performed to yield the first twenty harmonics. The theoretical results are also shown in Table 2.1.

An overplot of the experimental data with the theoretical data is shown in Fig. 2.7. The two sets of data correspond well throughout the entire spectrum shown; therefore, the equations presented in the previous sections do provide an accurate description of the input current spectrum for the PWM flyback converter.

Table 2.1. Experimental and theoretical PWM spectral data

m	Theoretical (dB)	Experimental (dB)
1	6.6	6.7
2	-9.1	-9.0
3	-3.1	-3.1
4	-14.6	-15.2
5	-7.7	-7.6
6	-17.4	-18.3
7	-10.7	-10.6
8	-19.1	-20.7
9	-13.1	-12.8
10	-20.1	-20.8
11	-15.0	-14.7
12	-20.9	-21.0
13	-16.7	-16.5
14	-21.5	-21.3
15	-18.3	-18.2
16	-21.9	-21.3
17	-19.7	-20.0
18	-22.3	-21.3
19	-21.1	-21.8
20	-22.6	-21.4
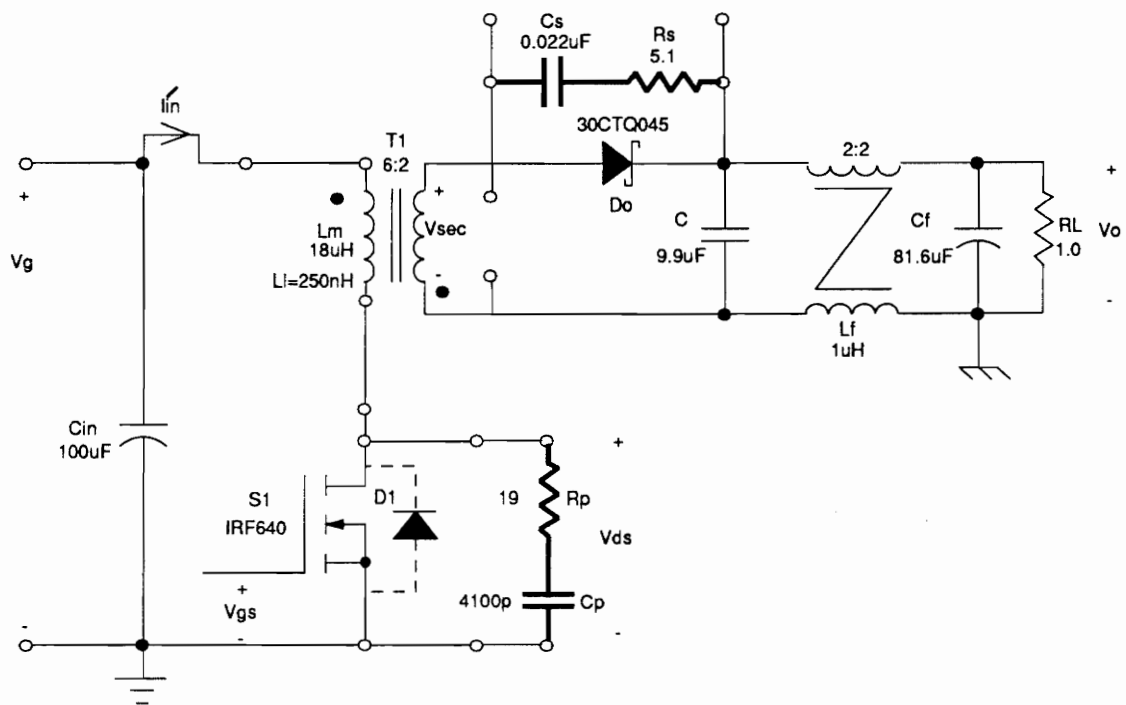
Figure 2.5. Experimental PWM circuit

Tek

Top trace: V_{GS}
Middle trace: I'_{in}
Bottom trace: V_{DS}
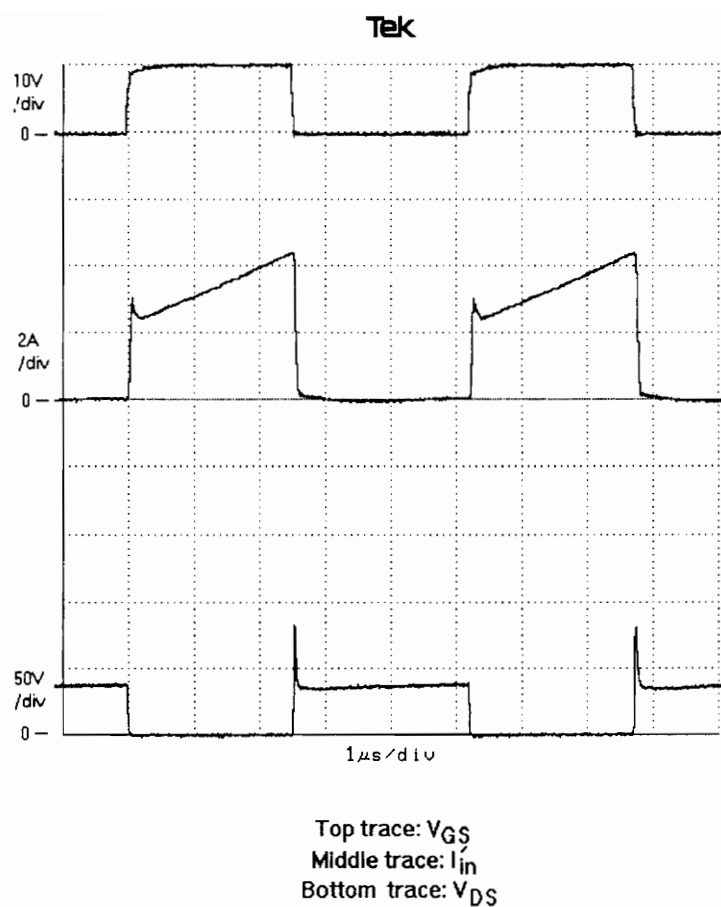
Figure 2.6.   Experimental PWM waveforms
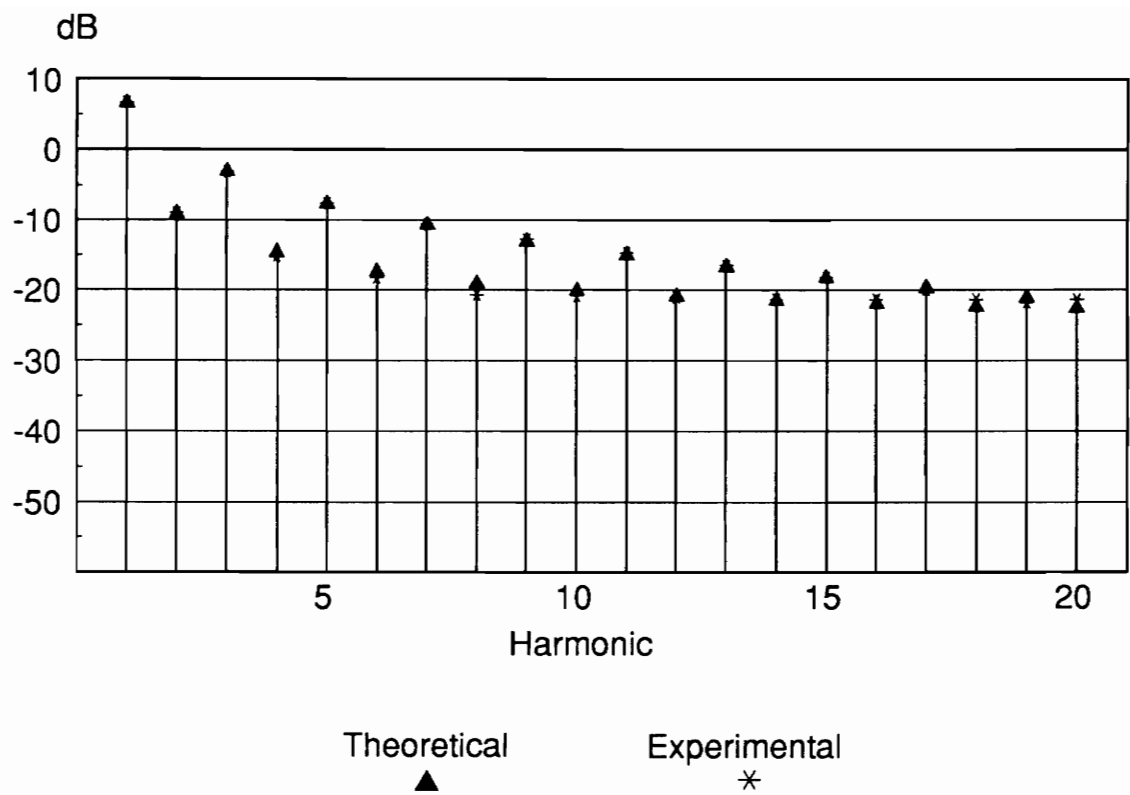
Figure 2.7. Overplot of experimental and theoretical spectrums

2.6 A Theoretical Example

To examine the changes in the spectrum as a function of line and load conditions, a numerical example will be presented. For this example, assume the following operating conditions:

- $V_g = 21\,V$ to $32\,V$

- $V_{g,nominal} = 24\,V$

- $V_o = 5\,V$

- $I_o = 1\,A$ to $5\,A$

- $f_s = 200\,kHz$

- $n = 3\,turns$

- $\xi_c = 0.1$

Also, assume that the converter is operating in the continuous conduction mode at all times.

Six specific cases are of interest: low-line, light-load; low-line, full-load; nominal-line, light-load; nominal-line, full-load; high-line, light-load; high-line, full-load. The spectral data of these six cases were computed and graphed in Figs. 2.8 (a-f), respectively.

According to [2], for PWM converters, a value of 0.1 to 0.2 should be assigned to ξ_c when designing for the worst-case. Therefore, when designing PWM converters to meet given specifications, ξ_c should be used for the case of maximum inductor current, i.e., full-load. The spectrum for the low-line, full-load case was computed for $\xi = \xi_c = 0.1$. As the line/load

conditions change, so must the value of ξ. To account numerically for this change in ξ, ξ_c must be scaled by the new line/load conditions of duty cycle (actually M) and output current (I_o) of each case. Doing this, the input current spectrum for the remaining cases can be calculated.

Examining Figs. 2.8 (a-f), patterns in the envelope of the spectrum can be seen. Peaks and valleys in the spectrum seem to move with a change in line/load conditions. In fact, examining the figures closely reveals that the dependence is mostly on line conditions (M and D) and is independent of load conditions (I_o). This corresponds to the derived equations which, although a function of the load current, are more a function of the conversion ratio.
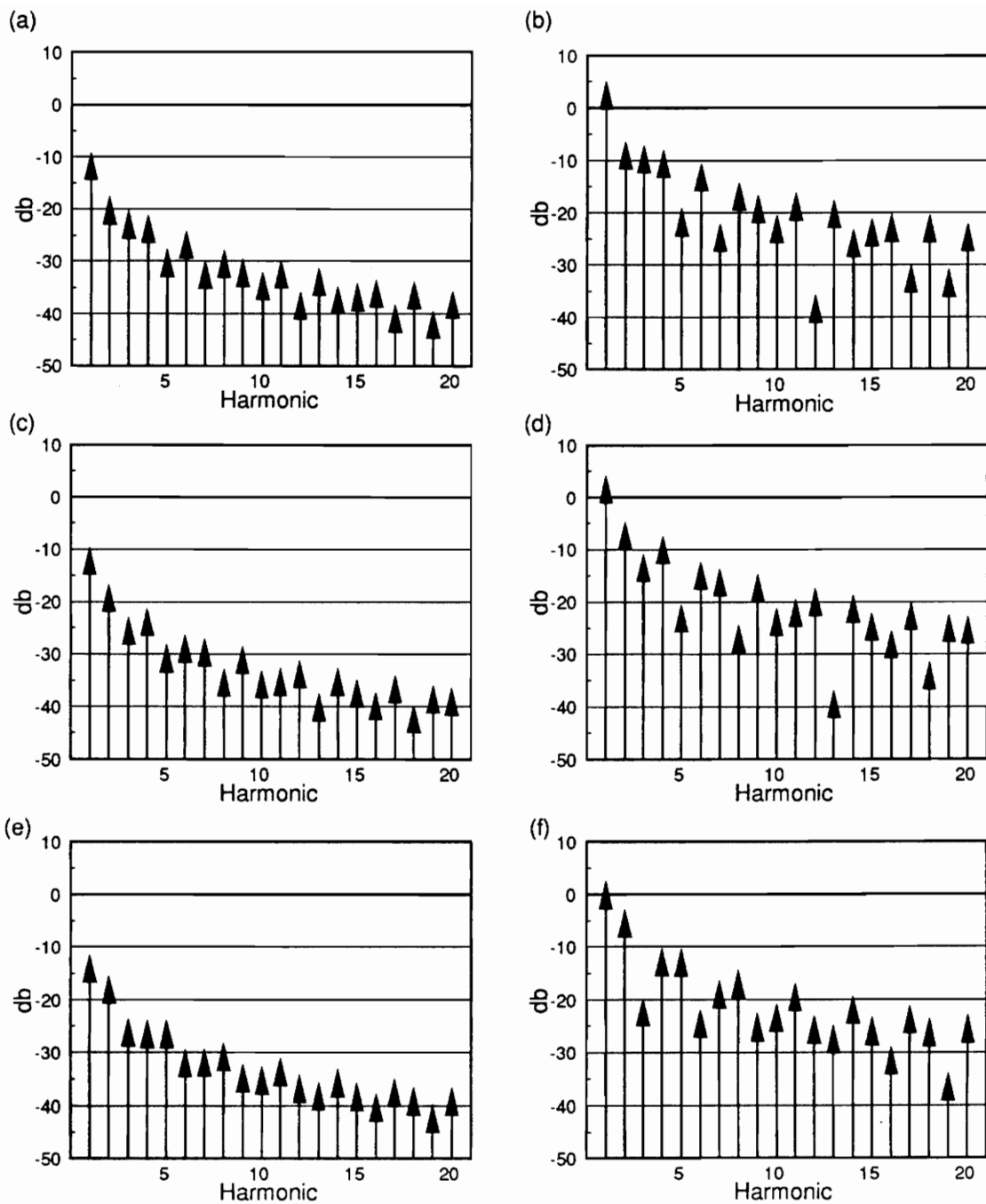
Figure 2.8. Spectrum for different cases of the flyback PWM converter: (a) low-line and light-load, (b) low-line and full-load, (c) nominal-line and light-load, (d) nominal-line and full-load, (e) high-line and light-load, and (f) high-line and full-load

2.7 Extensions to Other Converters

Equations (2.24) and (2.25) were derived to express the input current spectrum for flyback converters in terms of external parameters and a design constraint, ξ. The generality of these equations is worth discussion.

The input current waveform of flyback PWM converters consists of a pulsed current, and the equations derived were for this pulsed current. A pulsed input current, however, is not unique to flyback converters. The buck type converters also have a pulsed input current. This would allow (2.24) and (2.25) to be used to describe the input current of buck converters as long as the equations for the duty cycle D, the conversion ratio M, and the average inductor current I_x are all changed accordingly.

2.8 Summary

In this chapter, the complete analytical expressions of the input current spectrum for flyback PWM converters were derived. These equations were presented with the inductor current term factored out. By doing this, the effect of other parameter changes (as for M and ξ_c) can be seen more clearly. Also, this normalized format will allow a comparison of the PWM converters to resonant converters.

The analytical results were also tested against experimental results. A flyback PWM converter was built, and the input current spectrum was recorded from a spectrum analyzer. The experimental results were then compared to results obtained by using the derived expressions for the input current spectrum. Since these two sets of results corresponded well, the derived expressions can be used to predict the input current spectrum of the flyback PWM converter.

Also, an example was presented in which specifications for a converter were given. These specifications were used to compute the spectrum at various line/load conditions. For that example, it was evident that the spectrum was mostly dependent on load conditions and was almost independent of line conditions.

Chapter 3

Zero-Current-Switched Quasi-Resonant Converter

(ZCS-QRC)

3.1 Introduction to ZCS-QRC

By employing an LC resonant tank in the circuit, the main switch current can be shaped so that during the on-time of the switch, the current has a quasi-sinusoidal form. This action forces the current to be zero at turn-off. Because of this shape, for the same average current the peak current will be higher in ZCS-QRC than for the PWM converter. Relating this to the spectrum, it would be expected that the magnitudes of the lower harmonics are higher for ZCS than for PWM; also, because of the quasi-sinusoidal shape of the waveform, the magnitudes of the higher harmonics should fall off faster for ZCS than for PWM.

The ZCS technique is valid for all of the basic converters; however, only the flyback converter will be studied. All the equations will be derived for an equivalent circuit converter and di-

rectly applied to the isolated flyback converter by using simple transformations that arise from reflecting the primary side elements of the flyback converter to the secondary side.

3.2 Flyback ZCS-QRC

Figure 3.1 shows a schematic of a flyback ZCS-QRC. The resonant elements L_o and C_o shape the switch current waveform during the on-time to ensure turn-off at zero current.

Diode D_2 needs to be included for half-wave mode operation. As the current through the switch begins to resonate, D_2 is forward biased. When the current reaches zero, the switch is opened. Without diode D_2, the current could still flow in the opposite direction by way of the inherent body diode (D_1) of the switch. Diode D_2 stops this reverse flow of the resonant current and clamps the input current at zero when switch S_1 is off.

The output stage, D_0, C_f, R_L, is also shown in Fig. 3.1.

To find an equivalent circuit for Fig. 3.1, simply reflect the primary side elements to the secondary side. The resonant inductor (L_o) is scaled down by the square of the turns ratio, n. Also, the input voltage (V_g) and the input current (I'_{in}) are scaled down and up, respectively, by n.

The ideal switch and diodes transfer to the secondary without any change. So far all of the components have been defined for use in the secondary side. The flyback converter has now been reduced to the equivalent circuit shown in Fig. 3.2.

The converter of Fig. 3.2 is a direct result of Fig. 3.1 as explained above. L_r and C_r represent the resonant elements that shape the switch current waveform. All of the diodes (D_0, D_1, D_2), the output capacitor (C_f), the output resistance (R_L), and the switch (S_1) function in the same way as they did for the circuit of Fig. 3.1.

The output filter inductance, L_f, is the only element that was not described above. In the flyback converter of Fig. 3.1, when the switch is off, the energy stored in the transformer is delivered to the output. This current circulates through the secondary side inductance of the transformer. This inductance, along with the output capacitance, combine to create an output filter. The value of this secondary side inductance is usually large enough so that it can be correctly modeled as a constant current source during normal operation.

The following basic transformations are made so that elements of Fig. 3.2 can be written in terms of elements of the converter in Fig. 3.1:

$$L_r = \frac{L_o}{n^2} \quad , \tag{3.1}$$

$$C_r = C_o \quad , \tag{3.2}$$

$$V_i = \frac{V_g}{n} \quad , \tag{3.3}$$

$$I_{in} = n I'_{in} \quad . \tag{3.4}$$

Since the resonant capacitor C_o of the flyback converter was originally placed on the secondary side, no scaling is needed to transform this element to its equivalent value. The other elements, however, need to be scaled accordingly.

For the converter of Fig. 3.2, the key circuit parameters, namely, characteristic impedance, resonant angular frequency, and conversion ratio are defined as:

$$Z_o = \sqrt{\frac{L_r}{C_r}} \quad , \tag{3.5}$$

$$\omega_o = \frac{1}{\sqrt{L_r C_r}} \quad , \tag{3.6}$$

and

$$M = \frac{V_o}{V_i} \quad , \tag{3.7}$$

respectively.

Also, the normalized output impedance Q is defined as the ratio of the output impedance to the characteristic impedance:

$$Q = \frac{R_L}{Z_o} \quad . \tag{3.8}$$

Now that the relations between the Figs. 3.1 and 3.2 have been established mathematically, the general description of the operation can be discussed.
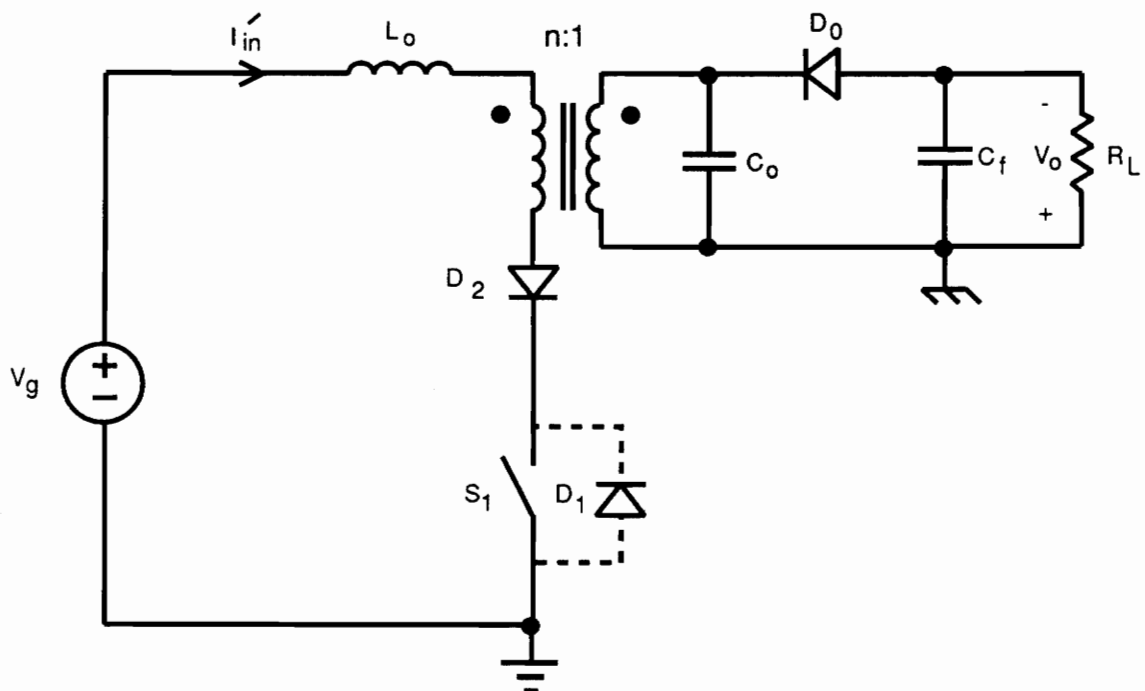
Figure 3.1. Circuit diagram of a flyback ZCS-QRC
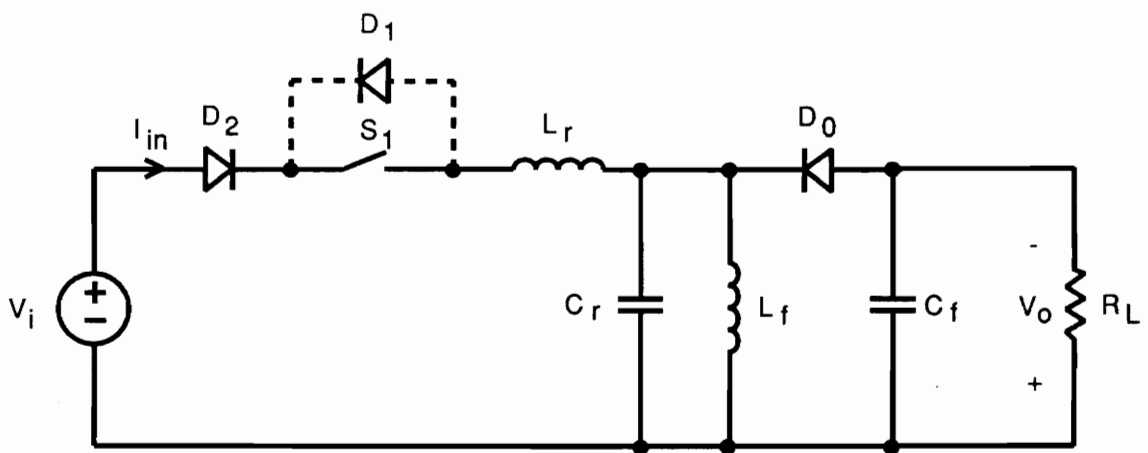
Figure 3.2.   Circuit diagram of an equivalent flyback ZCS-QRC

3.3 Stages of Operation

To describe the operation of the ZCS-QRC of Fig 3.2, one switching cycle can be divided into four stages. As for the buck converter presented in [1], the state equation(s) of each stage can be found and solved.

The output inductor L_f in Fig. 3.2 can be modeled as a current source. From [1], the magnitude of this current source is found to be:

$$I_x = \frac{M}{Q} \frac{V_i + V_o}{Z_o} \quad , \tag{3.9}$$

where M, Q, and Z_o are defined as in the previous section.

Initially, assume that the current I_x is being delivered to the load and that switch S_1 is open. Now the four stages of operation can be described.

- STAGE 1. Inductor-Charging Stage $[T_0, T_1]$

  At time T_0, switch S_1 closes, and the current through L_r; I_{L_r}, rises linearly until time T_1 when all of I_x is through the inductor. The voltage drop across the resonant inductor is constant at $V_i + V_o$ during this stage.

  The initial condition and the governing state equation for this stage are:

$$I_{L_r}(0) = 0 \quad , \tag{3.10}$$

$$L_r \frac{dI_{L_r}}{dt} = V_i + V_o \quad . \tag{3.11}$$

At time T_1, all of the current is depleted from the load so that diode D_0 is off. The duration of this stage is found to be:

$$T_{01} = L_r \frac{I_x}{V_i + V_o} \quad . \tag{3.12}$$

The equivalent circuit of the the inductor-charging stage is shown in Fig. 3.3(a).

- STAGE 2. Resonant Stage $[T_1, T_2]$

At time T_1, when diode D_0 turns off, the reactive elements L_r and C_r begin to resonate. This resonate action causes I_{in} to be sinusoidal during this interval. For half-wave mode operation, the switch is opened when current first reaches zero, at time T_2

The initial conditions and state equations for this stage are:

$$I_{L_r}(0) = I_x \quad , \tag{3.13}$$

$$V_{C_r}(0) = -V_o \quad , \tag{3.14}$$

and

$$L_r \frac{dI_{L_r}}{dt} = V_i - V_{C_r} \quad , \tag{3.15}$$

$$C_r \frac{dV_{C_r}}{dt} = I_{L_r} - I_x \quad , \tag{3.16}$$

respectively. Using the initial conditions, the solutions to (3.15) and (3.16) can be found to be:

$$I_{L_r}(t) = I_x + \frac{V_i + V_o}{Z_o} \sin \omega_o t \quad , \tag{3.17}$$

$$V_{C_r}(t) = V_i - (V_i + V_o) \cos \omega_o t \quad . \tag{3.18}$$

The time it takes from the the beginning of this stage until $I_{in} = 0$ can be found to be:

$$T_{12} = \frac{\alpha}{\omega_o} \quad , \tag{3.19}$$

where

$$\alpha = \sin^{-1}\left(\frac{-Z_o I_x}{V_i + V_o} \right) \quad . \tag{3.20}$$

Since half-wave mode operation is assumed, the following constraint is imposed on α:

$$\pi < \alpha < \frac{3}{2}\pi \quad . \tag{3.21}$$

An equivalent circuit of the resonant stage is shown in Fig 3.3(b).

- STAGE 3. Capacitor-Discharging Stage [T_2, T_3]

At time T_2, when there is no current through switch S_1, it is opened. Since diode D_0 is still reverse biased, capacitor C_r will discharge through the current source I_x until the voltage on the capacitor has decreased enough to let diode D_0 become forward biased, at time T_3. The resonant capacitor has an initial condition of:

$$V_{C_r}(0) = V_i - (V_i + V_o) \cos \alpha \quad , \tag{3.22}$$

The following state equation describes the capacitor discharge through the constant current source I_x:

$$C_r \frac{dV_{C_r}}{dt} = -I_x \quad . \tag{3.23}$$

The capacitor-discharging stage has a duration of T_{23}, which is found to be:

$$T_{23} = \frac{1}{\omega_o} \frac{V_i + V_o}{Z_o I_x} (1 - \cos \alpha) \quad .$$ (3.24)

An equivalent circuit of the capacitor-discharging stage is shown in Fig. 3.3(c).

- STAGE 4. Passive Stage $[T_3, T_4]$.

At time T_3, the voltage across C_r is low enough to forward bias diode D_0. Since the voltage across V_{C_r} is now clamped at a constant of $-V_o$, no current is being delivered to the capacitor. Thus,

$$C_r \frac{dV_{C_r}}{dt} = 0 \quad .$$ (3.25)

Therefore, all of the current is now being delivered to the output. This current will continue to freewheel through the output until switch S_1 is turned on again, starting a new switching cycle. The duration of the passive stage can be described as:

$$T_{34} = T_s - T_{01} - T_{12} - T_{23} \quad ,$$ (3.26)

where T_s is the period of the switching cycle.

An equivalent circuit of the passive stage is shown in Fig. 3.3(d).
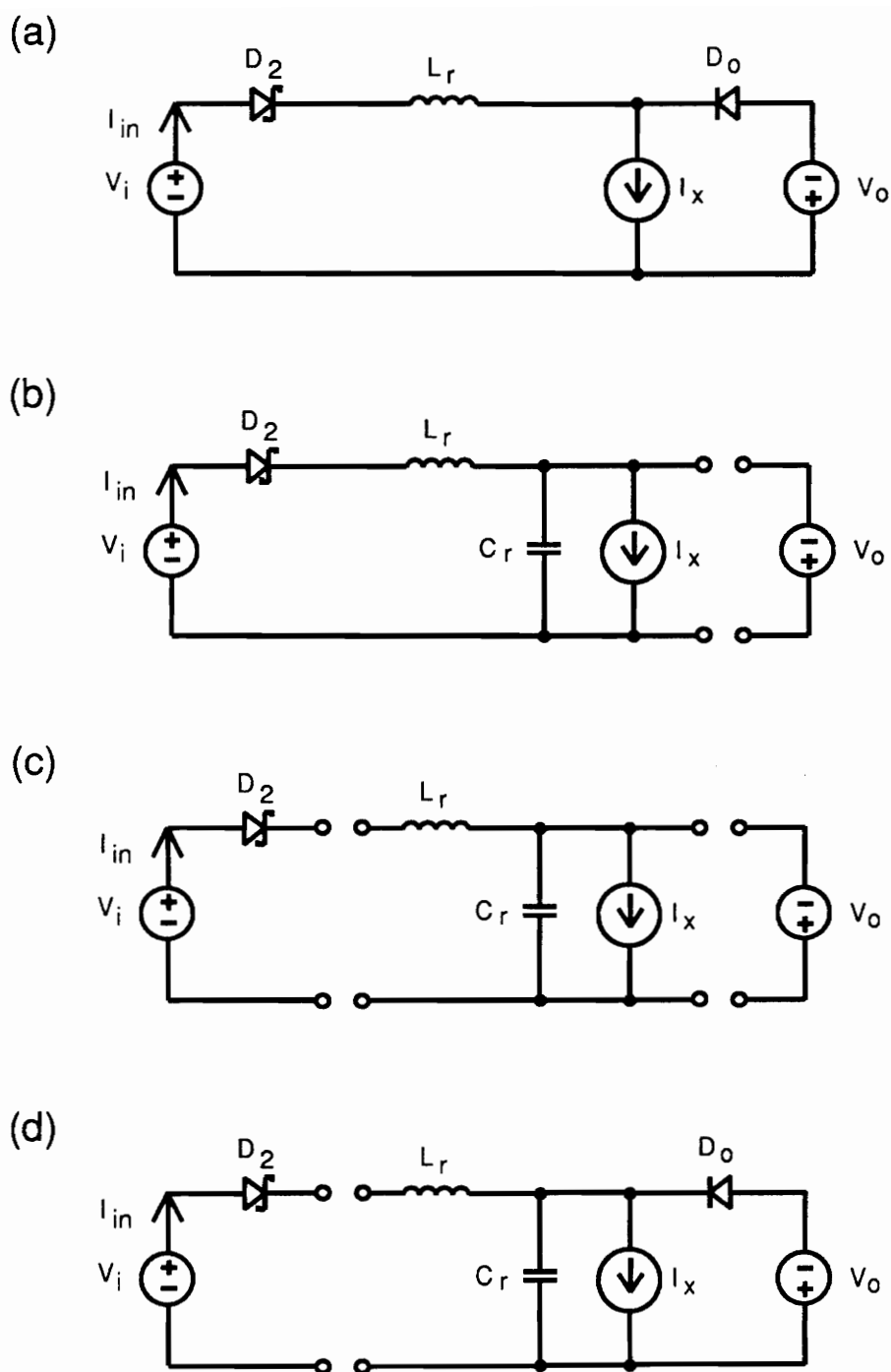
Figure 3.3. Stages of equivalent flyback ZCS-QRC circuit: (a) inductor-charging stage, (b) resonant stage, (c) capacitor-discharging stage, and (d) passive stage

Zero-Current-Switched Quasi-Resonant Converter (ZCS-QRC) 37

3.4 Input Current Equations

Section 3.3 described the four stages of operation associated with zero-current-switching. As was mentioned above, descriptions of the operation of Fig. 3.2 can be extended to the flyback ZCS-QRC of Fig. 3.1. Also included in the descriptions in the previous sections were the equations of the resonant inductor current, I_{L_r}, of each stage. Notice that for the converter of Fig. 3.2, the following relation exists:

$$I_{in}(t) = I_{L_r}(t) \ . \tag{3.27}$$

Now, the pieces of the input current can be assembled into one function.

During $[T_0, T_1]$, the resonant inductor was found to be charging linearly. Given (3.11), the input current can represented by:

$$I_{in}(t) = yt \quad T_0 < t < T_1 \ , \tag{3.28}$$

where y is the constant slope of the current during this interval.

$$y = \frac{V_i + V_o}{L_r} \ . \tag{3.29}$$

The input current during the resonant stage $[T_1, T_2]$ was found to have the form of (3.17); however, for the initial condition of $I_{in}(t) = I_x$ to be met, (3.17) needs to be rewritten as:

$$I_{in}(t) = I_x + u \sin \omega_o(t - T_{01}) \quad T_1 < t < T_2 \ , \tag{3.30}$$

where u is defined as:

$$u = \frac{V_i + V_o}{Z_o} \quad .$$

<div align="right">(3.31)</div>

For the remaining two stages of the switching cycle, the switch is open, and diode D_2 is blocking any reverse current:

$$I_{in}(t) = 0 \quad T_2 < t < T_3$$

<div align="right">(3.32)</div>

$$I_{in}(t) = 0 \quad T_3 < t < T_4$$

<div align="right">(3.33)</div>

The total continuous representation of the input current for the ZCS-QRC circuit of Fig. 3.2 can be written as:

$$I_{in}(t) = \begin{cases} yt & T_0 < t < T_1 \\ I_x + u \sin \omega_o(t - T_{01}) & T_1 < t < T_2 \\ 0 & T_2 < t < T_4 \end{cases}$$

<div align="right">(3.34)</div>

Theoretical waveforms representing these equations are shown in Fig. 3.4.

In order to find the expression of the input current of the flyback ZCS-QRC of Fig. 3.1, (3.34) needs to rewritten in terms of its converter components (L_o, C_o, V_g). To do this, the simple transformations found in Section 3.2 (rewritten here as (3.35)-(3.37)) need to be used:

$$L_r = \frac{L_o}{n^2} \quad ,$$

<div align="right">(3.35)</div>

$$C_r = C_o \quad ,$$

<div align="right">(3.36)</div>

$$V_i = \frac{V_g}{n} \quad .$$

<div align="right">(3.37)</div>

Notice that these transformations should first be used in the expressions that describe the key circuit parameters, namely, the characteristic impedance, the resonant angular frequency,

and the voltage conversion ratio. Using the above transformations, the key circuit parameters become:

$$Z_o = \frac{1}{n} \sqrt{\frac{L_o}{C_o}} \quad , \tag{3.38}$$

$$\omega_o = \frac{n}{\sqrt{L_o C_o}} \quad , \tag{3.39}$$

and

$$M = n \frac{V_o}{V_g} \quad , \tag{3.40}$$

respectively.

Although (3.34) is the correct *form* of the input current equation of the flyback converter, the values of the variables change with the transformation. Also, note that the magnitude of the input current of the flyback converter is scaled down by n, as shown in (3.4). Therefore, the complete expression of the input current of the flyback ZCS-QRC of Fig. 3.1 is:

$$I'_{in}(t) = \frac{1}{n} \cdot \begin{cases} yt & T_0 < t < T_1 \\ I_x + u \sin \omega_o(t - T_{01}) & T_1 < t < T_2 \\ 0 & T_2 < t < T_4 \end{cases} \quad , \tag{3.41}$$

where the following definitions now apply:

$$I_x = \frac{M}{Q} \frac{V_g}{n} \frac{(1 + M)}{Z_o} \quad , \tag{3.42}$$

$$y = \frac{V_g}{n} \frac{(1 + M)}{Z_o} \omega_o \quad , \tag{3.43}$$

$$u = \frac{V_g}{n} \frac{(1+M)}{Z_o} \quad , \tag{3.44}$$

$$T_{01} = \frac{1}{\omega_o} \frac{M}{Q} \quad , \tag{3.45}$$

$$T_{12} = \frac{\alpha}{\omega_o} \quad . \tag{3.46}$$

Notice that α can still be defined as:

$$\alpha = \sin^{-1}\left(-\frac{M}{Q}\right) \quad . \tag{3.47}$$

All of the equations in this section are used in order to describe the input current of the flyback ZCS-QRC in terms of its parameters: V_g, L_o, C_o, n.
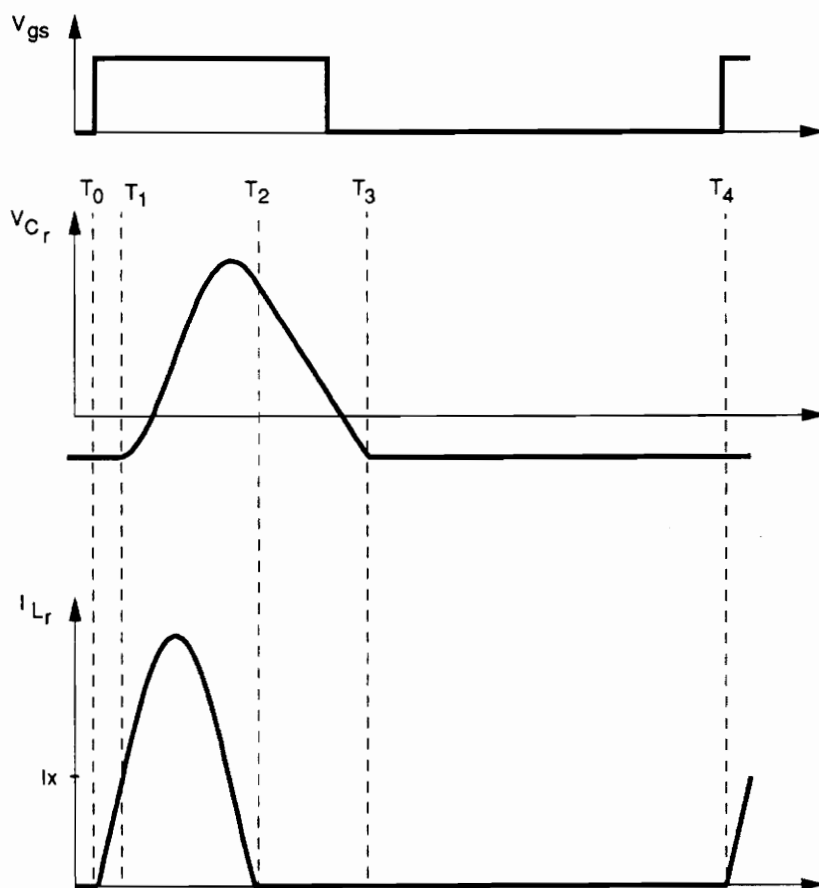
Figure 3.4. Theoretical waveforms of equivalent flyback ZCS-QRC

3.5   General Solution of the Fourier Coefficients

To find the Fourier coefficients of the input current, apply the following equations [10]:

$$a_m = \frac{2}{T_s} \int^{T_s} f(t) \cos x_m t \, dt \quad m = 0,1,2, \dots \tag{3.48}$$

$$b_m = \frac{2}{T_s} \int^{T_s} f(t) \sin x_m t \, dt \quad m = 0,1,2, \dots \tag{3.49}$$

This allows the function $f(t)$ to be rewritten as a collection of sine and cosine terms so that:

$$f(t) = \sum_{m=0}^{\infty} a_m \cos x_m t + b_m \sin x_m t \;, \tag{3.50}$$

where

$$x_m = 2m\pi f_s \;. \tag{3.51}$$

The magnitude of the mth Fourier coefficient is written as:

$$c_m = \sqrt{a_m{}^2 + b_m{}^2} \quad m = 0,1,2, \dots \tag{3.52}$$

Using $f(t) = I'_{in}(t)$ where $I'_{in}(t)$ is represented in (3.41) will yield the Fourier coefficients of the input current for the flyback ZCS-QRC.

The integration is performed in Appendix A. The final results of the integrations assign the following values to a_m and b_m:

$$a_m = \frac{I_x}{n} a'_m \;, \tag{3.53}$$

$$b_m = \frac{I_x}{n} b'_m \quad , \tag{3.54}$$

where

$$
\begin{aligned}
m\pi a'_m = \; & \frac{Q}{M} \left[\frac{\omega_o}{x_m} (\cos x_m T_{01} - 1) + \omega_o T_{01} \sin x_m T_{01} \right] \\
& + [\sin x_m T_A - \sin x_m T_{01}] \\
& - \frac{Q}{M} \frac{1}{d_m} \left\{ \frac{\omega_o}{x_m} [\cos x_m T_A \cos \omega_o T_{12} - \cos x_m T_{01}] \right. \\
& \qquad\qquad \left. + \sin x_m T_A \sin \omega_o T_{12} \right\}
\end{aligned}
\tag{3.55}
$$

and

$$
\begin{aligned}
m\pi b'_m = \; & \frac{Q}{M} \left[\frac{\omega_o}{x_m} \sin x_m T_{01} - \omega_o T_{01} \cos x_m T_{01} \right] \\
& + (\cos x_m T_{01} - \cos x_m T_A) \\
& \frac{Q}{M} \frac{1}{d_m} \left\{ \frac{\omega_o}{x_m} [\sin x_m T_{01} - \sin x_m T_A \cos \omega_o T_{12}] \right. \\
& \qquad\qquad \left. + \cos x_m T_A \sin \omega_o T_{12} \right\}
\end{aligned}
\tag{3.56}
$$

Also note that the following definition was made in Appendix A:

$$d_m = \frac{\omega_o^2}{x_m^2} - 1 \quad . \tag{3.57}$$

Therefore, the magnitude of the Fourier coefficients is:

$$c_m = \frac{I_x}{n} c'_m \quad , \tag{3.58}$$

where

$$c'_m = \sqrt{(a'_m)^2 + (b'_m)^2} \quad . \tag{3.59}$$

These results represent the complete general form of the input current spectrum for the flyback ZCS-QRC of Fig. 3.1.

Equations (3.58-3.59) represents the normalized spectrum independent of inductor (load) current and can be used in an analytical comparison.

3.6 Experimental Results

The purpose of this section is to test the analytical results of the previous sections against experimental measurements. In the previous sections, a complete analytical expression for the input current spectrum of the flyback ZCS-QRC was developed.

The flyback ZCS-QRC converter shown in Fig. 3.5 was constructed and tested. The experimental waveforms are shown in Fig. 3.6. A current probe was placed so that the input current waveform could be recorded on the oscilloscope. The coaxial cable was then disconnected from the scope and placed on the signal input to the spectrum analyzer. The magnitudes of the input current spectrum were recorded from the spectrum analyzer and are shown in Table 3.1.

The parameters (f_o, f_s, T_{01}, etc.) used in the equations of the theoretical computations were determined from the experimental waveforms. Once these parameter values were determined, the magnitudes of the input current spectrum could be computed. Only the first twenty harmonics are shown in Table 3.1.

An overplot of the experimental data with the theoretical data is shown in Fig. 3.7. The two sets of data correspond well at the lower harmonics. It seems, however, that around harmonic 14, the two sets of data do not correspond to each other as well as they did for the lower harmonics.

Examining the oscillograms of Fig. 3.6 closely shows that the input current has a oscillation imposed on it during the off-time of the switch.

It is known [15] that an attenuated sine wave disturbance in the time domain enters the frequency domain as a bell-shaped function centered around the sine wave's frequency; therefore, it would be expected that the experimental data be higher (in db) than the theoretical data for the same harmonic number. Any discrepancy between the theoretical data and the experimental data should be at harmonic number:

$$\frac{f(\text{high frequency attenuated sine wave})}{f(\text{switching})} = \frac{9.5\text{MHz}}{680\text{kHz}} = 14 \quad . \tag{3.60}$$

Therefore, the significant difference between the experimental data and the theoretical data should be symmetrical around harmonic number fourteen.

Figure 3.8 shows a plot of the theoretical data subtracted from the experimental data. As expected, the difference between the two data sets is only significant symmetric to harmonic number 14.

Therefore, the analytical results achieved in Chapter 3 do represent an accurate description of the input current spectrum of the flyback ZCS-QRC.

Table 3.1. Experimental and theoretical ZCS-QRC spectral data

m	Theoretical (dB)	Experimental (dB)
1	8.2	8.4
2	6.8	7.0
3	4.3	4.8
4	0.4	1.1
5	-5.6	-4.7
6	-16.9	-17.0
7	-21.5	-16.8
8	-17.2	-13.6
9	-20.2	-16.0
10	-31.7	-25.1
11	-26.2	-25.4
12	-23.4	-17.7
13	-26.6	-17.5
14	-46.5	-24.0
15	-29.4	-18.8
16	-26.1	-19.1
17	-28.1	-29.7
18	-37.0	-38.2
19	-33.5	-24.5
20	-28.7	-22.9
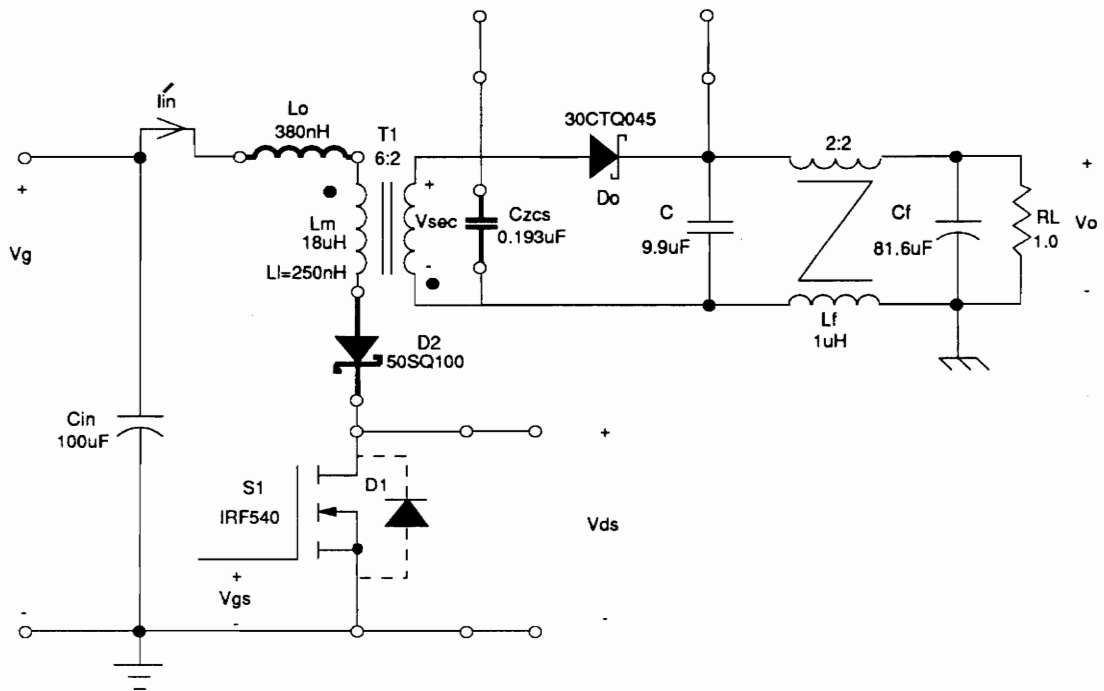
Figure 3.5. **Schematic of the experimental flyback ZCS-QRC circuit**
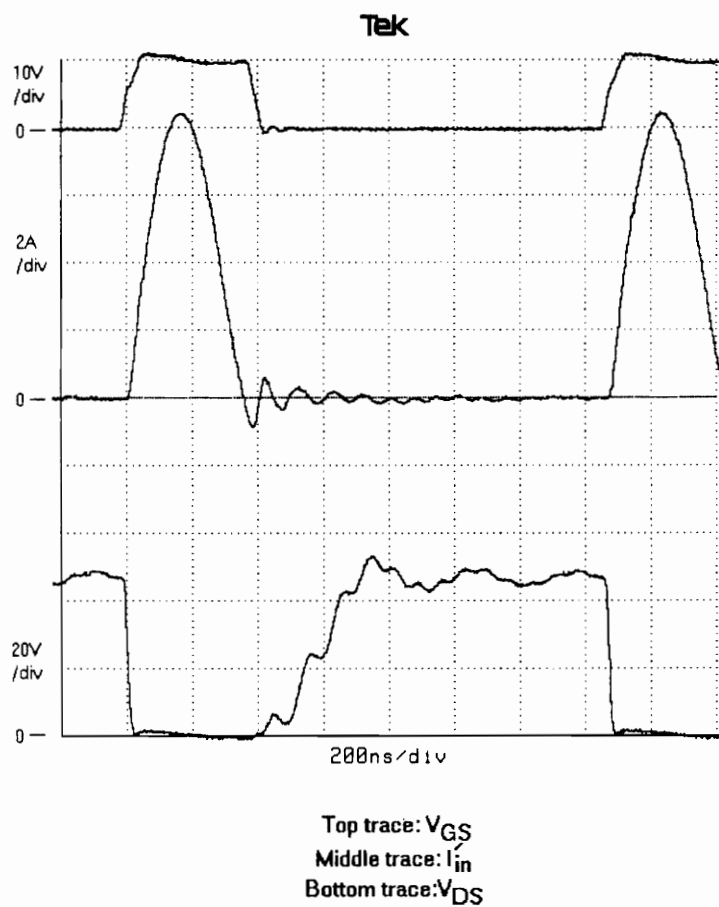
Figure 3.6.   Waveforms of the experimental flyback ZCS-QRC circuit
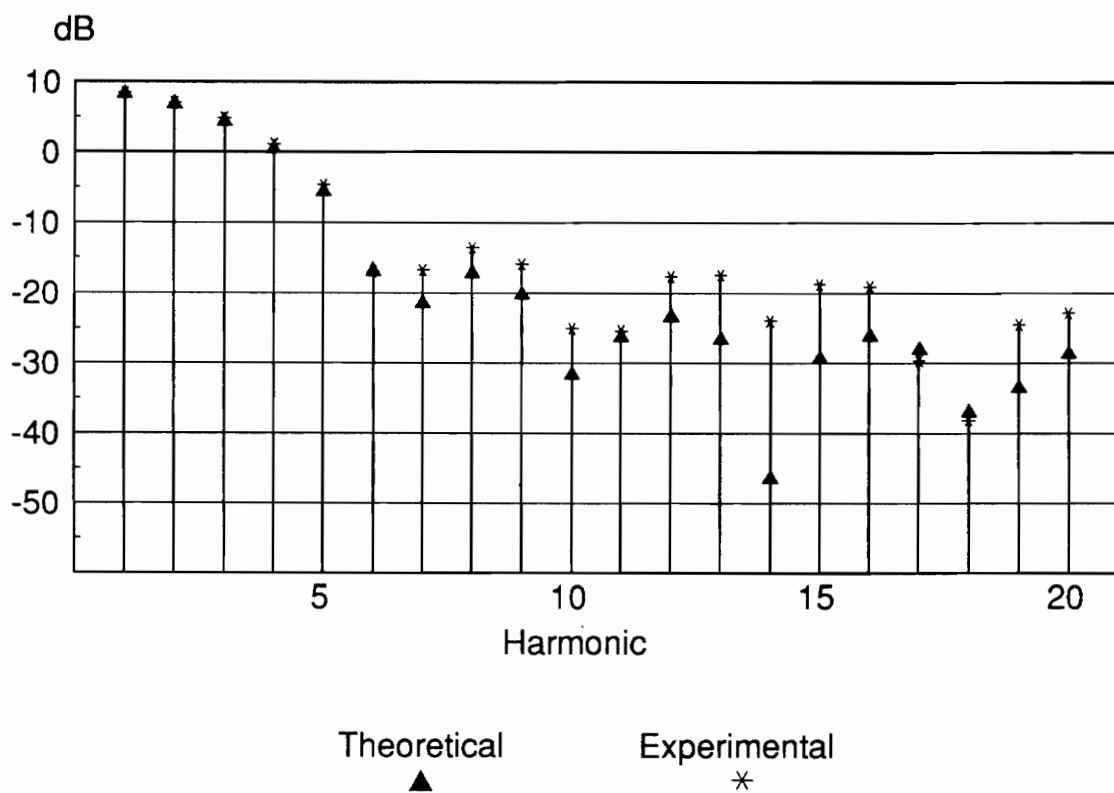
Figure 3.7. Overplot of experimental and theoretical spectral components
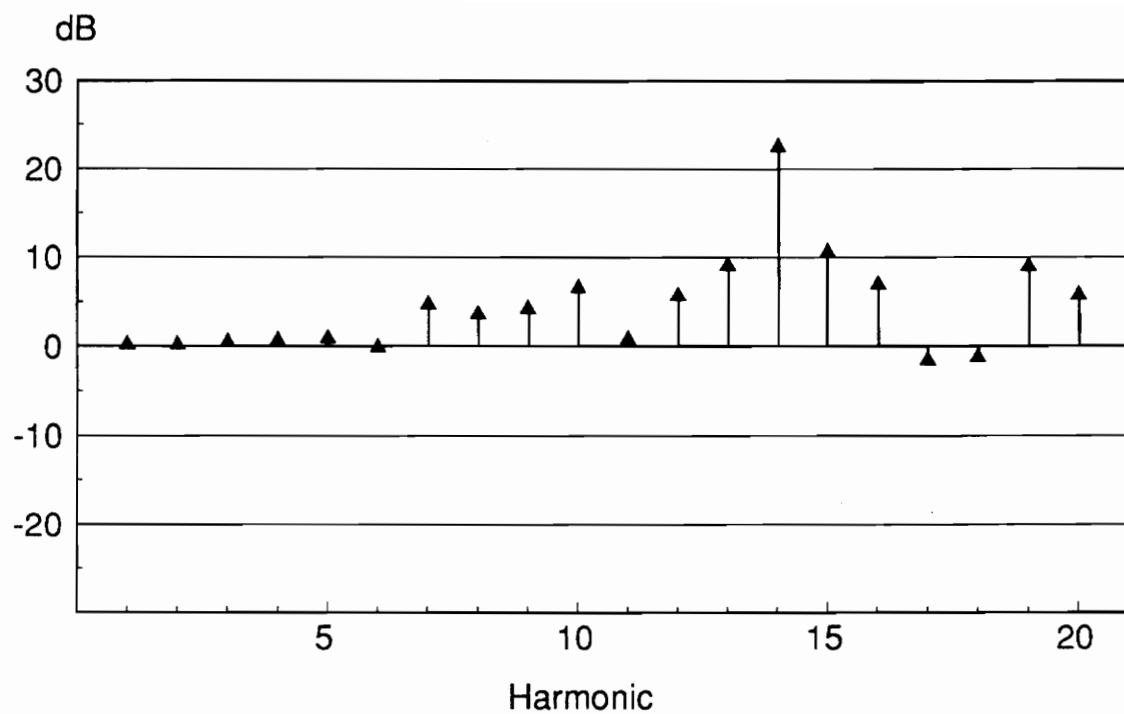
Figure 3.8. Theoretical spectral magnitudes subtracted from experimental spectral magnitudes

3.7 A Theoretical Example

To examine the change in the spectrum as a function of line and load conditions, a numerical example will be presented. For this example, assume the following operating conditions:

- $V_g = 21\,V$ to $32\,V$

- $V_{g,nominal} = 24\,V$

- $V_o = 5\,V$

- $I_o = 1\,A$ to $5\,A$

- $f_{s,max} = 1\,MHz$

- $n = 3\,turns$

- $\xi_c = 1.0$

The values of the resonant tank elements were calculated using the procedure described in [2]. The component values of the resonant tank are:

- $f_o = 2.4\,MHz$, and

- $Z_o = 4.2\,\Omega$

Also, assume that the converter operates in half-wave mode.

Six specific cases are of interest: low-line light-load, low-line full-load, nominal-line light-load, nominal-line full-load, high-line light-load, high-line full-load. The spectral data of these 6 cases were computed and graphed in Figs. 3.9 (a-f)

When examining Fig. 3.9, it is evident that the flyback ZCS-QRC spectrum exhibits a strong relationship to line/load conditions. Although there is a dependency on the line conditions, there is a much stronger sensitivity on the load conditions. This strong sensitivity is shown in the analytical equations because the load current is directly proportional to the magnitude of the spectral components.
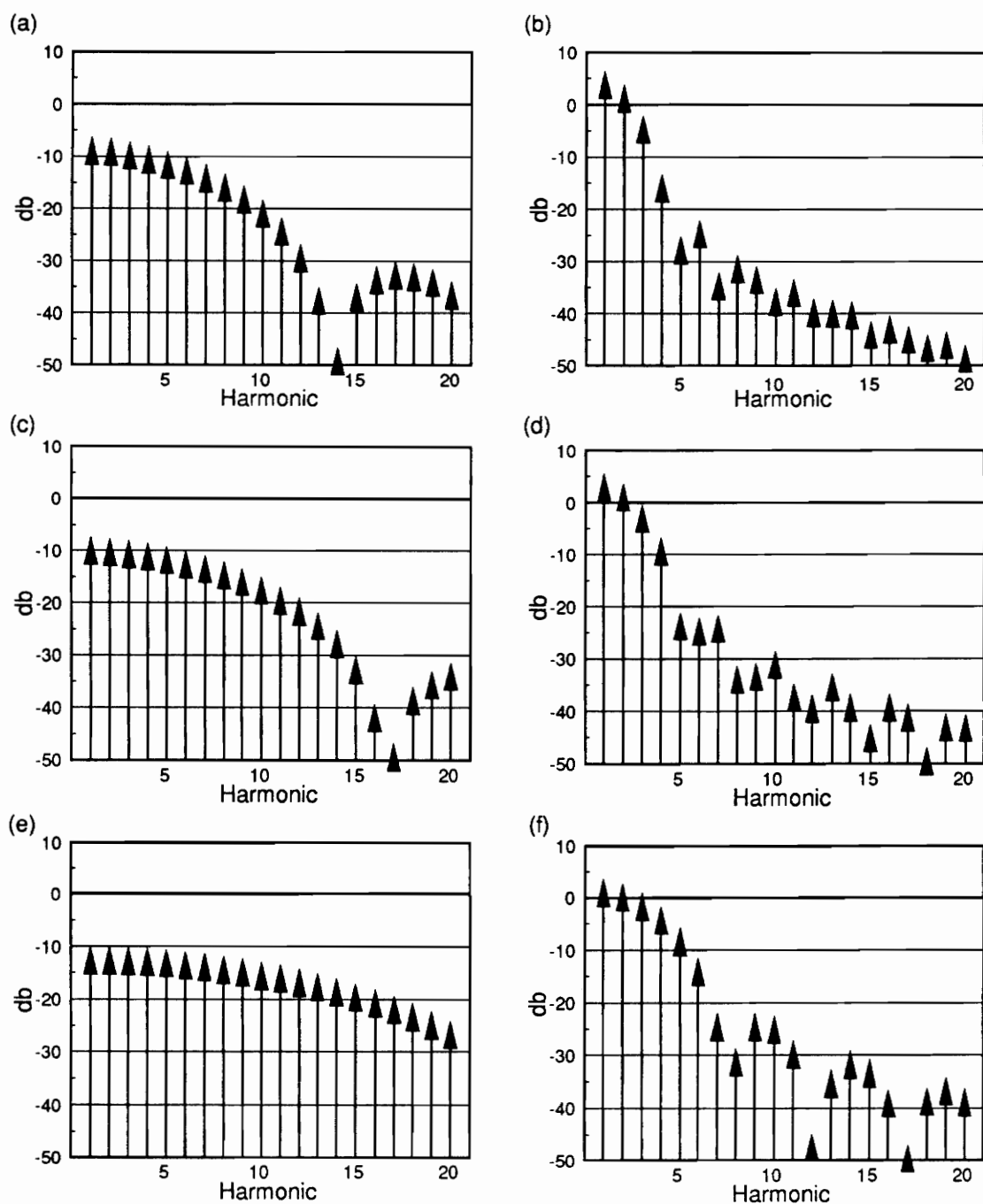
Figure 3.9. Spectrum for different cases of the flyback ZCS-QRC: (a) low-line and light-load, (b) low-line and full-load, (c) nominal-line and light-load, (d) nominal-line and full-load, (e) high-line and light-load, and (f) high-line and full-load

3.8 Comparisons to PWM

3.8.1 Comparison of Numerical Examples

The theoretical example presented in the previous section was for a well-designed ZCS-QRC where Q_{min} / M_{max} = 1. This is similar to theoretical examples presented for the PWM converter in Section 1.6 where $\xi = \xi_c = 0.1$ for a well-designed PWM converter. Therefore the two sets of results (plots) can be compared.

The spectrum of the PWM converter is very different than the spectrum of the ZCS-QRC for the example presented. One difference is the dependency on line/load conditions. The spectrum of the ZCS-QRC appears to be completely different for each condition shown, whereas the spectrum of the PWM converter only changes significantly with a change in the load condition.

Another difference between the two sets of spectrums is the slope of the envelopes. For most cases, the ZCS-QRC spectrum stays significant at low harmonics but rapidly declines at higher harmonics; however, the PWM spectrum decreases rapidly at first and stays relatively constant at higher harmonics.

When designing the input filter, remember that the PWM converter will usually have the general shape as shown in Chapter 2, but the ZCS converter has a dependence on line and load conditions. If this variation is small (smaller than the case shown) so that the variation of the switching frequency is small, the spectrum will be much better in ZCS-QRC than in PWM.

3.8.2 Comparison of Analytical Equations

To compare the analytical results of the ZCS-QRC to the PWM converter, a ratio can be used. Define the variable r as the ratio of the input current spectrum of the flyback ZCS-QRC to the input current spectrum of the flyback PWM converter. That is:

$$r = \frac{(c'_m)_{zcs}}{(c'_m)_{pwm}} \quad . \tag{3.61}$$

From [2], it is known that for a flyback ZCS-QRC the peak resonant input current is dependent on line variation when the converter is operated in its buck region, but is independent of line variation when operated in its boost region ($M > 1$). Therefore, for this comparison, conversion ratios greater then one will be used. Also in this comparison, only the worst case will be considered because this is what a converter is typically designed for. For both the PWM and ZCS converters, the worst case occurs at low line and full load (M_{max}, Q_{min}). The ratio r was computed for a given M_{max} and m by using (2.25) and (3.59) (note that for each M_{max}, a new resonant tank had to be calculated using the algorithm shown in [2]). A 3-D plot showing r as a function of M_{max} and the harmonic number m is shown in Fig. 3.10.

There are several interesting points to make about Fig. 3.10. The first concerns the reason why r is very large at the second harmonic for low values of M_{max}. This is not so much because the second harmonic of the ZCS-QRC is large, but more because the second harmonic of the PWM converter is small, thus the ratio r is large.

Another interesting point about Fig. 3.10 is that for the first harmonic ($m = 1$), r keeps increasing as M_{max} increases. This is because as M becomes large, so does the ratio of the switching frequency to the resonant frequency [2]:

$$\frac{f_s}{f_o} = \frac{M_{max}}{1 + M_{max}} \quad . \tag{3.62}$$

As this ratio increases, the current will take nearly the whole switching cycle to complete one resonant cycle. This forces the amplitude of the fundamental harmonic to become larger and the ratio r to increase. In contrast, for PWM converters, as M_{max} increases, so does the duty cycle D because:

$$D = \frac{M_{max}}{1 + M_{max}} \quad . \tag{3.63}$$

Therefore, as D increases, the amplitude of the fundamental decreases because the input current almost appears as a DC current.

Finally, it is interesting to note that besides the first two harmonics, the ratio r is always less than one. In fact, for the most part, the ratio r is close to zero, demonstrating that the spectrum for the flyback PWM converters is much less than the spectrum for a flyback ZCS-QRC for a given $M_{max} \geq 1$. This is important to know when considering the input filter for a converter because it is typically much easier to filter out the first few harmonics than to filter out a broad range of harmonics. Also, even though r may be greater than one for the first two harmonics, the spectrum of the flyback ZCS converter decreases faster than the spectrum of the flyback PWM converter.
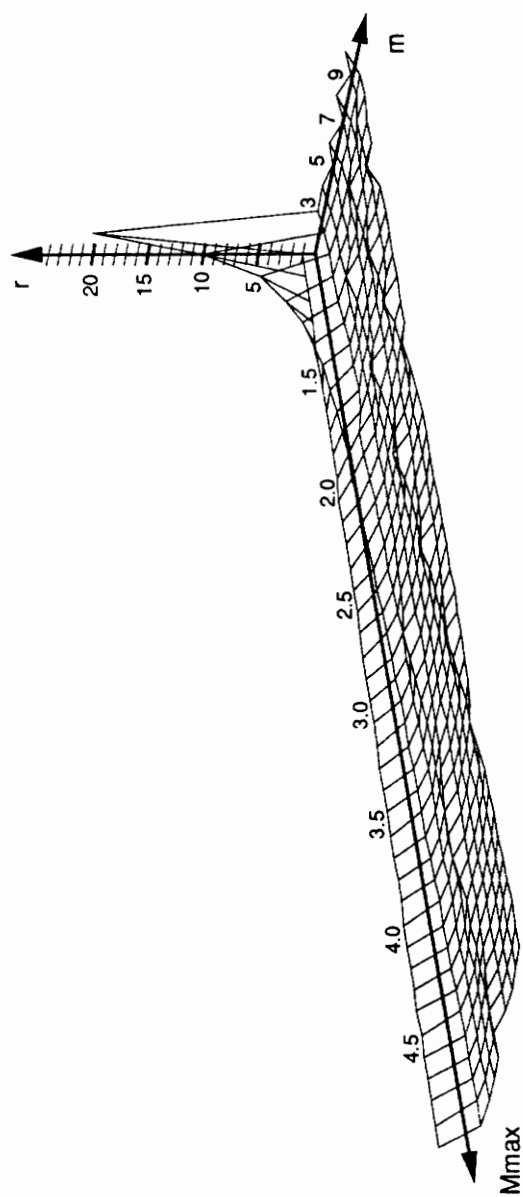
Figure 3.10. Ratio of flyback ZCS-QRC spectrum to flyback PWM spectrum

3.8.2.1 Approximation for Operation in Boost Region

According to [2], when the flyback ZCS-QRC operates in the boost region ($M_{max} \geq 1$), the converter equations are independent of percent line-load variation. At the worst-case condition of $Q_{min}/M_{max} = 1$, it would be advantageous to have an equation that could describe the first few harmonics in simple analytical terms. By simplifying the complex expressions for the input current spectrum of the ZCS-QRC, values could be obtained without the help of a computer.

For ZCS-QRC converters, zero current switching is guaranteed as long as $Q_{min} / M_{max} \geq 1$. At the boundary condition when $Q_{min} / M_{max} = 1$, the input current is about to lose zero current switching. That is, the input current has a slope of zero and a value of zero at the end of the on-time. For a smaller value of Z_o, $Q_{min} / M_{max} < 1$, and the input current will not be able to ring back down to zero. In a well-designed converter, this boundary condition marks the point of low-line and full-load, which according to [4] is the place of maximum current stress; therefore, it would be desirable to find the spectrum at the boundary condition.

At the point of $Q_{min}/M_{max} \simeq 1$, the peak input current is twice the inductor current of I_x. Also, as M_{max} increases, so does the effective on-time ratio of the converter which is given by:

$$\frac{f_s}{f_o} = \frac{M_{max}}{M_{max} + 1} \quad . \tag{3.64}$$

One way to simplify the equations is to approximate the actual waveform. After several attempts, a raised sine wave (a sine wave with a DC bias) was found to offer a sufficient approximation for the ZCS-QRC input current spectrum for low harmonics. Consider a raised sine wave of the following form:

$$f(t) = I_x + I_x \sin \omega_o t \qquad -t_0 < t < t_1 \quad , \tag{3.65}$$

where I_x is defined as in the previous sections. A plot of $f(t)$ is shown in Fig. 3.11.

The variable ω_o can be found from (3.64) as:

$$\omega_o = 2\pi f_s \frac{M_{max} + 1}{M_{max}} \quad . \tag{3.66}$$

The variables t_0 and t_1 can be found by observing that they occur when $-\omega_o t_0 = -\pi/2$ and $\omega_o t_1 = 3\pi/2$, respectively. Therefore, t_0 and t_1 are defined as:

$$t_0 = \frac{M_{max} T_s}{4(M_{max} + 1)} \quad , \tag{3.67}$$

$$t_1 = \frac{3M_{max} T_s}{4(M_{max} + 1)} \quad . \tag{3.68}$$

Using (3.67) and (3.68), the Fourier coefficients can be found (Appendix B). They are:

$$a_m = \frac{4I_x}{m\pi} \frac{(M_{max} + 1)^2}{(M_{max} + 1)^2 - m^2 M_{max}^2} \left(\sin x_m t_0 - \sin^3 x_m t_0 \right) \quad , \tag{3.69}$$

$$b_m = \frac{4I_x}{m\pi} \frac{(M_{max} + 1)^2}{(M_{max} + 1)^2 - m^2 M_{max}^2} \left(\cos x_m t_0 - \cos^3 x_m t_0 \right) \quad , \tag{3.70}$$

where

$$m \neq \frac{M_{max} + 1}{M_{max}} \quad , \tag{3.71}$$

and

$$a_m = 0 \quad , \tag{3.72}$$

$$b_m = I_x \frac{M_{max}}{M_{max} + 1} \quad , \tag{3.73}$$

where

$$m = \frac{M_{max} + 1}{M_{max}} \quad .$$

(3.74)

It is interesting to note that since $M_{max} \geq 1$ is of interest, and m is an integer greater than or equal to one, the only time the equality of (3.72) and (3.73) is valid is when both $m = 2$ and $M_{max} = 1$.

Squaring a_m and b_m, adding together and then taking the square root, will give the magnitude of each coefficient. From Appendix B, the final result is:

$$c_m = \begin{cases} \left| \dfrac{2I_x}{m\pi} \dfrac{(M_{max} + 1)^2}{(M_{max} + 1)^2 - m^2 M_{max}^2} \sin\left(\dfrac{m\pi M_{max}}{M_{max} + 1} \right) \right| & m \neq \dfrac{M_{max} + 1}{M_{max}} \\[4ex] I_x \dfrac{M_{max}}{M_{max} + 1} & m = \dfrac{M_{max} + 1}{M_{max}} \end{cases}$$

(3.75)

which can be written as:

$$c_m = \begin{cases} \left| \dfrac{2I_x}{m\pi} \dfrac{\sin\left(\dfrac{m\pi M_{max}}{M_{max} + 1} \right)}{1 - \left(\dfrac{m}{1 + \dfrac{1}{M_{max}}} \right)^2} \right| & m \neq \dfrac{M_{max} + 1}{M_{max}} \\[6ex] I_x \dfrac{M_{max}}{M_{max} + 1} & m = \dfrac{M_{max} + 1}{M_{max}} \end{cases}$$

(3.76)

The above relation gives an approximation for the spectrum of the input current for the flyback ZCS-QRC. Because the sine wave approximation is only an approximation to the actual waveform, (3.75) is only valid at the lower harmonics for $M_{max} \geq 1$ and $Q_{min}/M_{max} \simeq 1$.
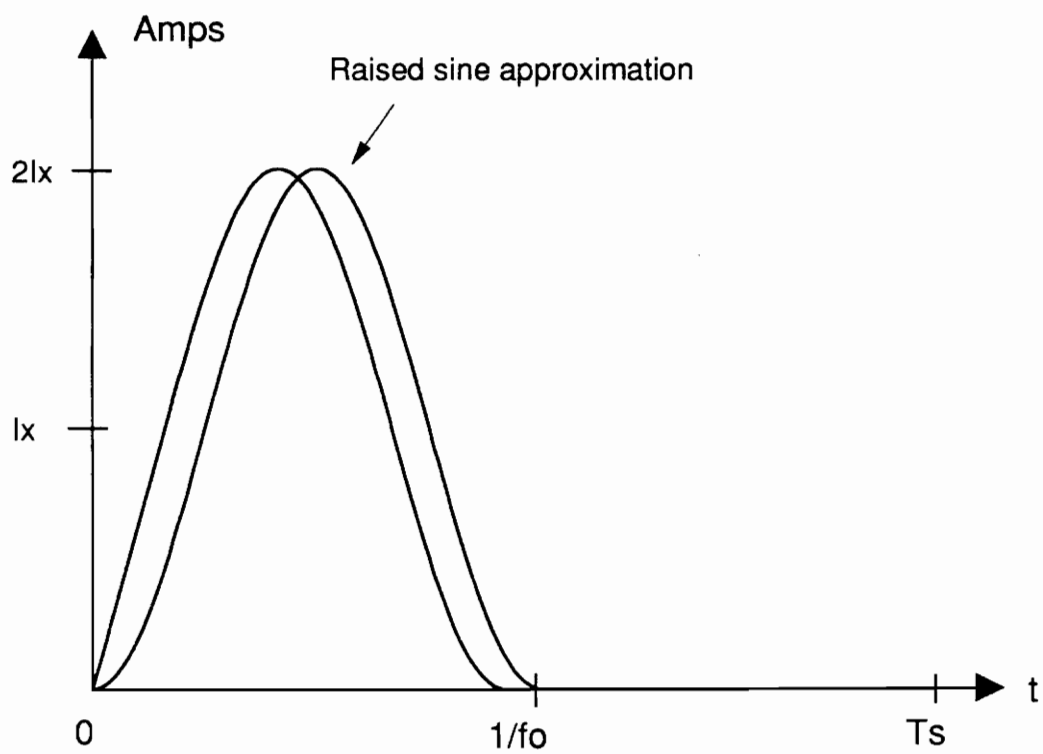
Figure 3.11. Raised sine wave approximation shown with the actual theoretical waveform

3.8.2.2 Approximation of Ratio of ZCS-QRC Spectrum to PWM Spectrum

To find a meaningful approximation for the ratio r of the input current spectrum of the flyback ZCS-QRC to the input current spectrum of the flyback PWM converter, several items need to be considered. First, the only point of interest would be for the worst-case design point: for PWM at $\xi = \xi_c$ and for ZCS-QRC at $Q_{min}/M_{max} \simeq 1$. At $Q_{min}/M_{max} \simeq 1$, the ZCS-QRC has the following approximation for the on-time ratio:

$$\frac{f_s}{f_o} = \frac{M_{max}}{M_{max} + 1} \quad , \tag{3.77}$$

while for the PWM converter, the on-time ratio is:

$$D = \frac{M_{max}}{M_{max} + 1} \quad . \tag{3.78}$$

Therefore, by taking the ratio r at $Q_{min}/M_{max} \simeq 1$, the amount of time the switch is on allowing the current to flow is comparable.

Also, to avoid the problems associated with percent line-load variation of ZCS-QRC [2], only the flyback converter operating in the boost region ($M_{max} \geq 1$) will be considered.

Using (2.24) for the input current spectrum of the PWM converter and (3.75) for an approximation of the input current spectrum for the ZCS-QRC, the ratio r can be written as:

$$r = \begin{cases} \left| \dfrac{\dfrac{\sin \theta_m}{\sqrt{\gamma}}}{1 - \left(\dfrac{m}{1 + \dfrac{1}{M_{max}}} \right)^2} \right| & m \neq \dfrac{M_{max} + 1}{M_{max}} \\[40pt] \dfrac{\pi}{2} \dfrac{1}{\sqrt{\gamma}} & m = \dfrac{M_{max} + 1}{M_{max}} \end{cases} , \qquad (3.79)$$

where

$$\gamma = \left(1 + \frac{\xi_c^2}{\theta_m^2} \right) \sin^2 \theta_m + \xi_c^2 \cos^2 \theta_m - \frac{\xi_c^2}{\theta_m} \sin 2\theta_m , \qquad (3.80)$$

and

$$\theta_m = m\pi \frac{M_{max}}{M_{max} + 1} . \qquad (3.81)$$

Also, ξ_c is a very small number (on the order of 0.1) [2]. Since ξ_c is relatively small and $M_{max} \geq 1$, the following approximation can be made:

$$\gamma \simeq \sin^2 \theta_m , \qquad (3.82)$$

for

$$m \neq \frac{M_{max} + 1}{M_{max}} . \qquad (3.83)$$

At the condition, when $m = 2$ and $M_{max} = 1$, θ_m becomes π and γ becomes ξ_c^2. Therefore, the ratio r can now be written as:

$$
r = \begin{cases} \left| \dfrac{1}{1 - \left(\dfrac{m}{1 + \dfrac{1}{M_{max}}} \right)^{2}} \right| & m \neq \dfrac{M_{max} + 1}{M_{max}} \\[2em] \dfrac{\pi}{2} \dfrac{1}{\xi_c} & m = \dfrac{M_{max} + 1}{M_{max}} \end{cases} \tag{3.84}
$$

Table 3.2 shows both the theoretical ratio and the approximated ratio of the ZCS-QRC spectrum to the PWM spectrum for $M_{max} \geq 1$, $1 \leq m \leq 5$. The percent errors shown in the table are relatively low for the first two harmonics. For the harmonic numbers greater than 2, the percent errors increase significantly. The percent errors are relatively large for higher harmonics because of the two approximated waveforms. When γ was approximated as $\sin^2\theta_m$, the effect of the input current ripple was basically neglected; i.e., the input current waveform for the PWM converter was approximated as a square wave. Also adding to the percent errors of the higher harmonics is the shape and duration of the approximated waveform. With this approximation, the lower two harmonics contain most of the information about the height of the waveform, but the higher harmonics make up the smaller details (such as the differences caused by the linear charging stage and the actual time duration of the resonant current). Although some of the percent errors are relatively large, the approximation can still be used to issue a conservative guess of the actual spectral ratio. Also, the fact that the magnitudes of the harmonics where $m \geq 3$ are larger in the flyback PWM converter than in the flyback ZCS-QRC converter is preserved.

These equations do show certain insight into the ratio of the input current spectrum of the flyback PWM converter to the input current spectrum of the flyback ZCS-QRC converter. For instance, both the theoretical ratio as well as the approximated ratio show that the magnitude

of the first harmonic of a well-designed ZCS-QRC spectrum operating at $Q_{min}/M_{max} \simeq 1$ is always larger than the magnitude of the first harmonic of a well-designed PWM spectrum operating at low line and full load for $M_{max} \geq 1$. Also, the approximated ratio shows the strong dependence on M_{max}. This dependence causes the first harmonic to continually increase for an increase in M_{max}.

A third item to consider is effect of the ripple current on the ratio at the point of $m = 2$ and $M_{max} = 1$. At this condition, the PWM input current waveform has a duty cycle of 0.5. As ξ_c approaches 0, the current waveform of the PWM converter approaches an ideal square wave. It is known [9] and shown later in Chapter 5 that the second harmonic (and subsequent even number harmonics) is zero. Therefore, as ξ_c decreases, the second harmonic of the PWM converter decreases and the ratio increases. This dependence on ξ_c can be seen clearly in equation (3.84).

Table 3.2. Theoretical, approximated, and percent error values of the ratio of the ZCS-QRC spectrum to the PWM spectrum

	m = 1			m = 2		
Mmax	Approxi-mation (Amps)	Theor-etical (Amps)	Error (%)	Approxi-mation (Amps)	Theor-etical (Amps)	Error (%)
1.0	1.33	1.38	-3.6	15.7	17.1	-7.7
1.2	1.42	1.48	-3.9	5.26	5.49	-4.2
1.4	1.52	1.58	-4.0	2.77	3.02	-8.2
1.6	1.61	1.68	-4.2	1.94	2.14	-9.4
1.8	1.70	1.78	-4.3	1.53	1.70	-10.1
2.0	1.80	1.88	-4.4	1.29	1.44	-10.5
2.2	1.90	1.98	-4.5	1.12	1.26	-10.8
2.4	1.99	2.09	-4.5	1.01	1.13	-11.1
2.6	2.09	2.19	-4.6	0.921	1.04	-11.2
2.8	2.19	2.29	-4.6	0.853	0.962	-11.3
3.0	2.29	2.40	-4.6	0.800	0.903	-11.4

	m = 3			m = 4		
Mmax	Approxi-mation (Amps)	Theor-etical (Amps)	Error (%)	Approxi-mation (Amps)	Theor-etical (Amps)	Error (%)
1.0	0.800	0.903	-11.4	0.333	0.638	-47.8
1.2	0.596	0.668	-10.7	0.266	0.451	-41.0
1.4	0.485	0.524	-7.5	0.225	0.362	-37.9
1.6	0.415	0.404	2.8	0.198	0.314	-37.1
1.8	0.368	0.244	50.8	0.178	0.280	-36.4
2.0	0.333	0.638	-47.8	0.164	0.252	-35.0
2.2	0.307	0.630	-51.2	0.152	0.224	-31.9
2.4	0.287	0.520	-44.8	0.143	0.192	-25.5
2.6	0.271	0.464	-41.7	0.136	0.159	-14.2
2.8	0.257	0.429	-40.0	0.130	0.211	-38.3
3.0	0.246	0.404	-39.1	0.125	0.652	-80.8

	m = 5		
Mmax	Approxi-mation (Amps)	Theor-etical (Amps)	Error (%)
1.0	0.191	0.302	-36.9
1.2	0.155	0.232	-32.9
1.4	0.133	0.155	-14.2
1.6	0.118	0.456	-74.1
1.8	0.107	0.318	-66.4
2.0	0.099	0.286	-65.4
2.2	0.092	0.272	-66.0
2.4	0.087	0.266	-67.2
2.6	0.083	0.266	-68.7
2.8	0.080	0.270	-70.5
3.0	0.077	0.281	-72.7

3.9 Extension to Other Converters

Because of the way that the equations have been defined and derived, they can be extended to other families of converters, such as the buck ZCS-QRC and the boost ZCS-QRC.

In [1], it is shown that the general shape of the input current for the buck ZCS-QRC and the boost ZCS-QRC is similar to the flyback ZCS-QRC presented in this chapter. In fact, only changes in the definitions of the variables of (3.53) to (3.58) need to be made.

3.10 Summary

In this chapter, the flyback ZCS-QRC was considered. For this converter, the input current spectrum was derived in terms of external parameters. The final analytical equations of the input current spectrum were displayed in a normalized fashion: that is, they were displayed so that the inductor current term could be omitted.

The experimental results were shown to be accurate when eliminating parasitic effects such as ringing on the secondary.

Also in this chapter, the same theoretical example used in the PWM chapter was used here. Plots were shown for different line/load conditions. The plots were compared to the PWM case, and similarities and differences were discussed.

Finally, a comparison of the analytical equations of PWM and ZCS was made. Several interesting points concerning the ratio of the input current spectrum of ZCS to PWM for a given M_{max} greater than one were discussed.

Chapter 4

Zero-Voltage-Switched Quasi-Resonant-Converter

(ZVS-QRC)

4.1   Introduction

In PWM operation, the voltage across the main power switch changes abruptly during turn-on. This, coupled with the junction capacitance of a MOSFET, causes high switching losses in the circuit. These turn-on losses could be avoided if the switch is turned on with zero volts across it. To do this, a resonant tank is employed to help shape the voltage waveform during the off-time so that a zero voltage condition occurs at the end of the off-time, *i.e.* at turn-on [1].

During turn-off, the input current is diverted away from the main switch to the resonant capacitor. Since the input current is then proportional to the derivative of the resonant-capacitor voltage, the current will also be quasi-sinusoidal during the off-time. This quasi-

sinusoidal current waveform should have much lower magnitudes of the spectrum when compared to the spectrum of the choppy input current of the PWM converter.

Although this zero-voltage-switching technique can be applied to any of the basic types of converters, only the flyback converter will be studied in detail.

The equations desired are for the flyback converter. By reflecting the primary side elements of the flyback converter to the secondary side, an equivalent converter can be constructed. The final equations presented here will be for a flyback ZVS-QRC.

4.2   Flyback ZVS-QRC

Figure 4.1 shows a schematic of a flyback ZVS-QRC. The reactive elements L_o and C_o make up the resonant tank that ultimately shapes the switch voltage waveform.

The anti-parallel diode, D_1, of switch S_1 is shown because it plays an important role in the shaping of the voltage waveform of the resonant capacitor (and switch). As the voltage across capacitor C_o resonates, it will eventually forward bias the anti-parallel diode and clamp the voltage across the switch at zero (ideally). This is known as half-wave mode operation. The switch then should be turned on at zero voltage.

Also shown in Fig. 4.1 is the output stage for the flyback converter, D_0, C_f, and R_L.

To find an equivalent circuit of Fig. 4.1, reflect the primary side elements to the secondary side. The resonant inductor (L_o) and the resonant capacitor (C_o) are scaled down and up, respectively, by the square of the turns ratio n. Also, the input voltage (V_g) is scaled down by the turns ratio, while the input current (I'_{in}) is scaled up by the turns ratio.

The ideal switch S_1 and diode D_1 transfer to the secondary without any change. Now all of the components have been defined for use in the secondary side. The flyback converter has now been reduced to the equivalent circuit shown in Fig. 4.2.

In Fig. 4.2, L_r and C_r make up the resonant tank. Diodes D_0 and D_1, switch S_1, capacitor C_f, and resistor R_L contribute in the same way as they did for the flyback converter of Fig. 4.1.

Element L_f, usually a relatively large inductance, serves as part of the output filter. This inductance can be represented in a flyback converter as the secondary side inductance of the

transformer. Since the inductance is relatively high, L_f acts as a current source during normal operation.

The elements L_r, C_r, V_i, and I_{in} of Fig. 4.2 can be written in terms of the notation used for the flyback converter of Fig. 4.1. The basic transformations are:

$$L_r = \frac{L_o}{n^2} \, , \tag{4.1}$$

$$C_r = n^2 C_o \, , \tag{4.2}$$

$$V_i = \frac{V_g}{n} \, , \tag{4.3}$$

and

$$I_{in} = n I'_{in} \, , \tag{4.4}$$

where n is defined as the turns ratio.

For the circuit of Fig. 4.2, the key circuit parameters, namely characteristic impedance, resonant angular frequency, and conversion ratio are known to be:

$$Z_o = \sqrt{\frac{L_r}{C_r}} \, , \tag{4.5}$$

$$\omega_o = \sqrt{\frac{1}{L_r C_r}} \, , \tag{4.6}$$

$$M = \frac{V_o}{V_i} \, , \tag{4.7}$$

respectively.

Also, define Q as the normalized load resistance; *i.e.*, the ratio of the output load resistance to the characteristic impedance:

$$Q = \frac{R_L}{Z_o} \quad .$$

(4.8)

Now that the global variables have been formally defined, following is a description of the operation.
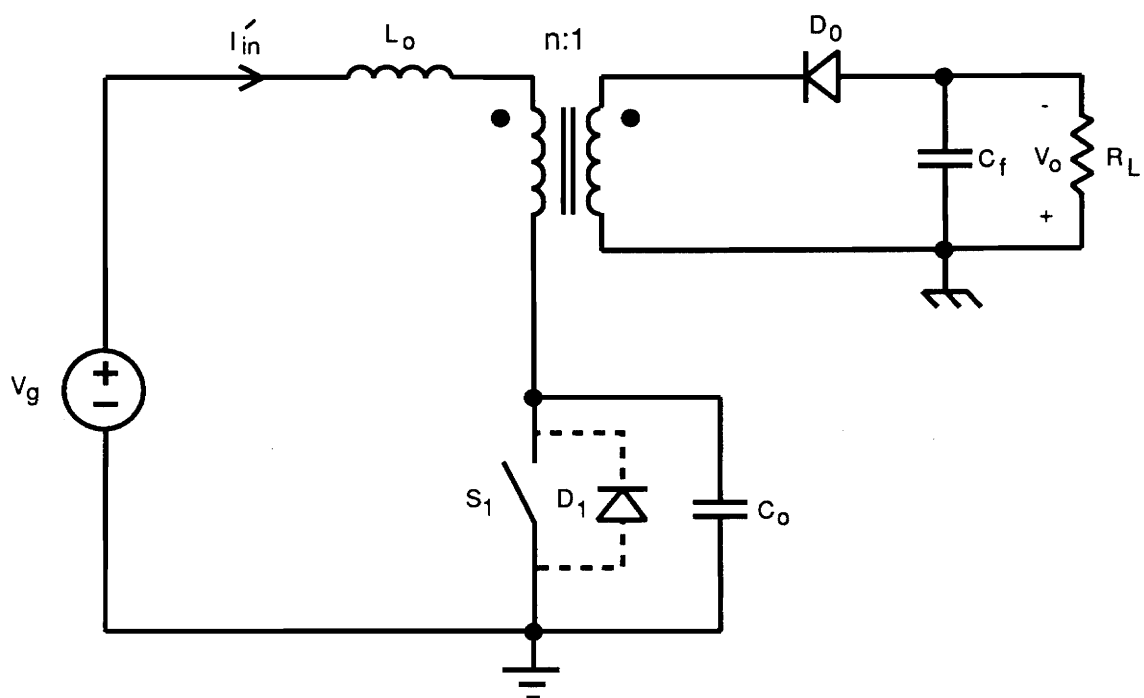
Figure 4.1. Circuit diagram of a flyback ZVS-QRC
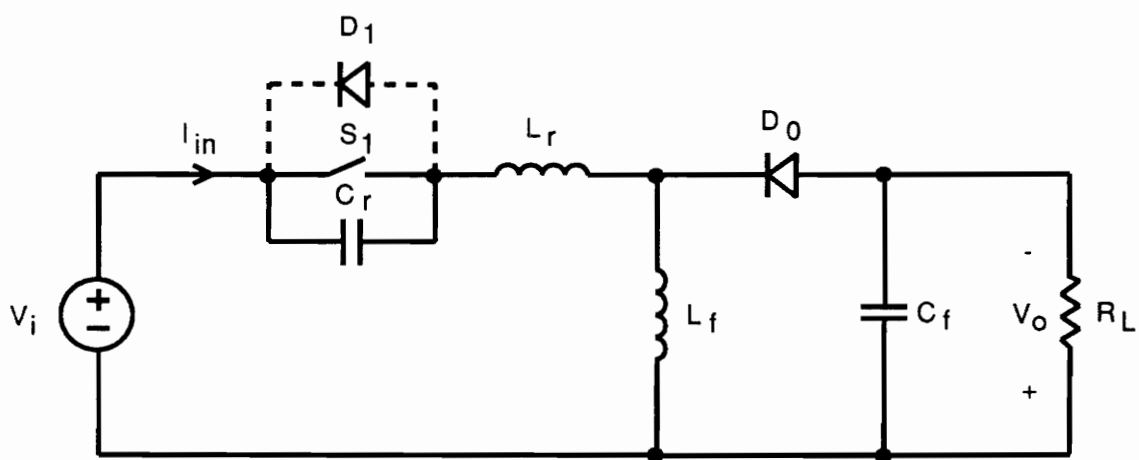
Figure 4.2. Circuit diagram of an equivalent flyback ZVS-QRC

4.3 Stages of Operation

Similar to the boost converter presented in [1], the flyback converter can also be divided into four stages during each switching cycle. The stages are used to describe the circuit during intervals of the switching period. For the different stages, the state equation(s) can be found and solved.

For the converter shown in Fig. 4.2, the inductor L_f is considered to be large so that it acts as a constant current source of magnitude I_x. From [1], I_x is found to be:

$$I_x = \frac{M}{Q}\frac{V_i + V_o}{Z_o} \quad , \tag{4.9}$$

where M, Q, Z_o are defined in Section 4.3.

Initially, assume that all of the current, I_x, circulates through S_1, L_f, and V_i. Diode D_0 is initially off so that no current is being delivered to the load. The operation of the circuit can be described by the following four stages:

- STAGE 1. Capacitor-Charging Stage $[T_0, T_1]$

  At time T_0, switch S_1 opens, and the current begins to charge capacitor C_r. The capacitor continues to charge until the voltage across it, V_{C_r}, reaches $V_o + V_i$.

  The initial condition and the governing state equation for this stage are:

  $$V_{C_r}(0) = 0 \quad , \tag{4.10}$$

  $$C_r\frac{dV_{C_r}}{dt} = I_x \quad . \tag{4.11}$$

At time T_1, diode D_0 is no longer reverse biased, and it begins to conduct. Time T_1 signifies the end of this stage. The duration of this stage is found to be:

$$T_{01} = C_r \frac{V_o + V_i}{I_x} \quad .$$

(4.12)

The equivalent circuit of the capacitor-charging stage is shown in Fig. 4.3(a).

• STAGE 2 . Resonant Stage [T_1, T_2] :

At time T_1, diode D_0 conducts and begins to build up current from I_x. As the current through D_0 increases, the current through L_r decreases (so that I_x remains constant) . The reactive elements L_r and C_r now begin to resonate, and a quasi-sinusoidal voltage forms across C_r . In half-wave mode operation, after V_{C_r} reaches zero (at time T_2), switch S_1 turns on.

The initial conditions and state equations for this stage are:

$$I_{L_r}(0) = I_x \quad ,$$

(4.13)

$$V_{C_r}(0) = V_o + V_i \quad ,$$

(4.14)

and

$$L_r \frac{dI_{L_r}}{dt} = V_i + V_o + V_{C_r} \quad ,$$

(4.15)

$$C_r \frac{dV_{C_r}}{dt} = I_{L_r} \quad ,$$

(4.16)

respectively. The following time-dependent solutions are found:

$$I_{L_r}(t) = I_x \cos \omega_o t \quad ,$$

(4.17)

$$V_{C_r}(t) = V_i + V_o + Z_o I_x \sin \omega_o t \quad . \tag{4.18}$$

Time T_2 is the time when $V_{C_r} = 0$. With this condition, it can be seen that the duration of the resonant stage, T_{12}, is

$$T_{12} = \frac{\alpha}{\omega_o} \quad , \tag{4.19}$$

where,

$$\alpha = \sin^{-1}\left(\frac{-V_i - V_o}{Z_o I_x}\right) \quad . \tag{4.20}$$

It is also important to note that since the circuit operates in the half-wave mode, α is defined as:

$$\pi < \alpha < \frac{3\pi}{2} \quad . \tag{4.21}$$

An equivalent circuit of the resonant stage is shown in Figure 4.3(b).

- STAGE 3 . Inductor-Charging Stage [T_2, T_3] :

At time T_2, switch S_1 turns on, and the current through L_r, I_{L_r}, rises linearly until $I_{L_r} = I_x$. At time T_3, when $I_{L_r} = I_x$, diode D_0 is naturally commutated. The initial condition and state equation for this stage are:

$$I_{L_r}(0) = I_x \cos(\alpha) \quad , \tag{4.22}$$

$$L_r \frac{dI_{L_r}}{dt} = V_i + V_o \quad , \tag{4.23}$$

respectively. The inductor charging stage has a duration of T_{23}, which is defined as:

$$T_{23} = \frac{1}{\omega_0} \frac{Z_o I_x}{V_i + V_o} (1 - \cos \alpha) \quad . \tag{4.24}$$

The inductor-charging stage can be represented by the circuit shown in Fig. 4.3(c).

- STAGE 4. Passive Stage [T_3, T_4]:

At time T_3, diode D_0 is cut off, and no current is delivered to the load. The current, I_x, is flowing through only V_i, S_1, and L_r. Since this current is not time varying during this stage, there is not a voltage drop across the inductor L_r:

$$L_r \frac{dI_{L_r}}{dt} = 0 \quad . \tag{4.25}$$

This stage will continue until the end of the switching cycle. Therefore, the duration of the passive stage can be described as:

$$T_{34} = T_s - T_{01} - T_{12} - T_{23} \quad , \tag{4.26}$$

where T_s is the period of the switching cycle.

An equivalent circuit of the passive stage is drawn in Fig. 4.3(d).
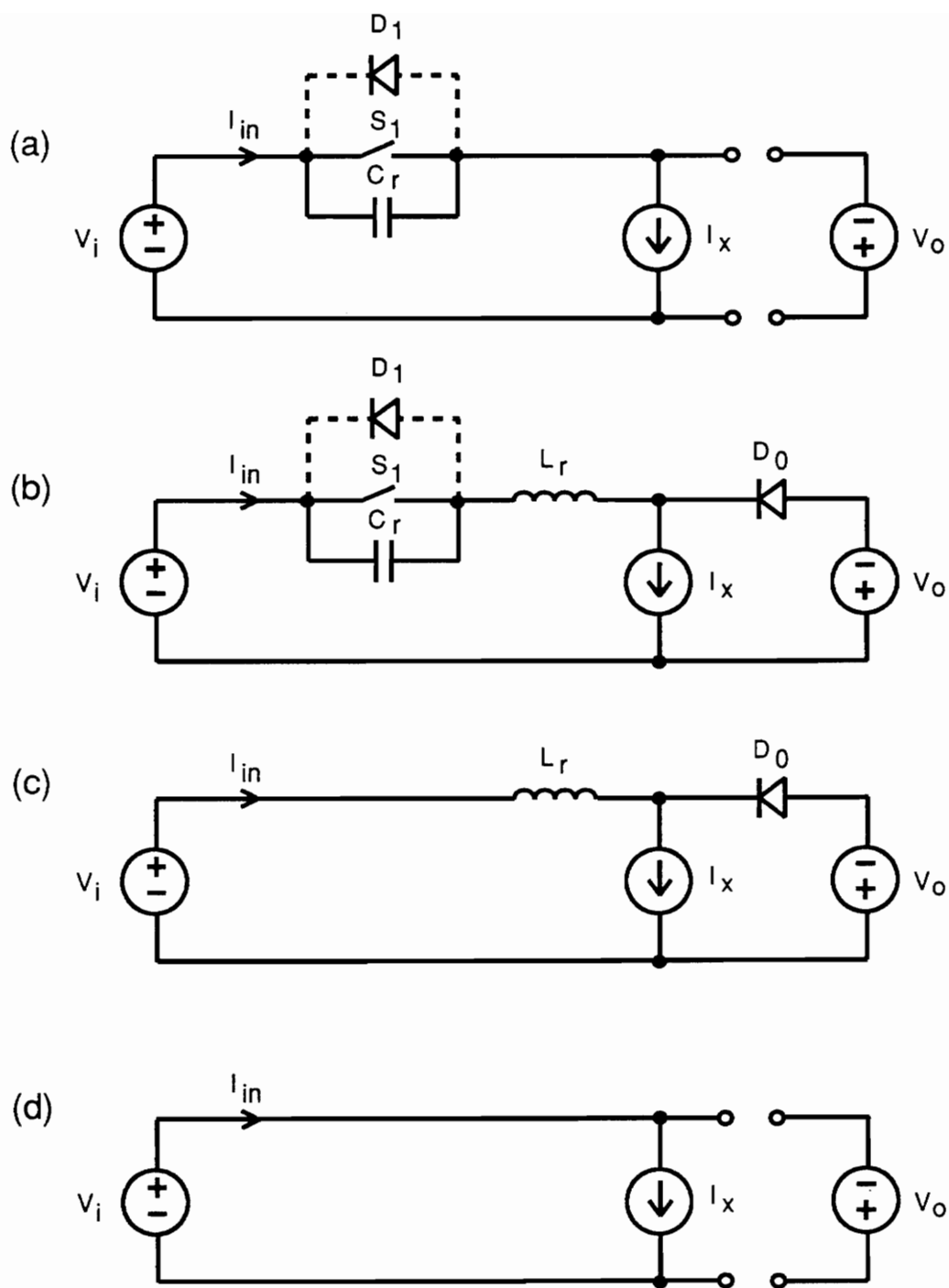
Figure 4.3. Stages of equivalent flyback ZVS-QRC: (a) capacitor-charging stage, (b) resonant stage, (c) inductor-charging stage, and (d) passive stage

4.4 Input Current Equations

The parts of the description for the input current waveform can now be assembled into one continuous function.

For the capacitor-charging stage $[T_0, T_1]$, the input current was found to be constant:

$$I_{in}(t) = I_x \quad T_0 < t < T_1 \quad .$$

(4.27)

During the resonant stage $[T_1, T_2]$, the input current was found to have the form of (4.17). But for the initial conditions of $I_{L_r}(0) = I_x$ to be met, (4.17) must be rewritten as:

$$I_{in}(t) = I_x \cos \omega_o(t - T_{01}) \quad T_1 < t < T_2 \quad .$$

(4.28)

During the inductor-charging stage, the input current was found to have a constant slope. Let y represent this constant slope:

$$y = \frac{dI_{L_r}}{dt} = \frac{dI_{in}}{dt} \quad T_2 < t < T_3 \quad ,$$

(4.29)

$$y = \frac{V_i + V_o}{L_r} \quad .$$

(4.30)

This is the slope of the input current only during the inductor charging stage. The endpoints of the input current for this interval are:

$$I_{in}(T_2) = I_x \cos \alpha \quad ,$$

(4.31)

$$I_{in}(T_3) = I_x \ , \tag{4.32}$$

where,

$$T_2 = T_{01} + T_{12} \ , \tag{4.33}$$

$$T_3 = T_{01} + T_{12} + T_{23} \ . \tag{4.34}$$

Also, α can be written as:

$$\alpha = \sin^{-1}\left(-\frac{Q}{M}\right) \ . \tag{4.35}$$

Using the endpoints and the slope, the equation of the input current for the inductor-charging stage can written as:

$$I_{in}(t) = v + y(t - T_{01} - T_{12}) \qquad T_2 < t < T_3 \ , \tag{4.36}$$

where v is the constant:

$$v = I_x \cos(\alpha) \ . \tag{4.37}$$

At time T_3 (when the input current reaches I_x), the input current stays constant until the end of the switching cycle; therefore, the input current of the passive stage can be described simply as:

$$I_{in}(t) = I_x \qquad T_3 < t < T_4 \ . \tag{4.38}$$

The total continuous representation of the input current for the converter of Fig. 4.2 can be written as:

$$I_{in}(t) = \begin{cases} I_x & T_0 < t < T_1 \\ I_x \cos \omega_o(t - T_{01}) & T_1 < t < T_2 \\ v + y(t - T_{01} - T_{12}) & T_2 < t < T_3 \\ I_x & T_3 < t < T_s \end{cases} \qquad (4.39)$$

Theoretical waveforms of the circuit of Fig. 4.2 are shown in Fig. 4.4.

The general description of the input current of the circuit shown in Fig. 4.1 is similar to that of the equivalent circuit of Fig. 4.2. In order to express the input current equation of the equivalent converter in terms of the elements of the original converter (L_o, C_o, V_g), the simple transformations found in Section 4.2 (rewritten here in (4.40) - (4.42)) need to be used in (4.39).

$$L_r = \frac{L_o}{n^2} , \qquad (4.40)$$

$$C_r = C_o n^2 , \qquad (4.41)$$

$$V_i = \frac{V_g}{n} . \qquad (4.42)$$

The first items to mention that change from the transformations are the basic characteristics: the characteristic impedance, the angular resonant frequency, and the conversion ratio. The new representations of these characteristics are:

$$Z_o = \frac{1}{n^2} \sqrt{\frac{L_o}{C_o}} , \qquad (4.43)$$

$$\omega_o = \frac{1}{\sqrt{L_o C_o}} , \qquad (4.44)$$

and

$$M = n \frac{V_o}{V_g} \quad , \tag{4.45}$$

respectively.

Although (4.39) is also the correct *form* to describe the input current of the flyback converter, the variables change with the transformations. It is also important to note that the input current of the flyback converter is scaled down by n from (4.39). Therefore, the complete expression for the input current of the flyback ZVS-QRC is:

$$I'_{in}(t) = \frac{1}{n} \cdot \begin{cases} I_x & T_0 < t < T_1 \\ I_x \cos \omega_o (t - T_{01}) & T_1 < t < T_2 \\ v + y(t - T_{01} - T_{12}) & T_2 < t < T_3 \\ I_x & T_3 < t < T_4 \end{cases} \tag{4.46}$$

where the following definitions now apply:

$$I_x = \frac{M}{Q} \frac{V_g}{n} \frac{(1 + M)}{Z_o} \quad , \tag{4.47}$$

$$v = I_x \cos(\alpha) \quad , \tag{4.48}$$

$$y = \frac{V_g}{n} \frac{(1 + M)}{Z_o} \omega_o \quad , \tag{4.49}$$

$$T_{01} = \frac{1}{\omega_o} \frac{Q}{M} \quad , \tag{4.50}$$

$$T_{12} = \frac{\alpha}{\omega_o} \quad , \tag{4.51}$$

$$T_{23} = \frac{1}{\omega_o} \frac{M}{Q} (1 - \cos \alpha) \quad . \tag{4.52}$$

The following definitions have not changed:

$$\alpha = \sin^{-1}\left(-\frac{Q}{M}\right) , \tag{4.53}$$

$$T_{34} = T_s - T_{01} - T_{12} - T_{23} . \tag{4.54}$$

These equations (along with Z_o, ω_o, M) are now all a function of the flyback converter parameters: V_g, L_o, C_o, n ; thus (4.46) fully describes the input current of the flyback ZVS-QRC.
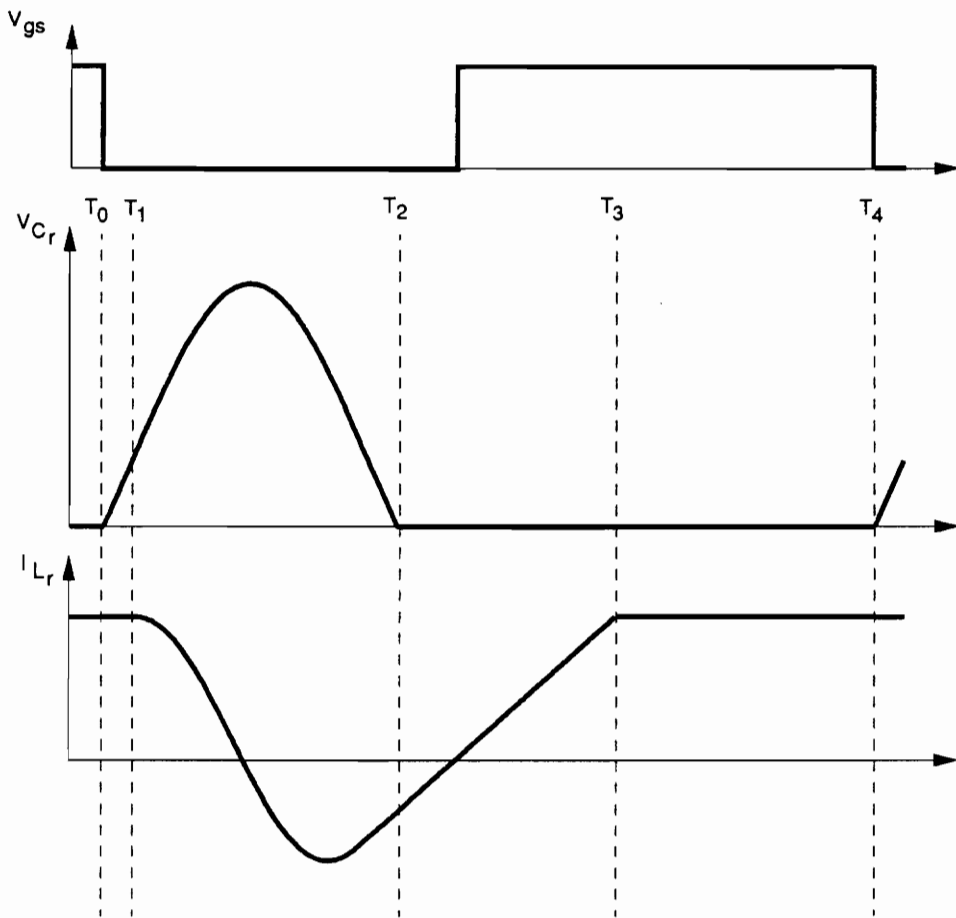
Figure 4.4.   Theoretical waveforms of equivalent flyback ZVS-QRC

4.5 General Solution of the Fourier Coefficients

Equation (4.46) represents the input current for the flyback converter. One way to find the Fourier coefficients is to apply the following equations [9]:

$$a_m = \frac{2}{T_s} \int f(t) \cos(x_m t) dt \quad m = 0, 1, 2, ... \tag{4.55}$$

$$b_m = \frac{2}{T_s} \int f(t) \sin(x_m t) dt \quad m = 0, 1, 2, ... \tag{4.56}$$

so that the function $f(t)$ can be written as a collection of sine and cosine terms of the form:

$$f(t) = \sum_{m=0}^{\infty} (a_m \cos x_m t + b_m \sin x_m t) , \tag{4.57}$$

where

$$x_m = 2m\pi f_s . \tag{4.58}$$

The magnitude of the mth Fourier coefficient can be written as:

$$c_m = \sqrt{a_m^2 + b_m^2} \quad m = 0, 1, 2, ... \tag{4.59}$$

Using $f(t) = I'_{in}(t)$ where $I'_{in}(t)$ is represented in (4.46) will yield the proper analytical result. The integration and simplification processes, however, are very tedious and enduring. Shifting the axes will help to simplify matters somewhat.

Shifting the vertical axis will only cause a change in the DC term ($m = 0$) of the Fourier series. Since only the AC terms ($m \geq 1$) are of interest, a vertical shift can be used to simplify the in-

tegrations. A logical vertical shift would be to shift the axis so that I_x is now at the zero level. This effect is shown in Fig. 4.5(a).

A time shift will also help to simplify the integration by shifting the time axis to the right so that time T_1 now represents $t = 0$. We can take advantage of the time zero when it comes to evaluating the integrals. In calculating the Fourier coefficients, a time shift is legal as long as the integration still encompasses one period. The effect of the time shift on the input current waveform is shown in Fig. 4.5(b).

The final form of the expression for the input current of the flyback ZVS-QRC, including both the time shift and the amplitude shift, is shown in (4.60):

$$ I'_{in}(t) = \frac{1}{n} \cdot \begin{cases} 0 & T_{01} < t < 0 \\ -I_x + I_x \cos \omega_o t & 0 < t < T_{12} \\ I_x(\cos \alpha - 1) + y(t - T_{12}) & T_{12} < t < T_{12} + T_{23} \\ 0 & T_{12} + T_{23} < t < T_s + T_{01} \end{cases} \tag{4.60} $$

Note that shifting the horizontal (time) axis essentially causes time zero and time T_1 to switch, so that:

$$ T_{01} < 0 \ , \tag{4.61} $$

$$ T_{01} = -\frac{1}{\omega_o} \frac{Q}{M} \ . \tag{4.62} $$

The integration is performed in Appendix C. The final solution of the Fourier coefficients is shown below. The cosine terms have values of:

$$ a_m = \frac{I_x}{n} a_m' \ , \tag{4.63} $$

where

$$m\pi a_m' = -\sin x_m T_{12}$$
$$+ \frac{1}{d_m}\left[\frac{\omega_o}{x_m}\sin \omega_o T_{12}\cos x_m T_{12} - \cos \omega_o T_{12}\sin x_m T_{12}\right]$$
$$+ (\cos \alpha - 1)(\sin x_m T_A - \sin x_m T_{12})$$
$$+ \frac{Q}{M}\omega_o T_{23}\sin x_m T_A + \frac{Q}{M}\frac{\omega_o}{x_m}(\cos x_m T_A - \cos x_m T_{12}) \qquad (4.64)$$

The sine terms have values of:

$$b_m = \frac{I_x}{n}b_m' \quad , \qquad (4.65)$$

where

$$m\pi b_m' = (\cos x_m T_{12} - 1)$$
$$+ \frac{1}{d_m}\left(\cos \omega_o T_{12}\cos x_m T_{12} + \frac{\omega_o}{x_m}\sin \omega_o T_{12}\sin x_m T_{12} - 1\right)$$
$$- \frac{Q}{M}\omega_o T_{23}\cos x_m T_A \qquad (4.66)$$
$$- (\cos \alpha - 1)(\cos x_m T_A - \cos x_m T_{12})$$
$$+ \frac{Q}{M}\frac{\omega_o}{x_m}(\sin x_m T_A - \sin x_m T_{12})$$

Also, the following equations apply:

$$T_A = T_{12} + T_{23} \quad , \qquad (4.67)$$

$$d_m = \left(\frac{\omega_o^2}{x_m^2} - 1\right) \quad . \qquad (4.68)$$

Therefore, the magnitude of the Fourier coefficients is:

$$c_m = \sqrt{a_m^2 + b_m^2} \quad . \qquad (4.69)$$

These results are the complete general form for the Fourier coefficients of the input current for the flyback ZVS-QRC shown in Fig. 4.1.
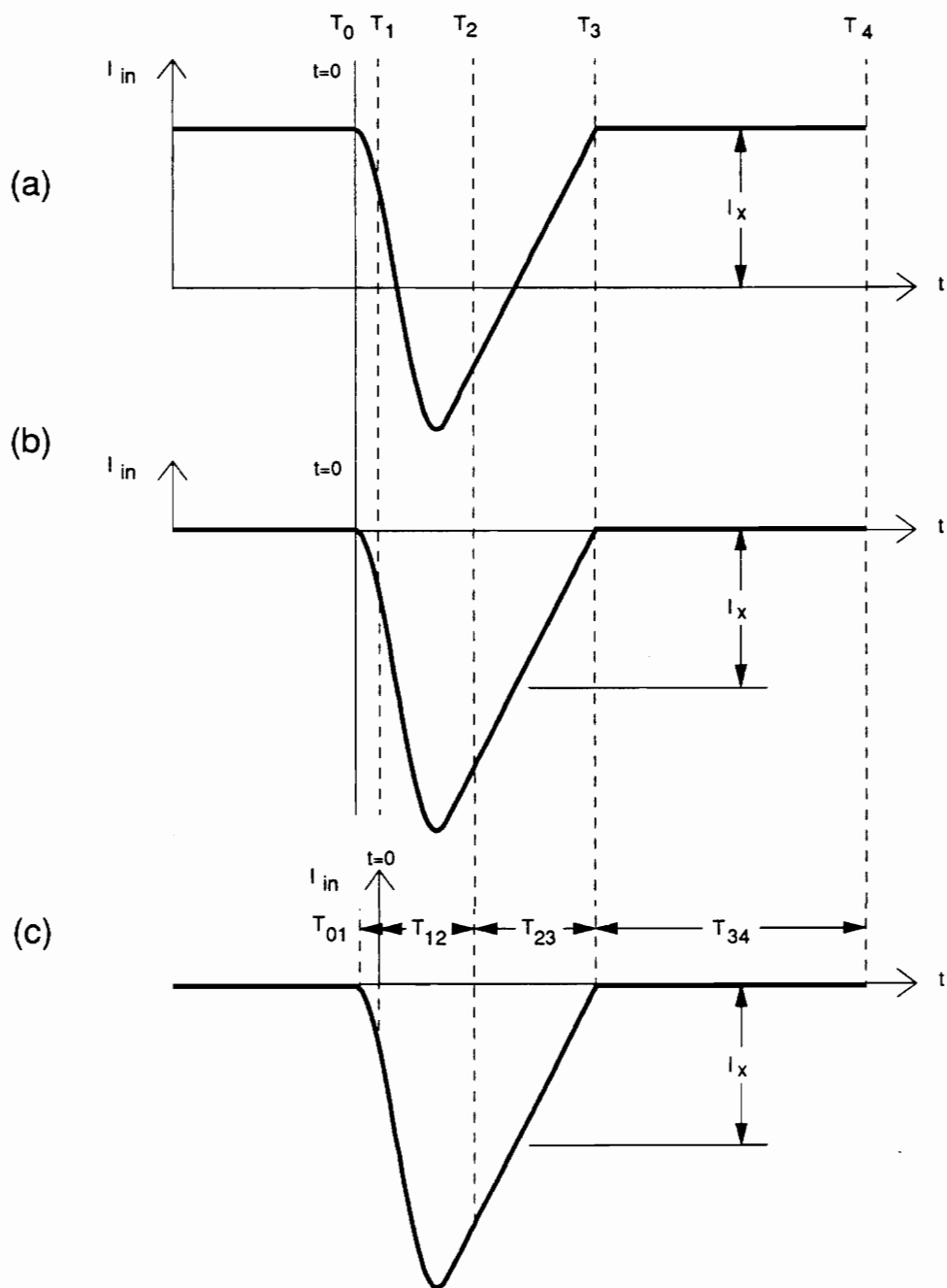
Figure 4.5. Shifted waveforms used in the spectrum calculations

4.6   Experimental Results

The purpose of this section is to test the analytical results of the previous sections against experimental results. In the previous sections, a complete analytical expression for the input current spectrum of the flyback ZVS-QRC is presented.

The flyback ZVS-QRC converter shown in Fig. 4.6 was constructed and tested. The experimental waveforms are shown in Fig. 4.7. A current probe was placed so that the input current waveform could be displayed on the oscilloscope. This waveform signal was then put into the spectrum analyzer. The magnitudes of the input current spectrum were then recorded from the spectrum analyzer and are shown in Table 4.1.

The parameters (f_o, f_s, T_{01}, etc.) used to calculate the theoretical spectrum were obtained directly from oscillograms. These values were then used to calculate the input current spectrum. Only the first twenty harmonics are shown in Table 4.1.

An overplot of the two sets of data is shown in Fig. 4.8. Notice that the two sets correspond to each other well at lower harmonics, but because of parasitic oscillation, they differ at higher harmonics.

Examining the oscillogram shown in Fig. 4.7 closely shows that the input current has an oscillation imposed on it. The frequency of this oscillation is approximately 11.5 MHz.

Transforming the high-frequency sine wave in the time domain to the frequency domain yields a bell-shaped function centered about the frequency of the sine train; therefore, it would be expected that any difference between the experimental data and the theoretical data would be centered about harmonic number:

$$\frac{f(\text{high frequency sine wave})}{f(\text{switching})} = \frac{11.5 \text{ MHz}}{1.06 \text{ MHz}} = 11 \quad. \tag{4.70}$$

The effect of this high frequency sine wave should be seen around harmonic number 11 in any of the experimental data. Chapter 5 offers a more detailed explanation.

A plot of the theoretical data subtracted from the experimental data is shown in Fig. 4.9. It is evident that the only significant difference between the experimental data and the theoretical data does occur around the predicted harmonic number, number 11.

Also, there is a slight discrepancy at harmonics around harmonic 19. At these frequencies, the magnitude of that harmonic is already 60dB below (or 1000 times lower) the fundamental, so that the spectrum analyzer is measuring the effects of parasitics that are hard to see in the oscillogram.

Although not shown in this chapter (but shown in Chapter 5) the parasitic oscillations do show at harmonics of the ringing frequency (most visible at the second harmonic of the ringing frequency). This also can contribute to the discrepancy around harmonic 19.

Therefore, the analytical results derived here in Chapter 4 do provide an accurate description of the input current spectrum for the flyback ZVS-QRC.

Table 4.1. Experimental and theoretical ZVS-QRC spectral data

m	Theoretical (dB)	Experimental (dB)
1	9.6	9.7
2	4.6	5.4
3	-3.1	-1.9
4	-5.0	-4.9
5	-8.9	-7.8
6	-15.1	-15.9
7	-16.7	-16.0
8	-26.1	-21.8
9	-34.5	-26.3
10	-37.4	-21.2
11	-29.7	-15.1
12	-35.6	-20.8
13	-34.7	-31.1
14	-33.9	-33.0
15	-44.7	-46.4
16	-45.4	-37.3
17	-40.3	-40.4
18	-37.8	-45.1
19	-55.6	-43.7
20	-41.5	-41.8
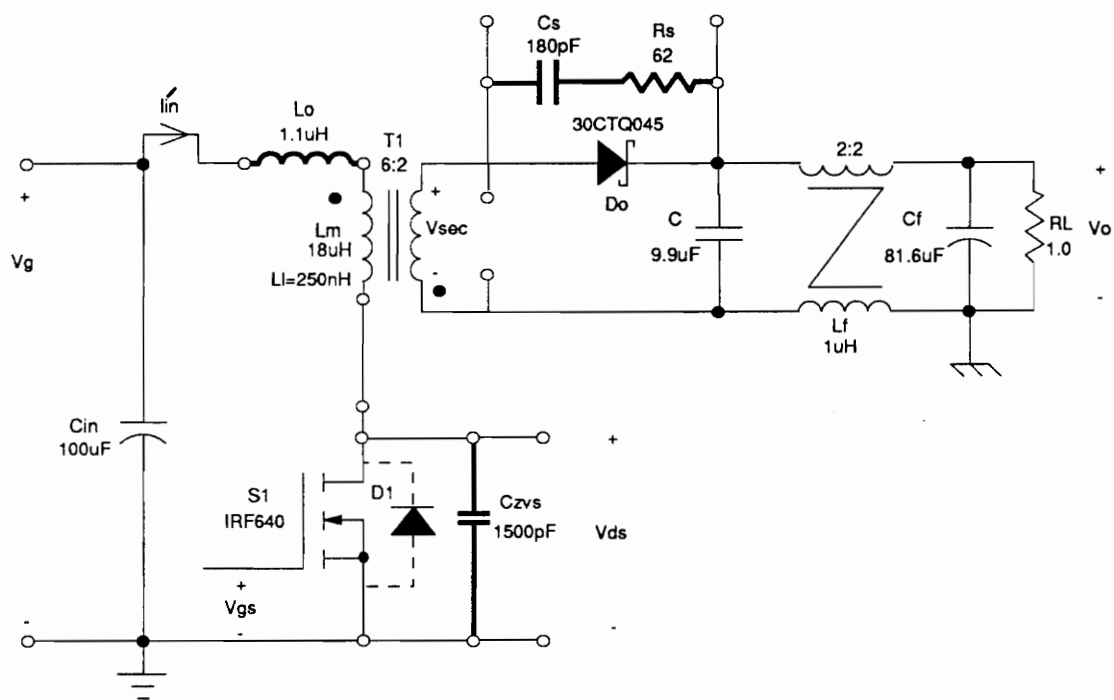
Figure 4.6. Schematic of the experimental flyback ZVS-QRC circuit

Tek

Top trace: V_{GS}
Middle trace: I'_{in}
Bottom trace: V_{DS}
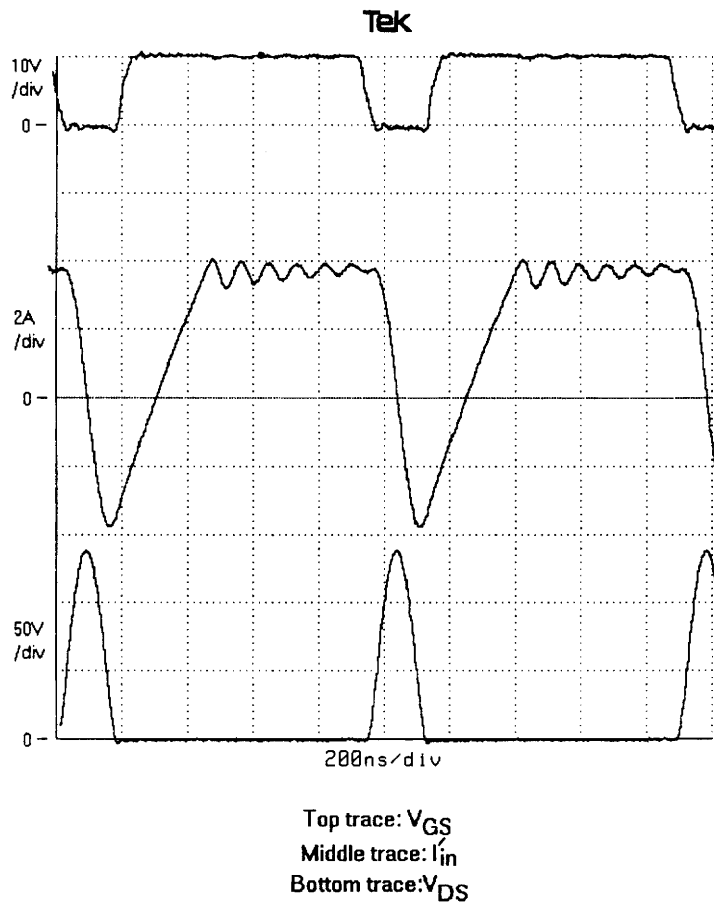
Figure 4.7. Waveforms of the experimental flyback ZVS-QRC waveforms

dB
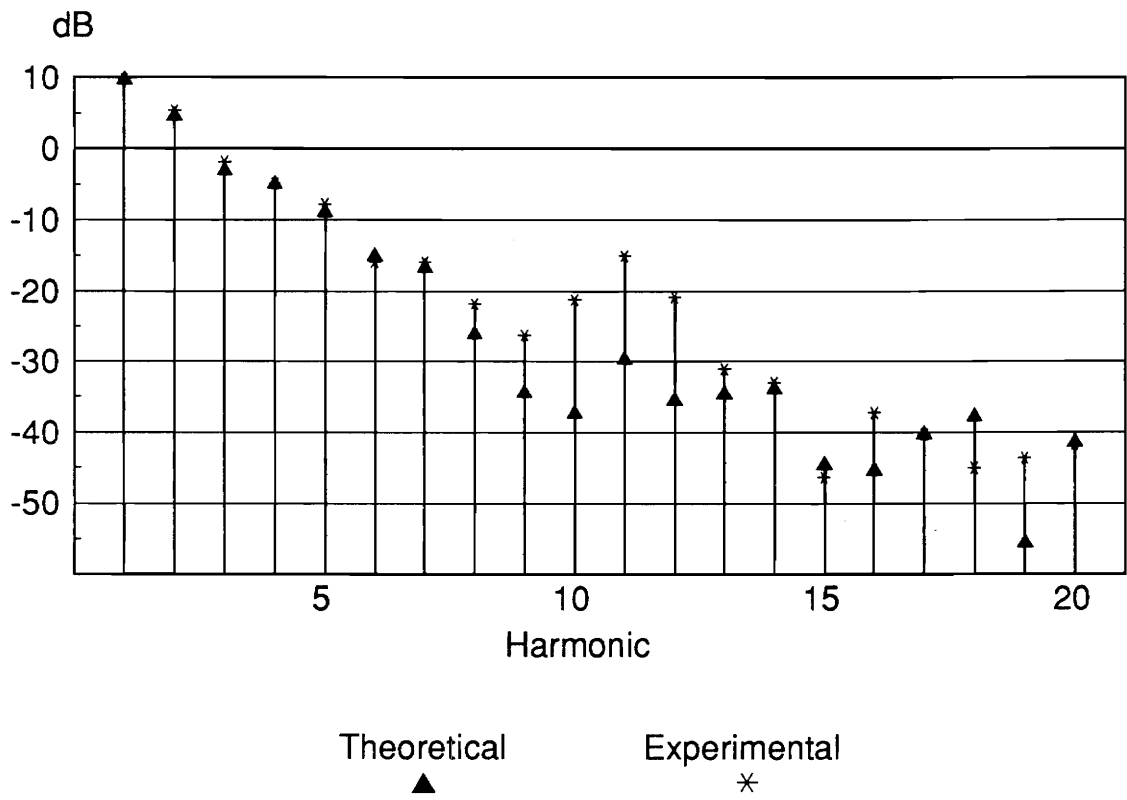
Figure 4.8.   Overplot of experimental and theoretical spectral components
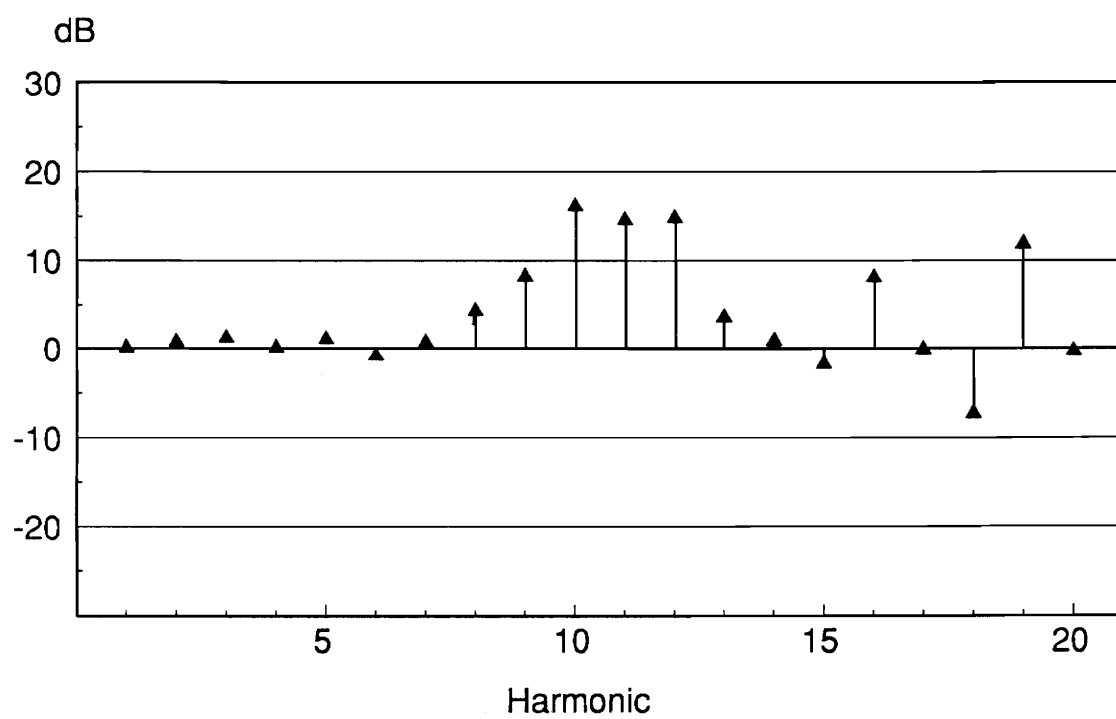
Figure 4.9. Theoretical spectral magnitudes subtracted from experimental spectral magnitudes

4.7 A Theoretical Example

To examine the change in the spectrum as a function of line and load conditions, a numerical example will be presented. For this example, assume the following operating conditions:

- $V_g = 21\ V$ to $32\ V$

- $V_{g,nominal} = 24\ V$

- $V_o = 5\ V$

- $I_o = 1\ A$ to $5\ A$

- $f_{s,max} = 1\ MHz$

- $n = 3\ turns$

The values of the resonant tank elements were calculated using the procedure described in [2]. The component values of the resonant tank are:

- $f_o = 1.47\ MHz$

- $Z_o = 10.7\ \Omega$

Also, assume that the converter operates in half-wave mode.

Six specific cases are of interest: low-line light-load, low-line full-load, nominal-line light-load, nominal-line full-load, high-line light-load, high-line full-load. The spectral data of these six cases were computed and graphed in Figs. 4.10 (a-f).
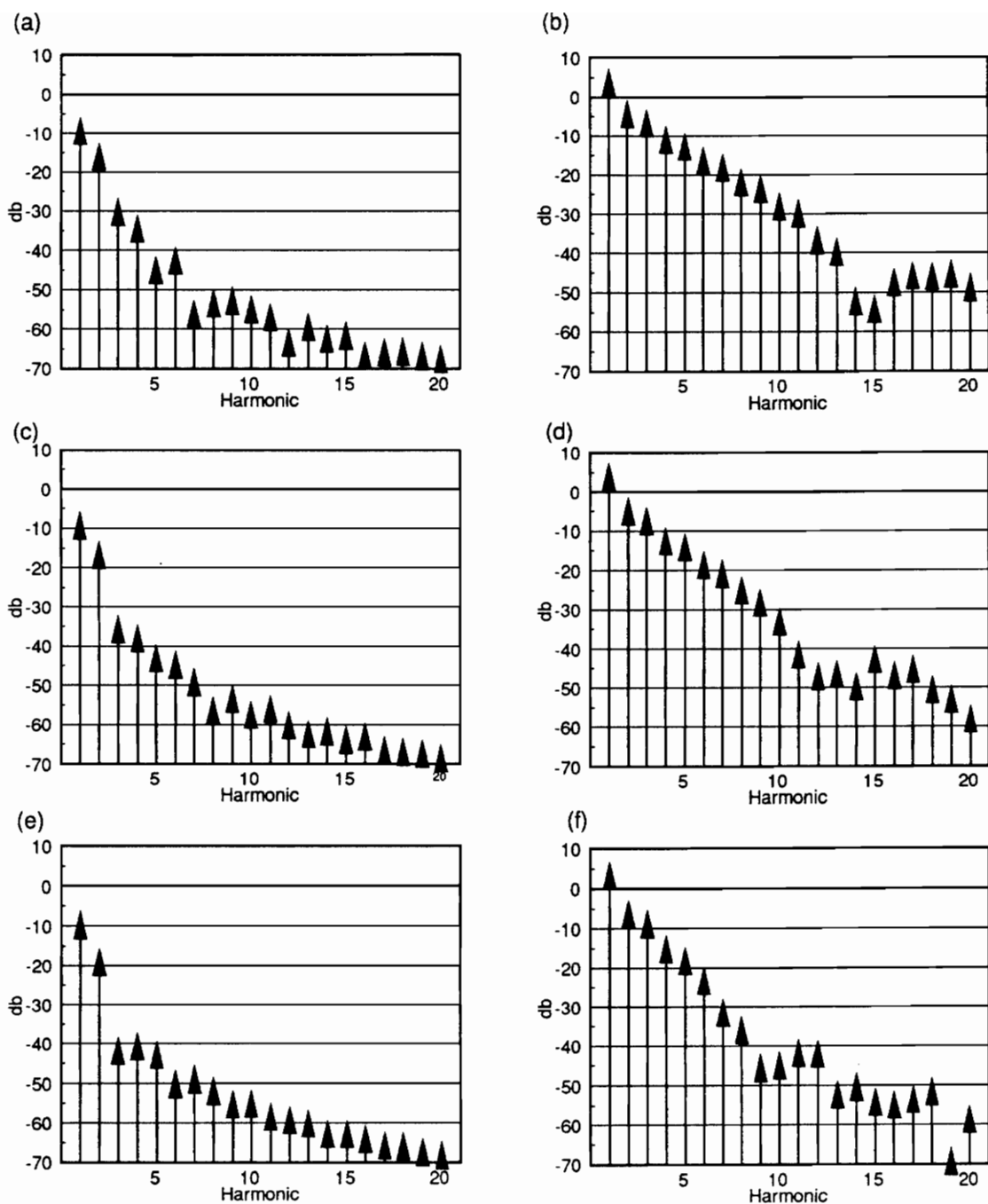
Figure 4.10. Spectrum for different cases of the flyback ZVS-QRC: (a) low-line and light-load, (b) low-line and full-load, (d) nominal-line and light-load, (e) nominal-line and full-load, (e) high-line and light-load, and (e) high-line and full-load

4.8 Comparisons

4.8.1 ZVS-QRC to PWM

Comparing the spectrum of the example for the ZVS-QRC to the spectrum of the same example for the PWM converter, several points need to be made. First, both sets of plots seem to be sensitive to load conditions. That is, for a given input voltage, a change in load will adversely effect the input current spectrum. One reason for this is that both sets of analytical equations are directly proportional to the inductor (hence, load) current.

Also, although the fundamental ($m = 1$) is greater in value in the ZVS-QRC case for all conditions, the magnitudes of the spectrum at higher harmonics decrease faster than for PWM. As an example of this steep slope, consider the full-load cases of both converters. For the ZVS-QRC, the spectrum has dropped off by at least 50 db by harmonic 11; while for the PWM converter, only a maximum of a 40 db drop is seen in the entire spectrum shown of twenty harmonics. This will help when building an input filter, because although the fundamental is stronger, it can be attenuated the proper amount, whereas the higher harmonics (higher frequencies) are not as easy to attenuate. In other words, it is much easier to build an input filter to attenuate the first few harmonics than to build a filter to attenuate a wide range of harmonics.

4.8.2 ZVS-QRC to ZCS-QRC

When the spectrum of the ZVS-QRC is compared to the spectrum of the ZCS-QRC, several points can be made. The first concerns how spread-out the spectrum of the ZCS-QRC is compared to the spectrum of the ZVS-QRC. It appears that for the ZVS-QRC spectrum, the attenuation of the envelope is relatively constant at all the line/load conditions; conversely, the attenuation of the envelope of the ZCS-QRC spectrum lowers as conditions change. In general, the slope of the ZCS-QRC spectrum envelope will widen as the operating frequency is decreased. The ZVS-QRC spectrum drops off 40 db in the first few harmonics for every condition shown, while the ZCS-QRC spectrum may not even drop off 40 db for the entire twenty harmonics shown.

Not only is the attenuation of the envelope important, but also the computed values. For most cases of the ZCS-QRC spectrum, the entire spectrum contains many harmonics of significant levels, but for all the cases of the ZVS-QRC, the significant values of the spectrum are all at very low harmonics.

The ZVS-QRC spectrum would be more desirable than the ZCS-QRC spectrum because in all cases only the lower harmonics would need significant attenuation, while in the ZCS-QRC, more harmonics would need attenuation.

4.9 Extension to Other Converters

Because of the way that the equations of the previous sections have been defined and derived, they can be extended to other families of converters such as the buck ZVS-QRC and the boost ZVS-QRC.

In [1] it is shown that the general shape of the input current for the buck ZVS-QRC and the boost ZVS-QRC are similar to the flyback ZVS-QRC presented in this chapter. In fact, only changes in the definitions of the variables of (4.63) to (4.66) are needed.

4.10 Summary

In this chapter, the flyback ZVS-QRC was considered. For this converter, the input current spectrum was derived in terms of circuit parameters. The final analytical equations were displayed so that the inductor current term can be considered a specific term, in contrast to the rest of the equation which can be considered a normalized term.

An experimental test circuit was constructed. The input current spectrum was determined by a spectrum analyzer. These experimental results were compared against results from the derived equations. The experimental results were shown to be accurate when the effect of the secondary side ringing was taken into account. The FFT results compared very well against the results acquired from the analytical equations.

Also, the same theoretical example used in the last two chapters was used in this chapter. Six plots for the same set of line/load conditions were shown, and a comparison to PWM and ZCS-QRC was made. It was determined that the spectral characteristics for the flyback ZVS-QRC were more sensitive to changes in load conditions (although there are some changes with a change in the line condition).

Chapter 5

Experimental Results and Comparisons

5.1 Measurement Procedure

To preform all of the experiments in this chapter, a printed circuit board with the ability to operate using either PWM, ZCS-QRC, ZVS-QRC, or ZVS-MRC was used. Figure 5.1 shows the schematic for the board. Not all of the parts were used for each experiment; for instance, the resonant components were absent during the PWM experiment. On the schematic, all of the components with open circles on either side represent components that are socketed into the board. Therefore, either the component could be used or it could be omitted. Each section in this chapter describes more on the specific circuit components used.

For all of the experiments, the unsocketed components were kept the same. These components are: C_{in}, T_1, D_o, R_L, and the output filter.

Each of the converters was designed to operate between an input line voltage of 15 V to 25 V and an output load current between 3 A and 5 A at an output voltage of 5 V. All of the waveforms in this chapter are with respect to a nominal operating condition of a 20 V input voltage and a 5 A output current.

All of the converters were run closed loop using the Signetics NE5580 control chip. The NE5580 has the ability to run either using a constant on-time control or a constant off-time control, depending on how the chip is set up. Figure 5.2 shows the schematic of the control circuitry.

The spectral measurements were made using the HP8568B spectrum analyzer. The current I'_{in} was sensed using a Pearson Model 411 current transformer terminated into the spectrum analyzer. The current transformer, when terminated into 50 Ω, has a sensitivity of 2A/100mV. This will need to be considered when converting the measured values from dBm to dB.

The spectrum analyzer provides reading in dBm. That is, all readings are referred to the power through the 50Ω input impedance referenced to 1mW. Therefore, if V_{RMS} is the RMS voltage across the input to the spectrum analyzer and dBm is the reading in dBm, then the following relationship holds:

$$dBm = 10 \log \left(\frac{V^2_{RMS}}{50\Omega \cdot 1mW} \right) , \qquad (5.1)$$

which reduces to:

$$dBm = 20 \log \left(\frac{V_{RMS}}{0.2236} \right) . \qquad (5.2)$$

Likewise, a reading in dBm can be converted to a reading in RMS voltage by:

$$V_{RMS} = 0.2236 \cdot 10^{dBm/20} . \qquad (5.3)$$

But this assumes that a voltage is of interest. Since the current is of interest in this particular case, the sensitivity factor of the Pearson current probe needs to be accounted for. Also, the relationship between RMS values and peak values needs to be considered. Since the spectrum of a waveform is the amplitudes of different frequency sine waves, the relationship between RMS values and peak values is simply: $RMS\sqrt{2} = peak$. Because peak values are easier to draw relationships to, all of the measurements will be referenced to the following standard: $1\,A_{peak} \rightarrow 0\,dB$. Therefore, considering the sensitivity factor and the RMS to peak relationship:

$$I_{peak} = \sqrt{2}\,\frac{2A}{0.1V}\,V_{RMS} \quad . \tag{5.4}$$

Substituting (5.3) into (5.4):

$$I_{peak} = 6.32 \cdot 10^{dBm/20} \quad . \tag{5.5}$$

Taking the logarithm and multiplying by 20 will given a reference of $1\,A \rightarrow 0\,dB$.

$$I_{dB} = 20\log 6.32 + dBm \quad , \tag{5.6}$$

$$I_{dB} = 16.0 + dBm \quad . \tag{5.7}$$

Therefore, to convert the measurements made by the spectrum analyzer from dBm to dB, a factor of 16.0 needs to be added to all dBm measurements. All of spectral plots in this chapter were scaled by this factor so that $1\,A \rightarrow 0\,dB$. With this standard, values of -20 dB, -40 dB, and -60 dB translate into current amplitudes of 0.1 A, 0.01 A, and 0.001 A, respectively.

The plots were recorded in two parts: from 100 kHz to 30 MHz and from 30 MHz to 60 MHz. Each plot was saved on a diskette and converted from the HPGL format to the TIFF format using the program HiJaak. The two pictures then could be imported into FreeLance and combined to form one picture.

In order for the spectrum analyzer to achieve an accurate reading, the resolution bandwidth (Res BW) must be set less than or equal to the frequency span of one screen (30 MHz) divided by the actual number of data points recorded by the spectrum analyzer (1000 points). To satisfy this condition, the resolution bandwidth was selected to be 30 kHz. Also, for accurate plots, the video bandwidth (VBW) was chosen to be 100 Hz and the sweep time (SWP) was chosen to be 30 seconds.

To improve the accuracy further, all of the oscilloscope probes were removed from the circuit when the spectrum analyzer was in use. This helps in eliminating any spurious ground noise that may be coupled to the spectrum analyzer. Also, to reduce ground noise further, the coaxial wire connecting the Pearson current probe to the spectrum analyzer was wound several times around a high-frequency high permeability ferrite core to create a common-mode choke.
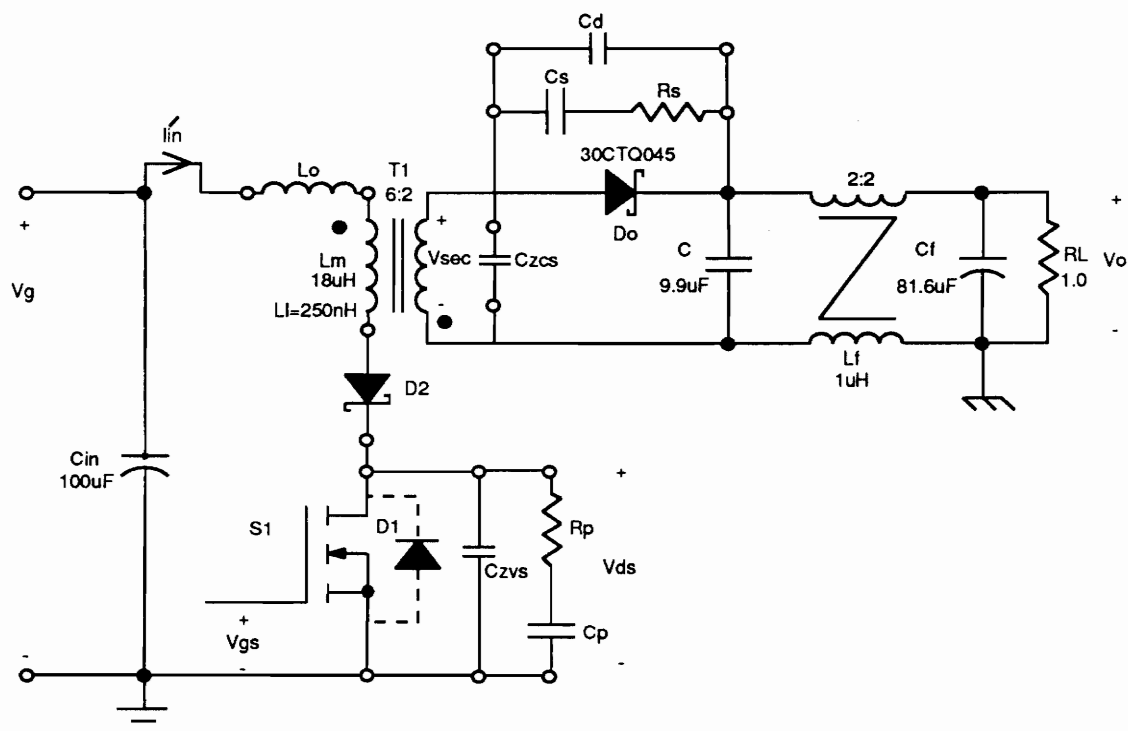
Figure 5.1. Schematic of the power stage showing all of the parts used for the different experiments
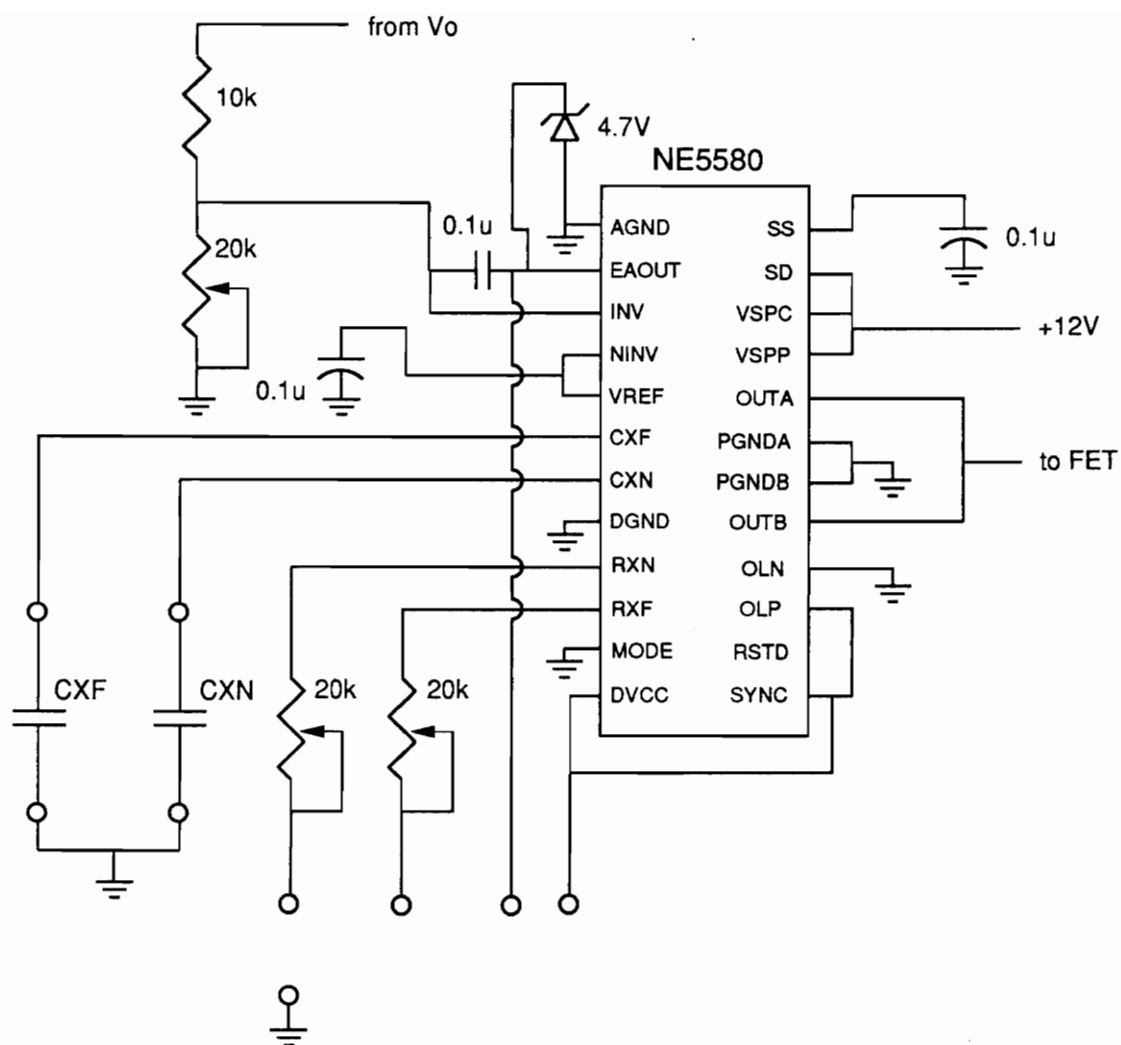
Figure 5.2. Schematic of the control circuit

5.2 Experimental Results

A detailed description of the design procedure used for each of the converters can be found in [14]. The PWM and ZCS-QRC experiments were run using a constant on-time control scheme, and the ZVS-QRC and ZVS-MRC experiments were run using a constant off-time control. Figure 5.3(a) shows how to connect the chip for constant on-time operation, and Fig. 5.3(b) shows how to connect the chip for constant off-time operation.
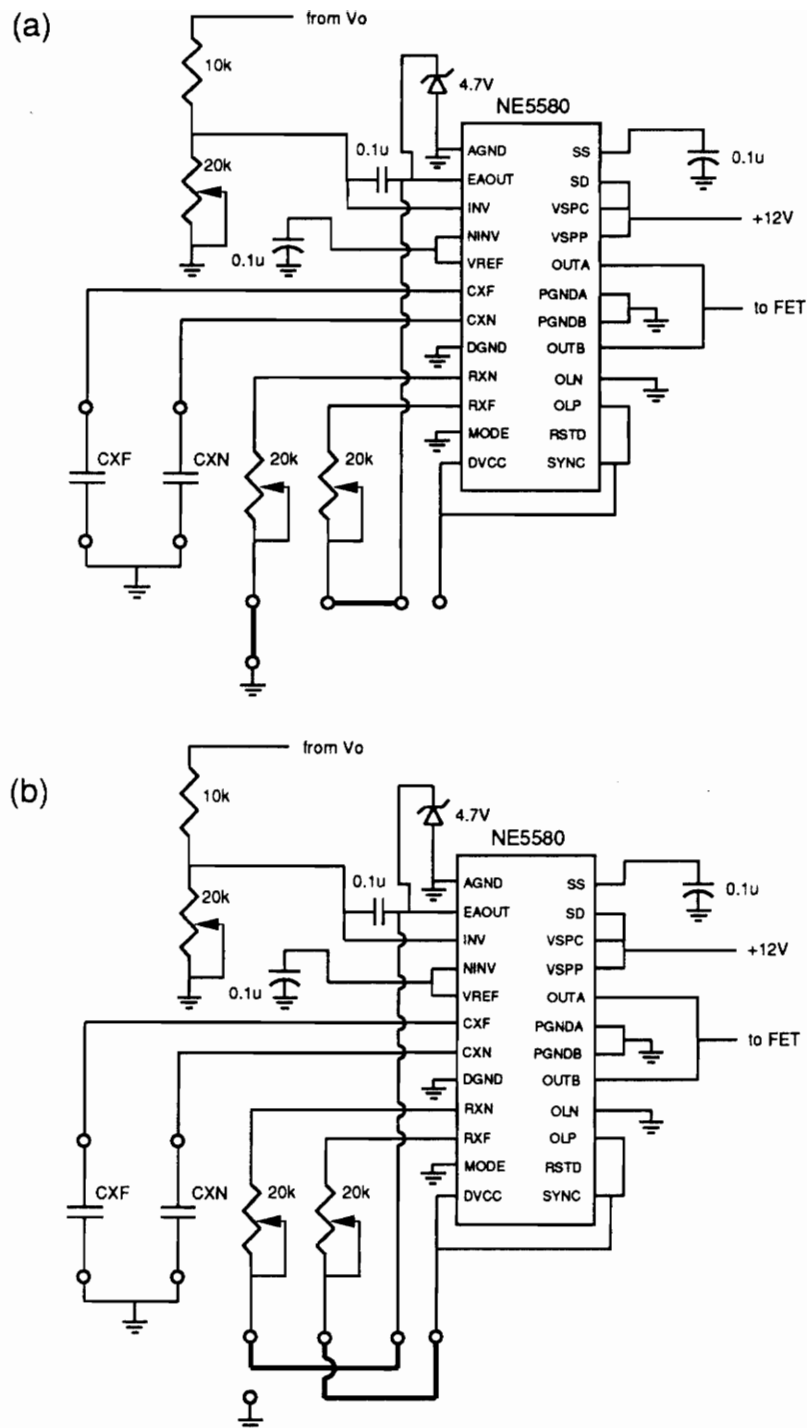
Figure 5.3. Control circuit for the different converters: (a) Constant on-time control, and for (b) constant off-time control

5.2.1 PWM

5.2.1.1 Discussion of Ideal PWM Input Current Spectrum

For a flyback PWM converter, an ideal input current waveform is composed of two parts: a square wave and a triangular ramp. The spectrum of the entire ideal waveform can be found by adding together each of the two sets of frequency spectrum.

For an example, consider the square wave shown in Fig. 5.4(a). This waveform is similar to an ideal PWM input current waveform with zero ripple current ($\xi = 0$). To examine the changes in the spectrum for the following five different duty cycles ($D = T_{on} / T_s$): D = 0.45, 0.47, 0.50, 0.52, 0.55. The first 100 harmonics were evaluated using (2.25) with $\xi = 0$, and are plotted for each of the square waves. Figures 5.4 and 5.5 show the calculated spectrum for a 200 kHz square wave with a duty cycle of 0.45, 0.47, 0.50, 0.52, and 0.55. (For this discussion, only the general shape is of interest, so the magnitudes were omitted.)

Figure 5.4 (b) shows the spectrum for the square wave of Fig. 5.4 (a) with a duty cycle of 0.45. The spectrum can be seen as being comprised of two sets of sinc functions: one made up of the odd number harmonics and one made up of the even number harmonics. Considering only the odd harmonics, the first valley occurs at 2 MHz. Considering only the even harmonics, the first valley occurs at 4 MHz.

Figure 5.4 (c) shows the spectrum of a square wave with a duty cycle of 0.47. In this spectrum, the odd harmonics have their first valley at 3.4 MHz, and the even harmonics have their first valley at 6.8 MHz. Notice that both of the first valleys have increased in frequency. In fact,

as D approaches 0.5, the first valleys of both the even and the odd sets of harmonics move toward infinity.

Also, note the trend of the amplitude of the even harmonics. As D approaches 0.5, the magnitude of the first even harmonic (and therefore subsequent even harmonics) decreases until D = 0.5. When D = 0.5, Fig. 5.5 (a), it can be seen that the magnitudes of all of the even harmonics have decreased to zero and that there are no valleys in the total spectrum shown.

As the duty cycle increases past 0.5, the reverse effects occur. As D increases, the valleys (and peaks) move from infinity toward the origin, and the magnitude of the first even harmonics increases. For an example, consider Fig. 5.5 (b) which shows the spectrum of the square wave with a duty cycle of 0.52. The first valley of the odd harmonics occurs at 3.0 MHz, and the first valley of the even harmonics occurs at 5.0 MHz. When the duty cycle is further increased to 0.55, shown in Fig. 5.5 (c), the first valley of the odd harmonics is now at 1.8 MHz, and the first valley of the even harmonics is now at 4.0 MHz. Also, notice that the magnitude of the first even harmonic is higher for the case of D = 0.55 than for the case of D = 0.52.

Now consider the second component of the ideal PWM input current waveform: the triangular ramp. Figure 5.6 (a) shows the triangular ramp and Fig. 5.6 (b) shows its spectrum. This shape of the spectrum will stay very much the same for different ramps. The amplitude of the spectrum will change with a change in amplitude of the ramp. Again, since only the general shape of the spectrum is of interest, the magnitudes have been omitted.

Also, ringing is sometimes present in PWM converters that operate without snubbers. This ringing takes the form of a pulsed exponentially damped sine wave. Figure 5.7 (a) shows this waveform and Fig. 5.7 (b) shows its associated spectrum. If another waveform has this exponentially damped sine wave imposed on it, the spectrum of that waveform will have the spectrum of the exponentially damped sine wave added to it. In the frequency domain, the effect will be seen at the frequency of the sine wave.

This is a brief background of some of the waveforms that will be considered in this section. In general, by adding together in the frequency domain the different components of a waveform, its complete spectrum can be obtained. For example, a square wave, similar in shape to Fig. 5.4 (a), with an exponentially damped sine wave imposed on the part of the waveform greater than zero, will have have a spectral envelope similar to the one of a square wave, except that a bell-shaped disturbance will be seen on the spectrum around harmonics of the sine wave's frequency.
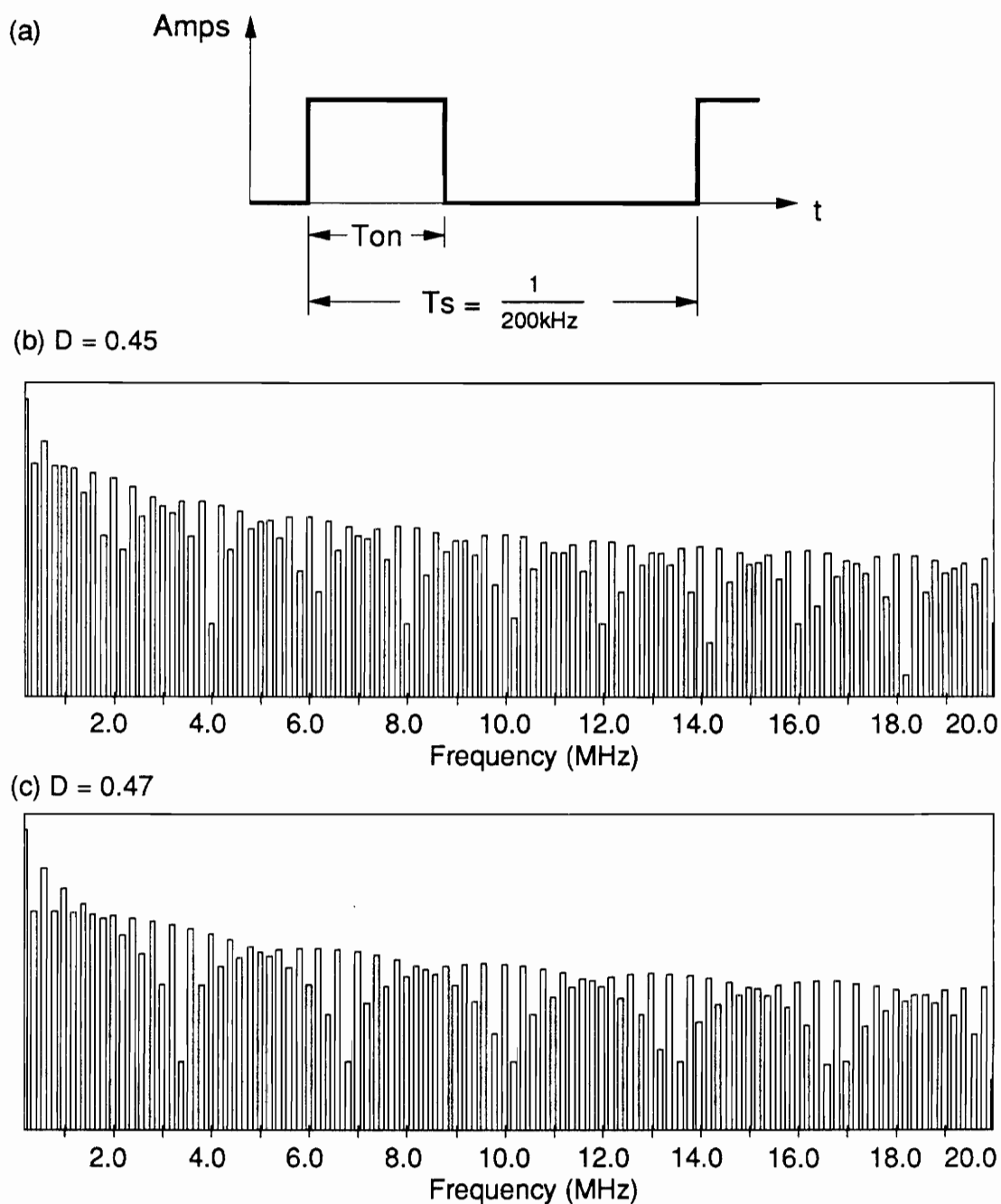
Figure 5.4. Generalized square wave and its associated spectrum: (a) Plot of a generalized square wave, (b) spectrum for duty cycle of 0.45, and (c) spectrum for a duty cycle of 0.47

(d) D = 0.5
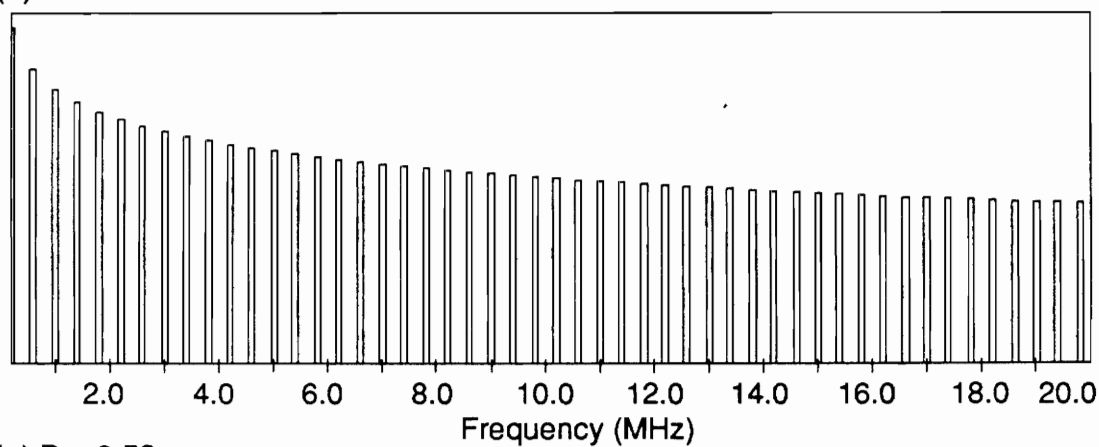
(e) D = 0.52
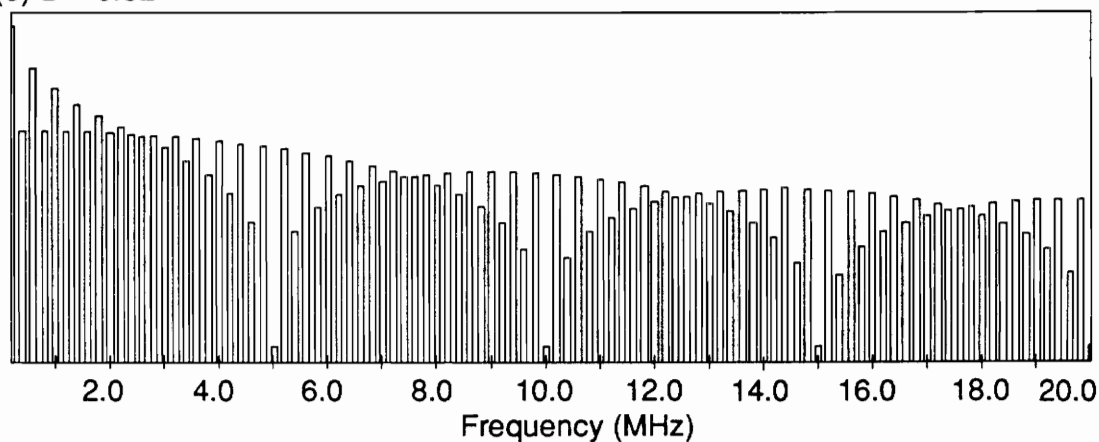
(f) D = 0.55
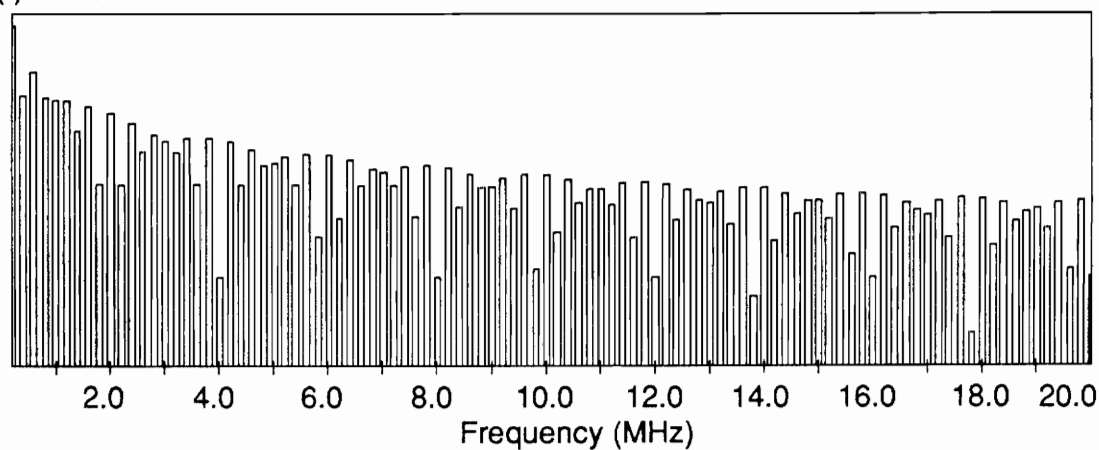
Figure 5.5.   More spectral plots of the generalized square wave: for a duty cycle of (a) 0.50, (b) 0.52, and (c) 0.55

$$Ts = \frac{1}{200kHz}$$

(b)

Frequency (MHz)
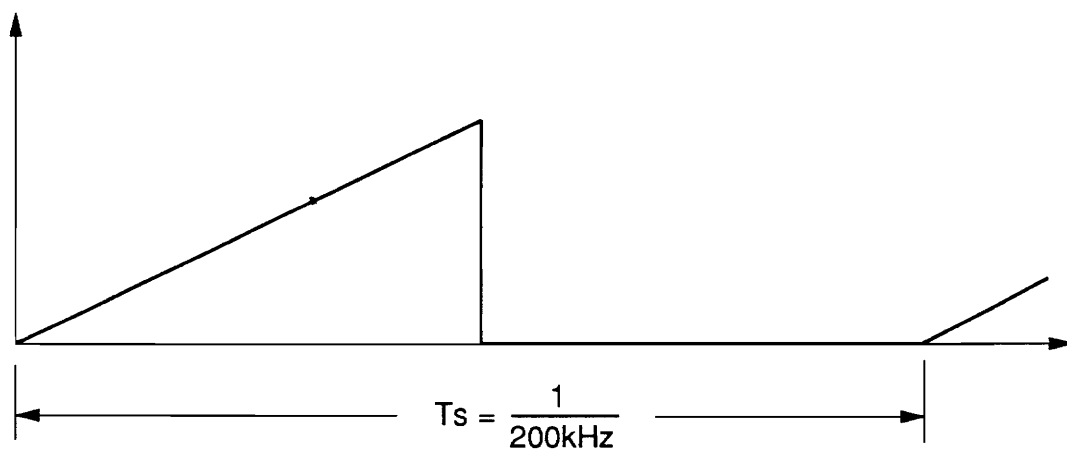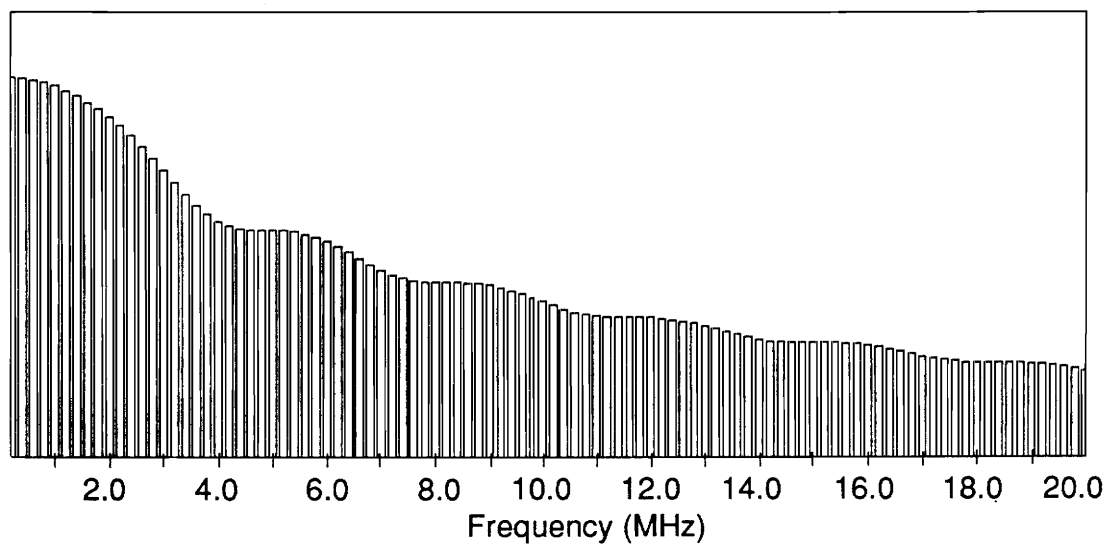
Figure 5.6. Generalized triangular ramp: (a) time domain plot, and (b) its associated spectrum
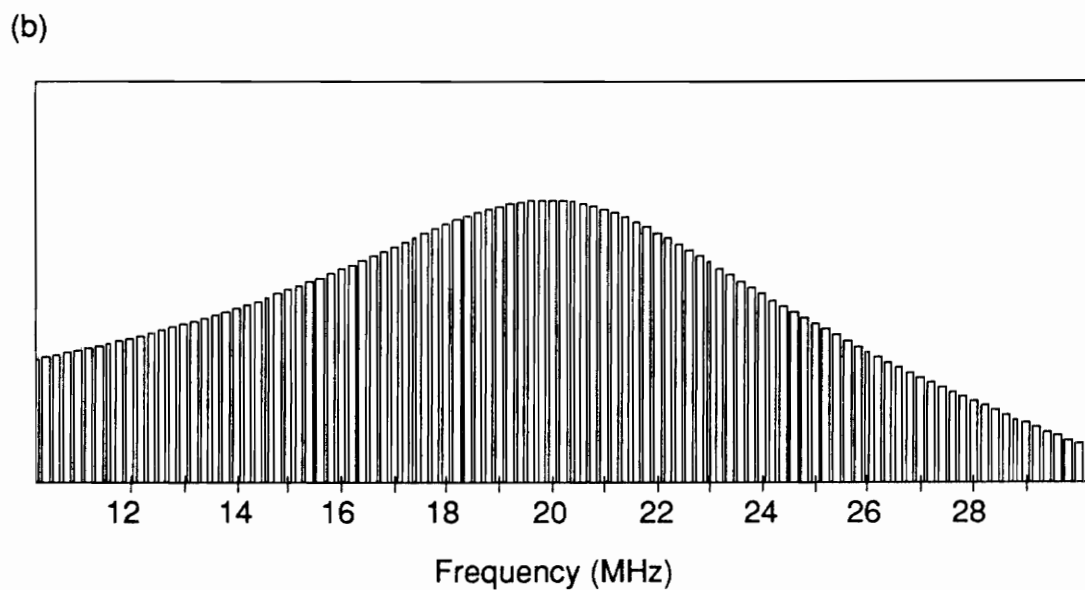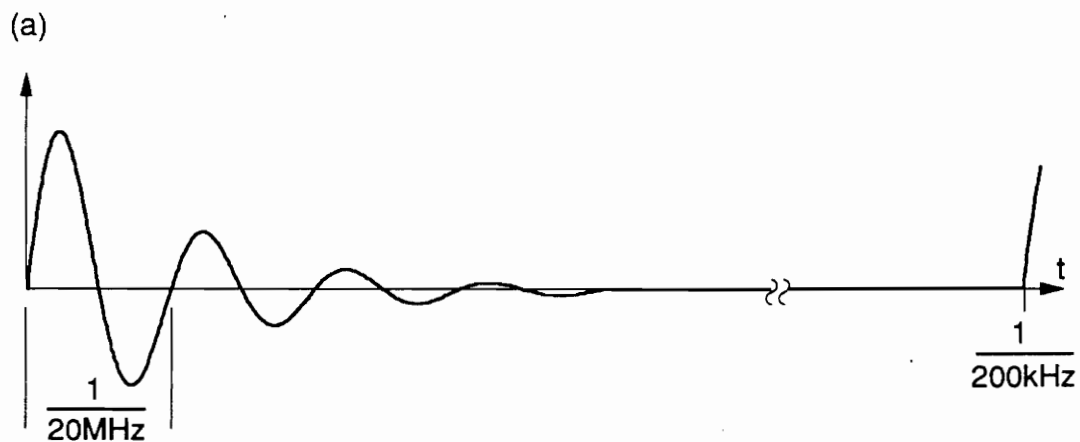
Figure 5.7. Generalized exponentially damped sine wave: (a) time domain plot, and (b) its associated spectrum

5.2.1.2 Experimental Testing

Figure 5.8 shows the schematic of the PWM circuit used. Since the leakage of the transformer has been minimized for operation at a frequency of 200 kHz, the frequency of operation at the nominal line/load conditions was chosen to be 200 kHz. Two sets of PWM experiments were run: one with the snubbers in place and one with the snubbers omitted. The results for each test will be presented and discussed.

Two snubbers were designed using the procedure in [14]. Their values are on the schematic in Fig. 5.8. One snubber is in parallel with the FET (to dampen the turn-off ringing of the FET), and the other is in parallel with the output diode (to dampen the turn-off ringing of the diode).

Figure 5.9 shows the waveforms of the PWM converter operating at the nominal line/load conditions. The input current waveform is the second from the top.

The spectrum of the PWM input current waveform for the snubbered converter is shown in Fig. 5.10. Considering the discussion presented in section 5.2.1.1, the experimental spectrum is similar to what would be expected. The peaks and valleys are accounted for by the square wave part of the input current, while the vertical offset at lower frequencies is accounted for by the triangular part of the input current.

Also, there are two spikes seen in the input current waveform. The spike on the leading edge of the input current waveform is caused by the turn-off of the output diode, while the spike on the trailing edge of the input current waveform is caused by turn-off of the FET. Because the amplitudes and the durations of these two spikes are very small when compared to the entire waveform, they have very little effect on the spectrum.

Figure 5.11 shows the waveforms of the PWM converter with the snubbers omitted. On the input current waveform, there are two distinctly different ringing frequencies. A ringing fre-

quency of approximately 10 MHz is seen when the FET is turned off (this ringing is from the leakage inductance of the primary side resonating with the drain to source capacitance of the FET), and a ringing frequency of approximately 20 MHZ is seen when the output diode is reverse biased (this ringing is from the leakage inductance of the secondary side resonating with the junction capacitance of the output diode). Since these two sets of oscillations comprise a relatively large part of the entire waveform, there should be a strong effect on the spectrum.

Figure 5.12 shows the spectrum of the input current waveform for the snubberless PWM converter operating at the nominal line/load conditions. It appears to be much different than the spectrum of the snubbered PWM converter (Fig. 5.10). Considering the discussion in section 5.2.1.1 of the exponentially damped sine wave, the difference can be explained. Since the ringing frequencies are approximately 10 MHZ and 20 MHz, a distortion similar to Fig. 5.7 (b) occurs at harmonics of these two ringing frequencies. Three places on the spectral plot are peculiar: around 10 MHz, around 20 MHz, and around 30 MHz. The first disturbance (at approximately 10 MHz) is caused by the ringing on the FET at turn-off. The second disturbance (at 20 MHz) has two components: the ringing caused by the output diode turn-off, and the second harmonic of the ringing caused by the FET turn-off. Finally, the third disturbance (at 40 MHz) is caused by the second harmonic of the ringing on the output diode.
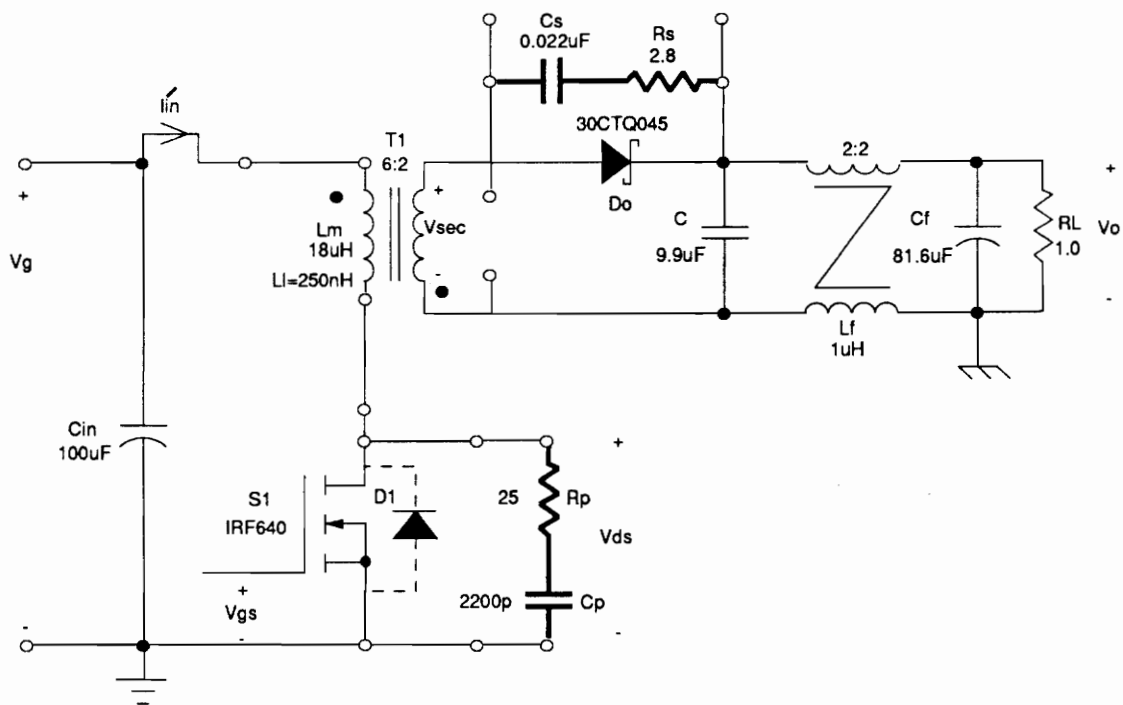
Figure 5.8.   Schematic of the entire PWM test circuit used

Figure 5.9. **Waveforms of the snubbered PWM circuit:** converter operating at the nominal line/load conditions

Figure 5.10. Input current spectrum of the snubbered PWM circuit

Figure 5.11. Waveforms of the snubberless PWM circuit: converter operating at the nominal line/load conditions

dB

RES BW 30 kHz
VBW 100 Hz   F (MHz)
SWP 30 sec   (Fs = 0.2 MHz)
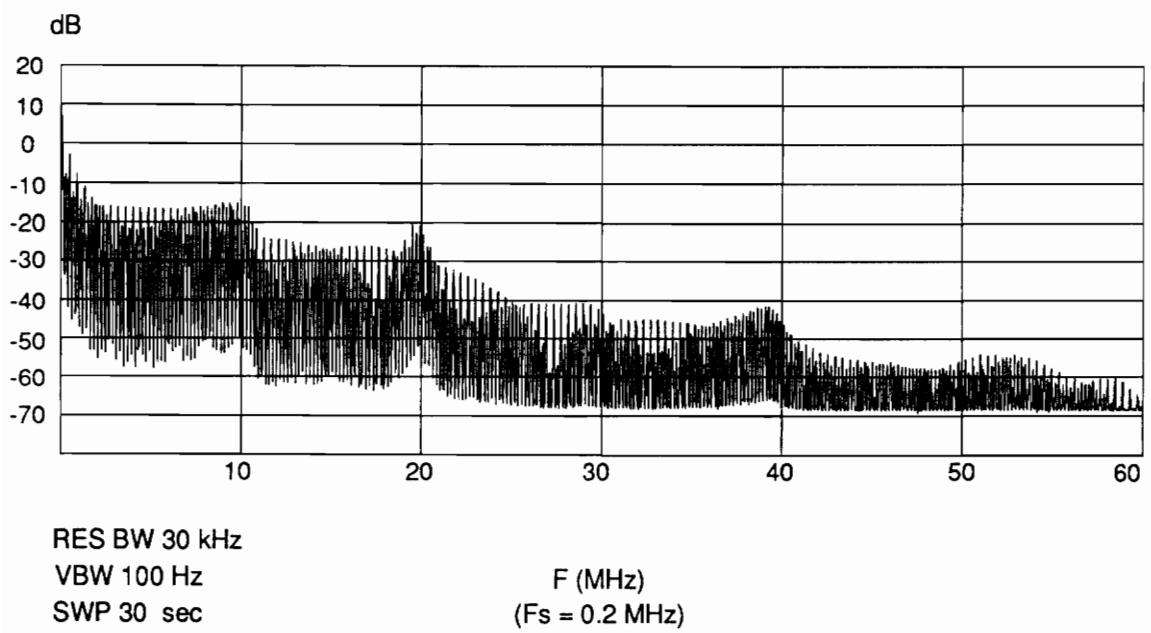
Figure 5.12.   Input current spectrum of the snubberless PWM circuit

5.2.2 ZCS-QRC

A schematic of the ZCS-QRC circuit that was used is shown in Fig. 5.13. It was designed as described in [14] for a maximum switching frequency of 1 MHz. At the nominal line/load operating condition, the switching frequency was 922 kHz.

Figure 5.14 shows the waveforms of the ZCS-QRC converter when operated at the nominal line/load conditions. Figure 5.15 shows the spectrum of the input current. At the lower frequencies, the spectrum looks similar to what would be expected for an ideal input current waveform (based on examples presented in Chapter 2). However, at the higher frequencies, the spectrum does not decrease to zero very fast; in fact, the values of the higher frequency harmonics are relatively constant. The spread out spectrum is a characteristic of wide band frequency modulation [15-18].

Figure 5.16 shows a close-up of the waveforms. In this figure, two definite changes in the FET off-time ringing on the input current waveform can be seen. One change is that the ringing seems to be damped in an exponential fashion. The second change in the ringing can be attributed to the fact that as the drain to source capacitance of the FET is being charged up (toward twice the input voltage), the actual value of this capacitance is changing. Since this drain to source capacitance forms a resonant circuit with parasitic inductances, then as the capacitance changes, the ringing frequency also changes.

Also, there is another oscillation on the input current to consider. Examining Fig. 5.16 a high-frequency oscillation on the input current during the on-time of the FET can be seen. At the end of the linear charging stage (Chapter 2), the output diode is reverse biased and begins to block the secondary voltage. The junction capacitance of the output diode sets up a resonant circuit with the parasitic inductances of the secondary side, causing this high frequency oscillation; however, as the voltage on the diode continues to change, so does its junction

capacitance and so does the frequency of oscillation. This oscillation is reflected back to the primary side and affects the input current.

Considering these two sets of changing frequencies, it is important to investigate frequency modulation a bit further. To show how modulation can effect the frequency spectrum of a waveform, an example will be presented. It is known that a single frequency sine wave is represented in the frequency domain by a single harmonic at the sine wave's frequency. If this sine wave were now frequency modulated and exponentially damped, how would the spectrum change? Consider the following equation that represents a frequency modulated signal with an exponential decay:

$$f(t) = -e^{\left(-5 \cdot 10^6 t\right)} \cdot \sin\left[2\pi \cdot 0.5 \cdot 10^7 t + \frac{5 \cdot 10^{13} t^2}{2}\right] . \tag{5.8}$$

Figure 5.17 (a) shows a plot of this equation in the time domain, while Fig. 5.17 (b) shows the spectrum of this signal. Since only the shape is of interest, the magnitudes on each plot have been omitted. Looking at the shape of the envelope, it is apparent that the spectrum of the frequency modulated exponentially damped sine wave is spread out over a large frequency range (the frequency range of modulation) [15].

The ringing frequency during the FET off-time ranges from approximately 9 MHz to approximately 16MHz; the oscillation during the on-time, however, is of a much higher frequency range-- from approximately 32 MHz to 45 MHz. Since both sets of oscillations are damped, the example illustrated above of the exponentially damped-frequency modulated sine wave is applicable. Considering the two sets of ringing frequencies, it would be expected (and is shown in Fig. 5.15) that the experimental spectrum would extend to approximately 45 MHz and then fall off rapidly. Also, it would be expected that the magnitudes of the harmonics between 9 MHz and 16 MHz also be raised.

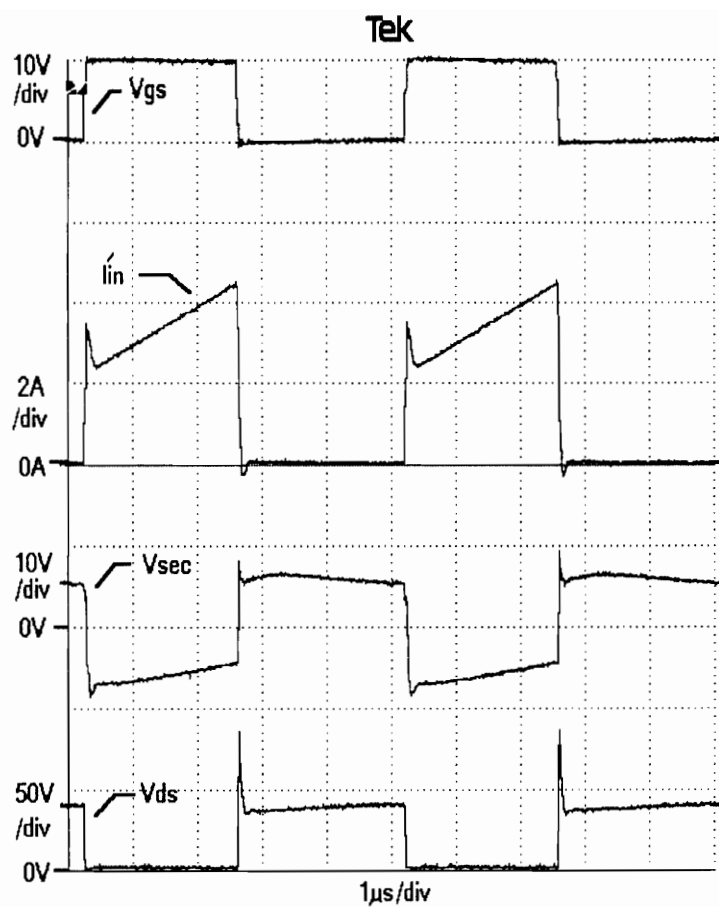**Figure 5.13. Schematic of the entire ZCS-QRC test circuit used**
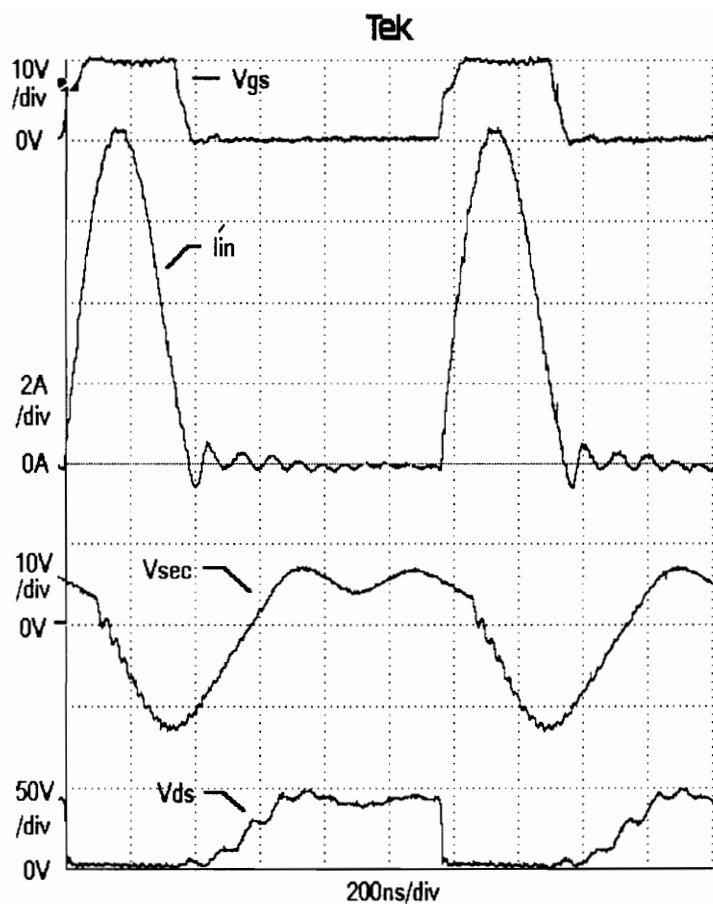
Figure 5.14. Waveforms of the ZCS-QRC circuit: converter operating at the nominal line/load conditions
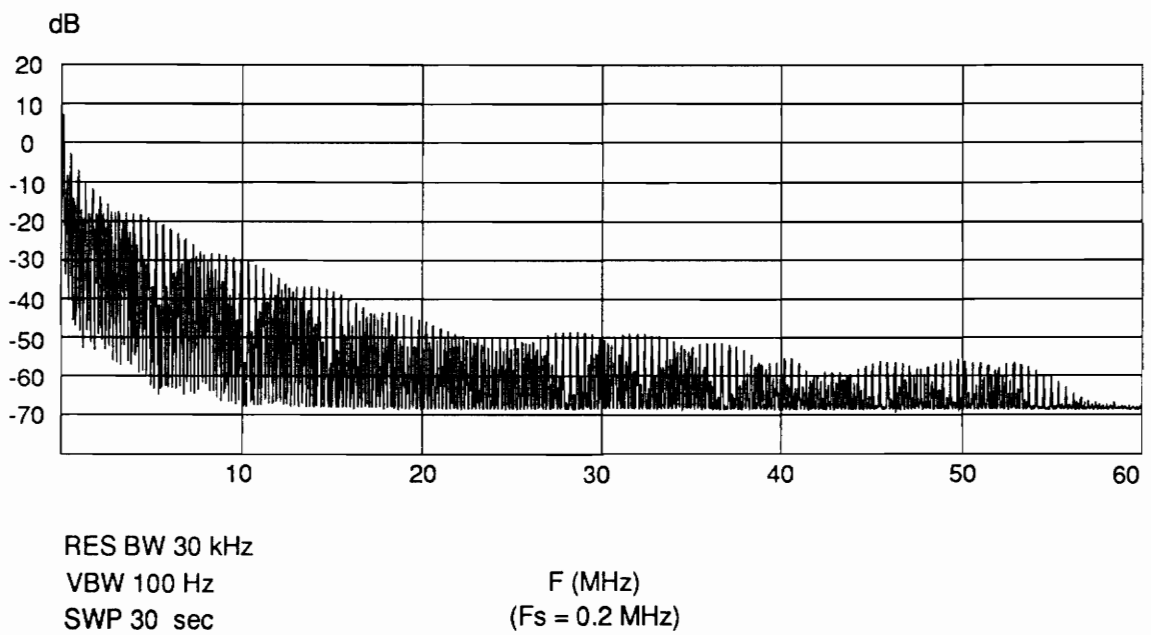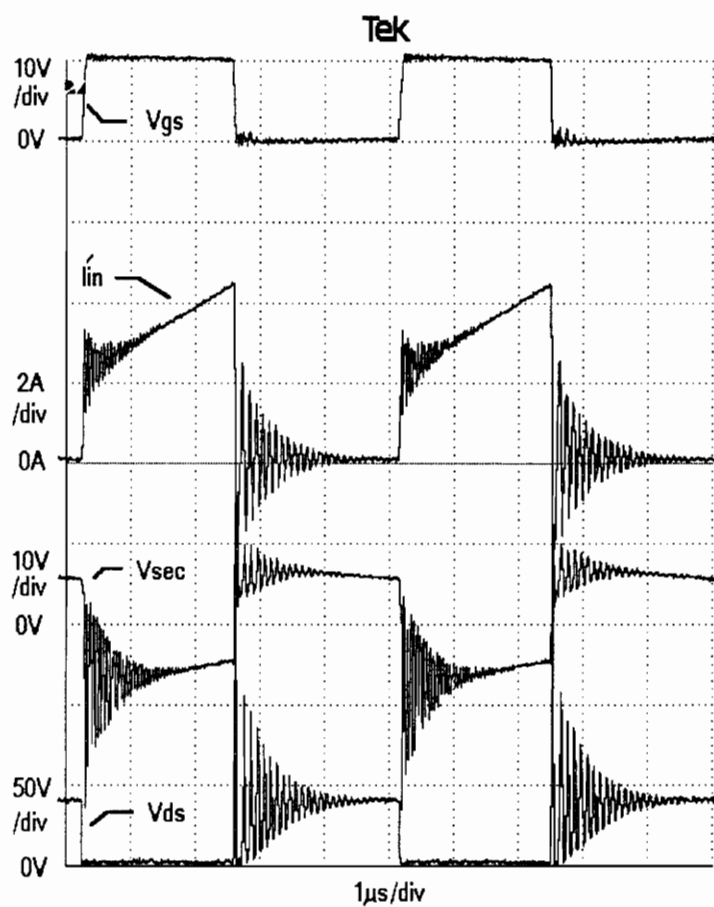
Figure 5.15. Input current spectrum of the ZCS-QRC circuit
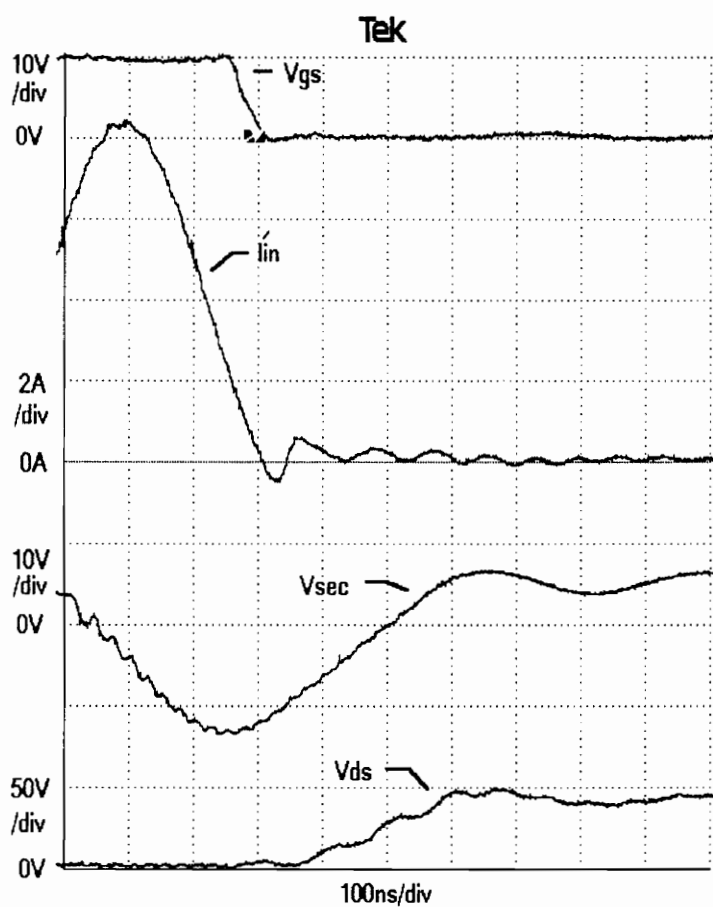
Figure 5.16. Close-up of the waveforms for the ZCS-QRC test circuit: converter operating at the nominal line/load conditions

(a)
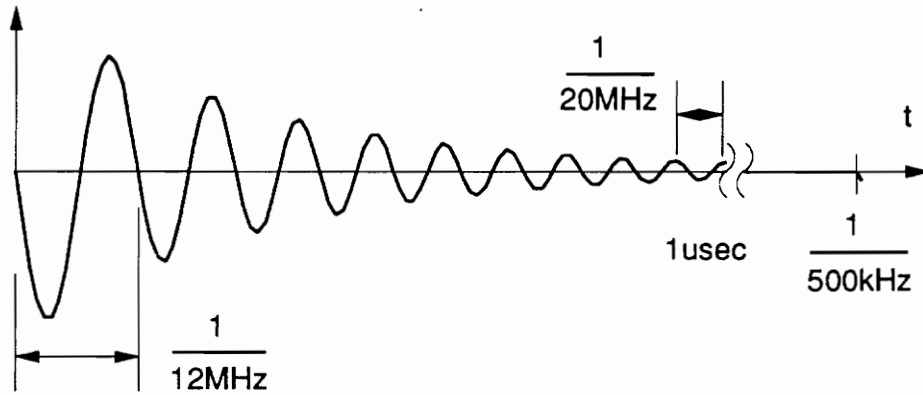
(b)
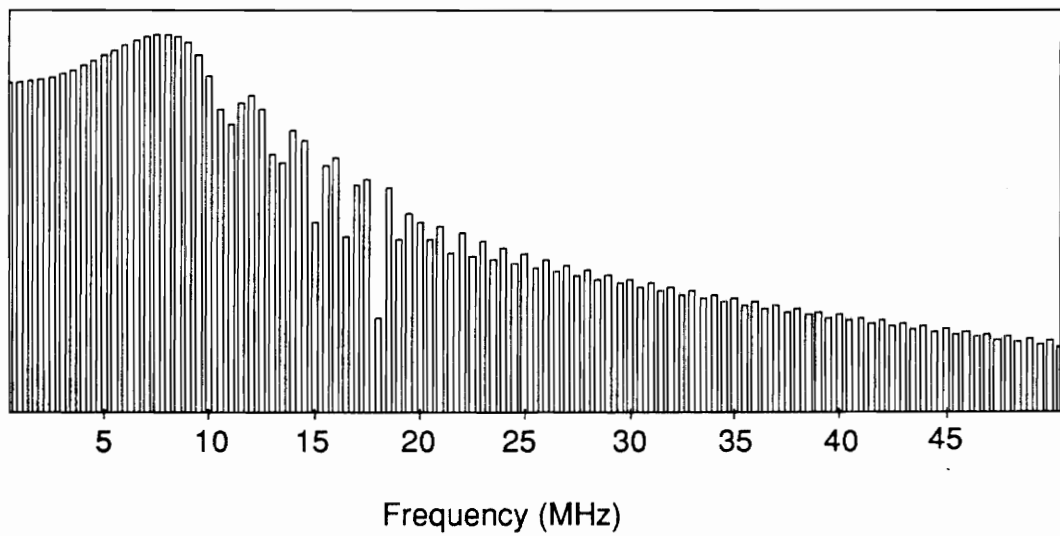
Figure 5.17. Exponentially damped, frequency modulated sine wave: (a) time domain plot, and (b) its associated spectrum

5.2.3 ZVS-QRC

Figure 5.18 shows the schematic of the ZVS-QRC circuit that was used for the results in this subsection. Similar to the PWM experiments, two sets of measurements were taken: one with the snubber in place and one with the snubber omitted. The resonant tank was designed for a minimum switching frequency of 800 kHz using the design procedures found in [14]. The same resonant tank is used for both sets of measurements.

Figure 5.19 shows the experimental waveforms of the snubbered ZVS-QRC operating at the nominal line/load conditions.

The snubber shown in Fig. 5.18 was designed according to the same procedure as the PWM snubbers [14]. Because the input current waveform is virtually free of any ringing, it would be expected that the spectrum would be very close to an ideal spectrum (seen in Chapter 3). There is, however, a ringing frequency of approximately 2 MHz caused by the junction capacitance of the output diode resonating with the parasitic inductance on the secondary side. Since the amplitude of this ringing is very small and relatively low in frequency, the spectrum of the input current would not be expected to be altered very much.

Figure 5.20 shows the spectrum of the input current waveform of the snubbered ZVS-QRC. The envelope of the spectrum shows no strong peaks from circuit oscillations and is similar to what would be expected (based on Chapter 3 examples).

With the snubber omitted, the circuit was run at the nominal line/load conditions. Figure 5.21 shows the waveforms of the ZVS-QRC. Because the resonant tank shapes the drain-to-source voltage across the FET, there is no ringing on the device at turn-off. However, when the output

diode turns off, an oscillation between the junction capacitance of the output diode and the parasitic inductance of the secondary side occurs. This ringing is reflected back to the primary side and is evident in the input current waveform. Considering the discussion in section 5.2.1.1 about an exponentially damped sine wave, it would be expected that this ringing will cause a distortion in the input current spectrum around harmonics of the 9 MHz ringing frequency.

Figure 5.22 shows the input current spectrum for the snubberless ZVS-QRC operating at nominal line/load conditions. Examining the spectrum, peaks can be found in the envelope of the spectrum around 9 MHz and 18 MHz. These sets of peaks can be attributed to harmonics of the ringing frequency of 9 MHz as seen in the circuit waveforms.
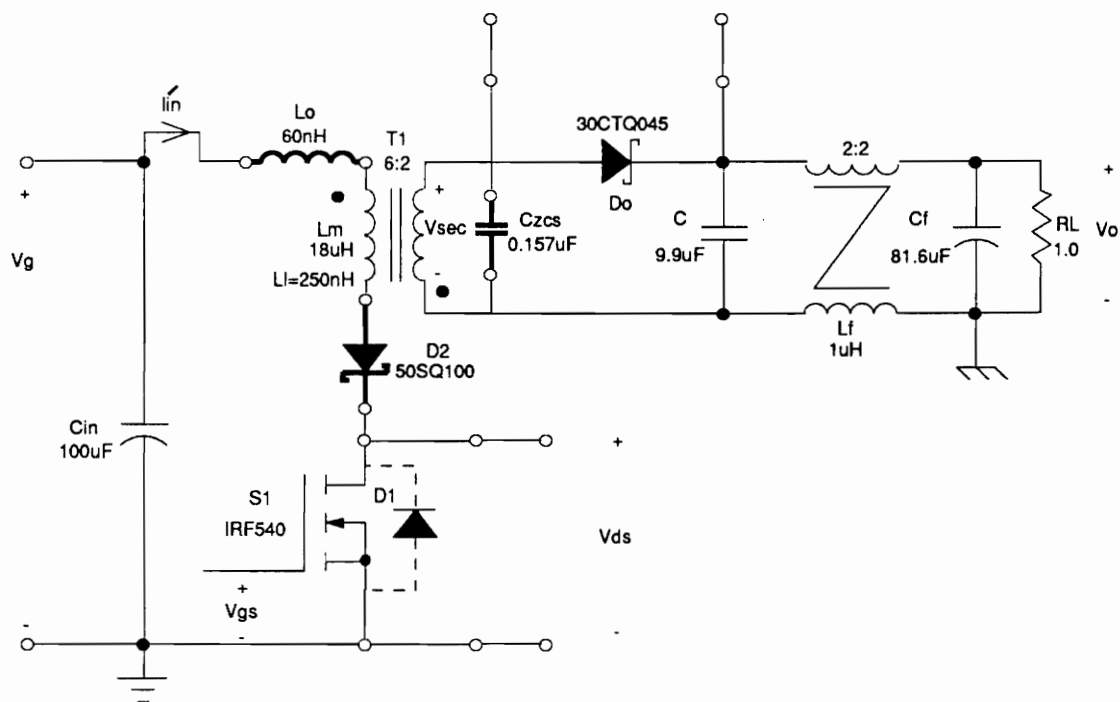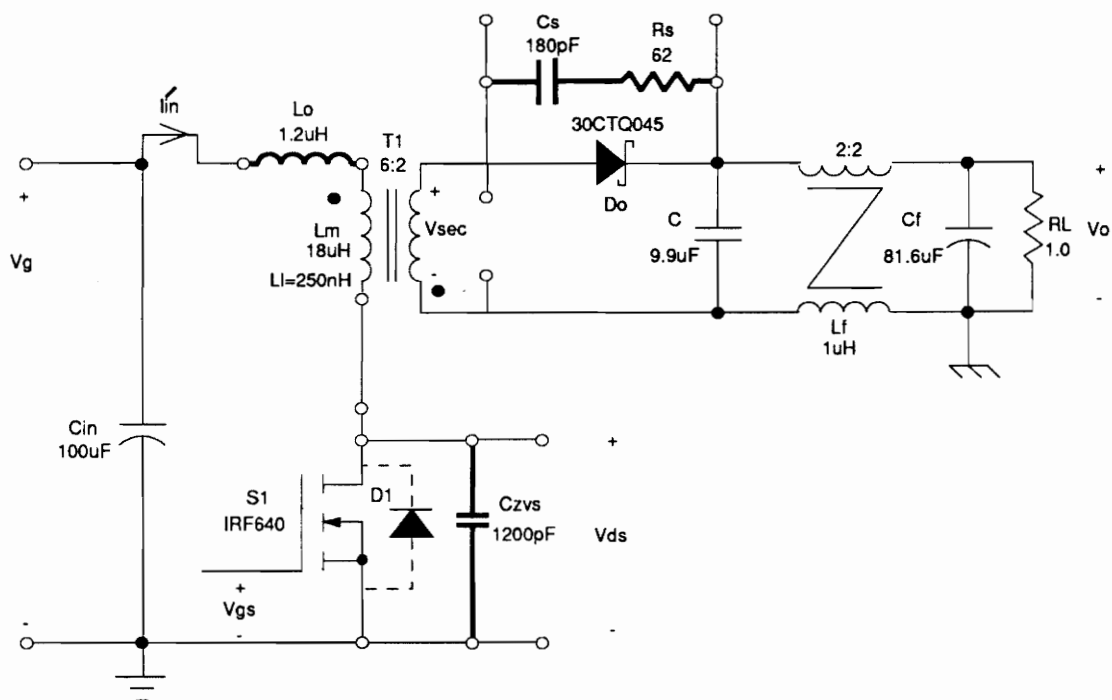
Figure 5.18. Schematic of the entire ZVS-QRC test circuit used
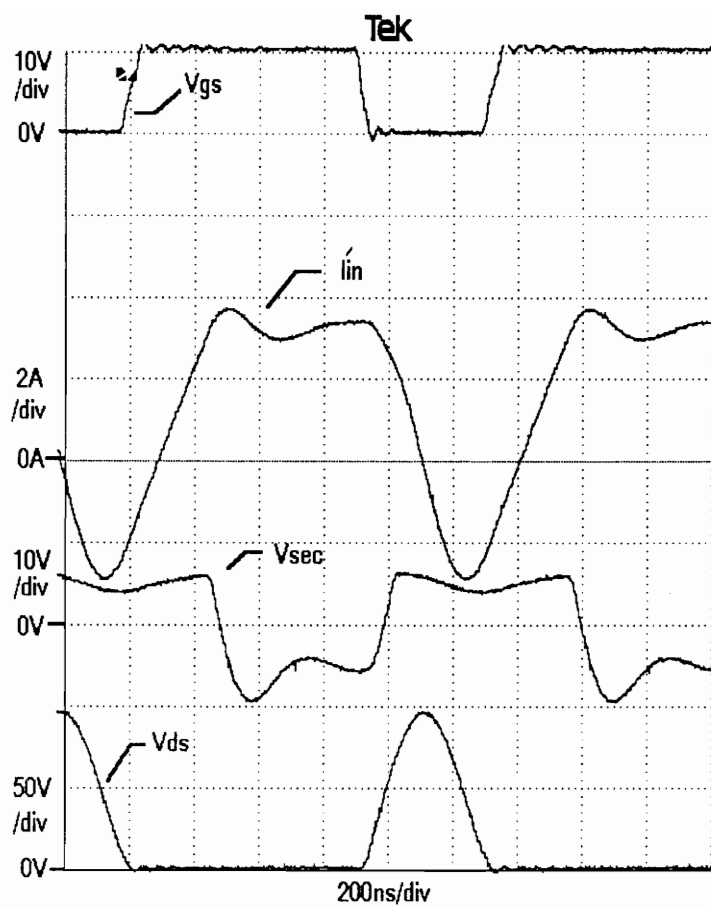
Figure 5.19. Waveforms of the snubbered ZVS-QRC circuit: converter operating at the nominal line/load conditions

dB

RES BW 30 kHz
VBW 100 Hz
SWP 30 sec

F (MHz)
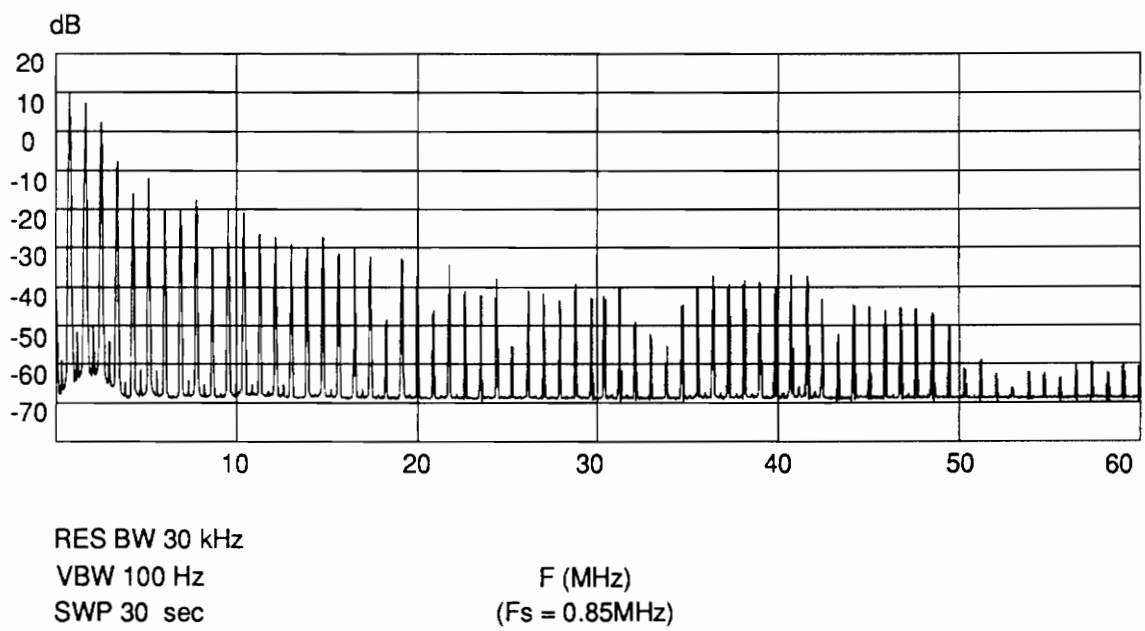(Fs = 0.89MHz)
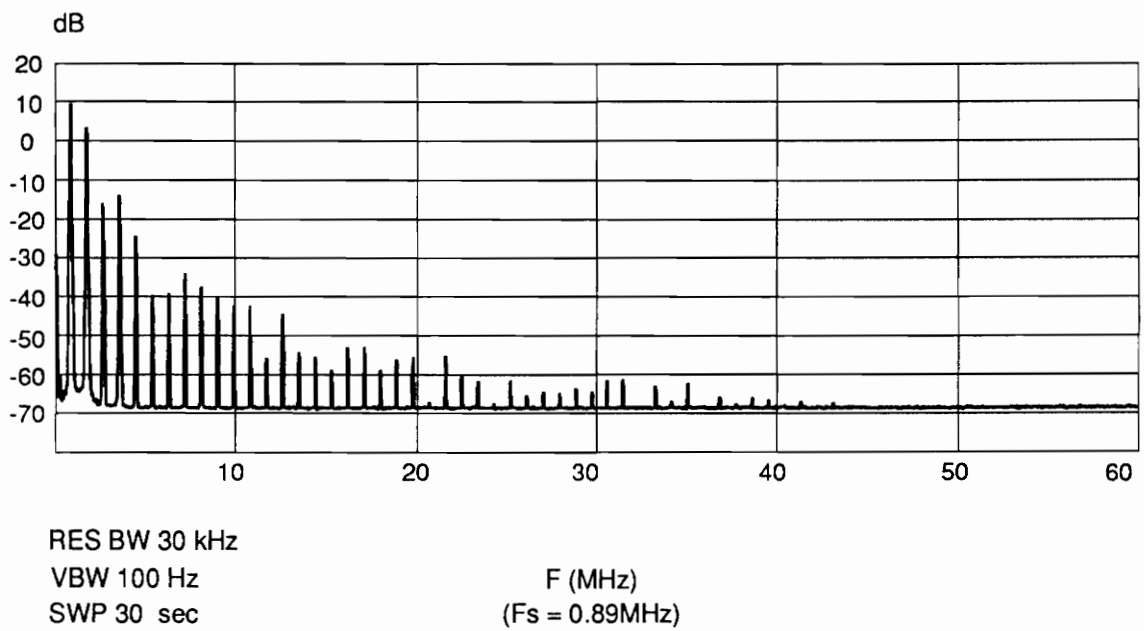
Figure 5.20.   Input current spectrum of the snubbered ZVS-QRC circuit
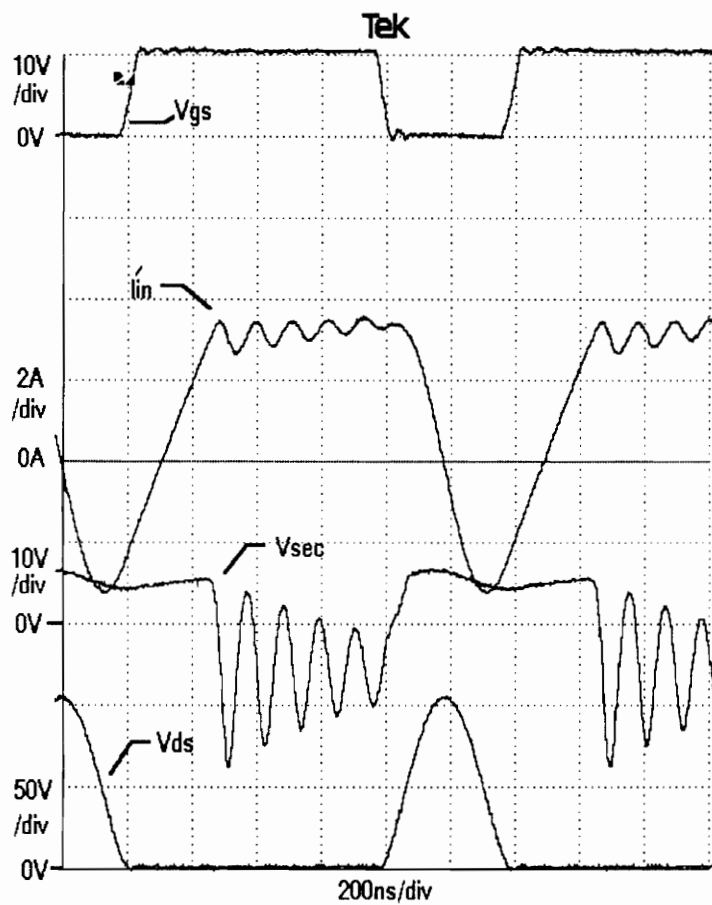
Figure 5.21. **Waveforms of the snubberless ZVS-QRC circuit:** converter operating at the nominal line/load conditions

dB

```
 20 ┬─────────┬─────────┬─────────┬─────────┬─────────┬
 10 ┤         │         │         │         │         │
  0 ┤         │         │         │         │         │
-10 ┤         │         │         │         │         │
-20 ┤         │         │         │         │         │
-30 ┤         │         │         │         │         │
-40 ┤         │         │         │         │         │
-50 ┤         │         │         │         │         │
-60 ┤         │         │         │         │         │
-70 ┴─────────┴─────────┴─────────┴─────────┴─────────┴
         10        20        30        40        50        60
```

RES BW 30 kHz
VBW 100 Hz   F (MHz)
SWP 30 sec   (Fs = 0.85MHz)
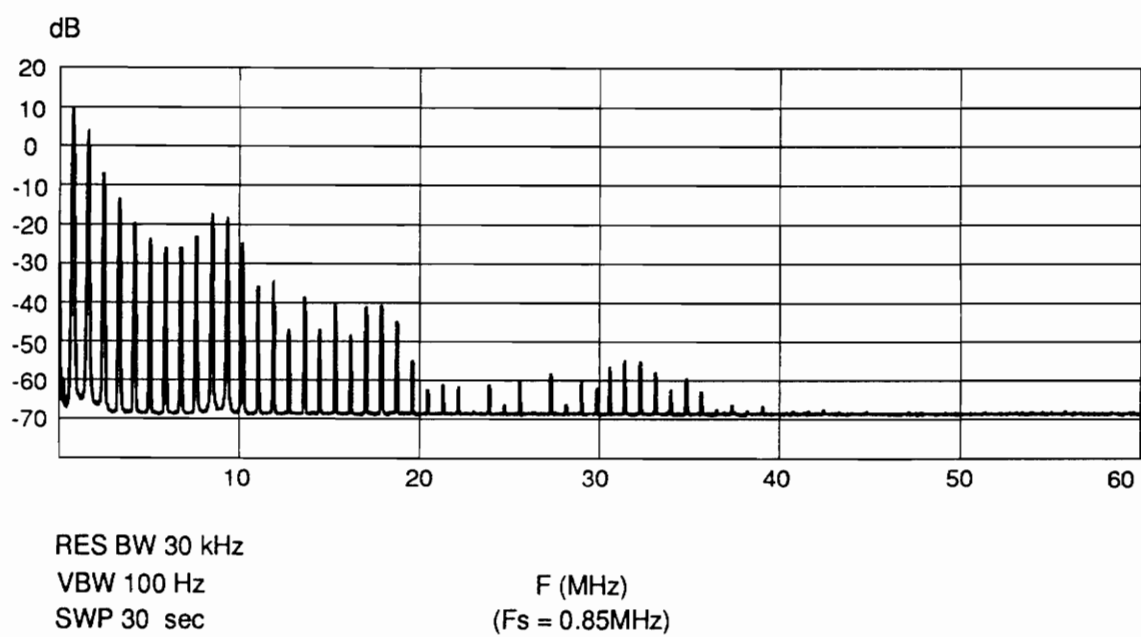
Figure 5.22.   Input current spectrum of the snubberless ZVS-QRC circuit

Experimental Results and Comparisons   142

5.2.4 ZVS-MRC

Figure 5.23 shows the schematic of the circuit used for the ZVS-MRC experiment. A complete description of the multi-resonant conversion technique can be found in [19]. The circuit was designed according to the guidelines presented in [14] for a minimum switching frequency of 1 MHz. The ZVS-MRC circuit works by shaping both the primary and secondary waveforms.

Figure 5.24 shows the waveforms of the ZVS-MRC operating at the nominal line/load conditions. The input current waveform is very smooth and rounded. The envelope of the spectrum for this waveform should not show any large peaks.

Figure 5.25 shows the input current spectrum of the ZVS-MRC operating at the nominal line/load conditions. The harmonics decay rather steadily, and there are no strong oscillations represented in the current spectrum.

Figure 5.23. Schematic of the entire ZVS-MRC test circuit used
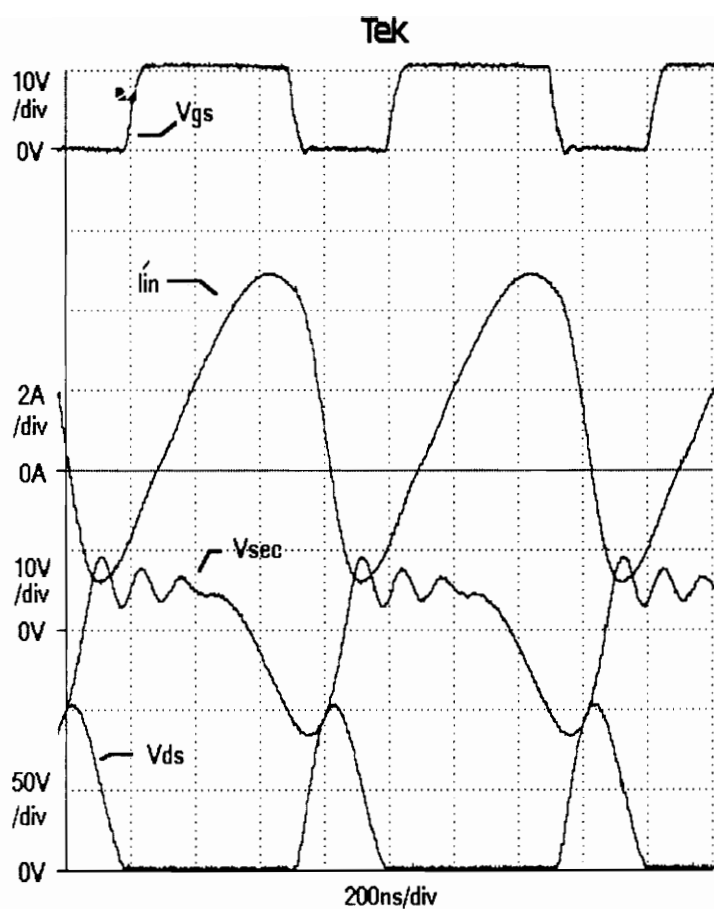
Figure 5.24. **Waveforms of the ZVS-MRC circuit:** converter operating at the nominal line/load conditions

dB

```
20
10
 0
-10
-20
-30
-40
-50
-60
-70
        10        20        30        40        50        60
```

RES BW 30 kHz
VBW 100 Hz   F (MHz)
SWP 30 sec   (Fs = 1.2MHz)
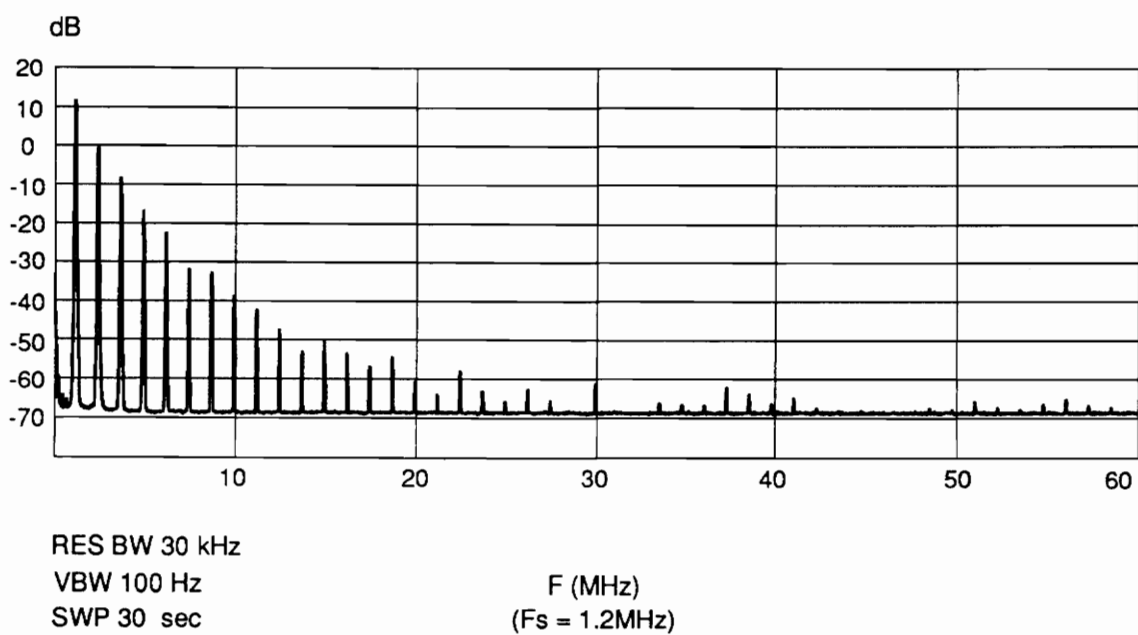
Figure 5.25. Input current spectrum of the ZVS-MRC circuit

5.3 Comparisons

Figures 5.26 and 5.27 show all of the spectral plots from each of the experiments described in section 5.2. All of the plots have the same x and y scales and were made with the same resolution bandwidth (30 kHz), video bandwidth (100 Hz) and sweep time (30 sec) set on the spectrum analyzer.

The effect of the snubbers on the PWM converter can be seen by comparing the top two plots of Fig. 5.25. By using the snubbers, the lower harmonics now decay more naturally when compared to the plot of the PWM converter without the snubbers. Without the snubbers, the ringing on the FET and output diode caused harmonics of the spectrum around 10 MHz, 20 MHz, and 40 Mhz to be offset vertically. Although there appears to be two envelopes associated with the snubbered PWM converter, the envelope is still smoother and more regular than the spectrum of the PWM converter without the snubbers.

It was determined that the peaks and valleys of the PWM spectral plots are a strong function of the squareness of the current waveform. Since all of the other current waveforms were very rounded in shape, their spectral plots were absent of these regular peaks and valleys.

The ZCS-QRC spectrum for the most part has higher spectral peaks for a given frequency when compared to all of the other converters tested. Some of these peaks could be reduced or eliminated by completely eliminating the oscillation shown on the drain-to-source voltage waveform. If the ringing frequency were completely eliminated, or at least was not being modulated, most of the high frequency harmonics would not be present.

The two ZVS-QRC spectral plots extend to a much lower frequency (40 MHz) than the PWM and the ZCS-QRCs; however, in the snubberless ZVS-QRC, there are peaks in the envelope of the spectrum at lower frequencies. These peaks could cause a problem in filtering because although the filtering requirement may be met at for example 6 MHz, it may not guarantee that the requirement will be met at 9 MHz. The spectrum of the snubbered ZVS-QRC does not have any irregular peaks, and it would be easier to meet the filtering requirements for this converter than for the PWM (both), ZCS-QRCs or ZVS-QRCs (snubberless).

The spectral plot of the ZVS-MRC is the most desirable of all of the plots. The harmonics steadily decay which would lead to easier filtering (since there are no sudden peaks). Also, the ZVS-MRC's ability to run at higher frequencies contributes to easier filtering because even low harmonics are still at a much higher frequency (higher frequencies are easier to filter).
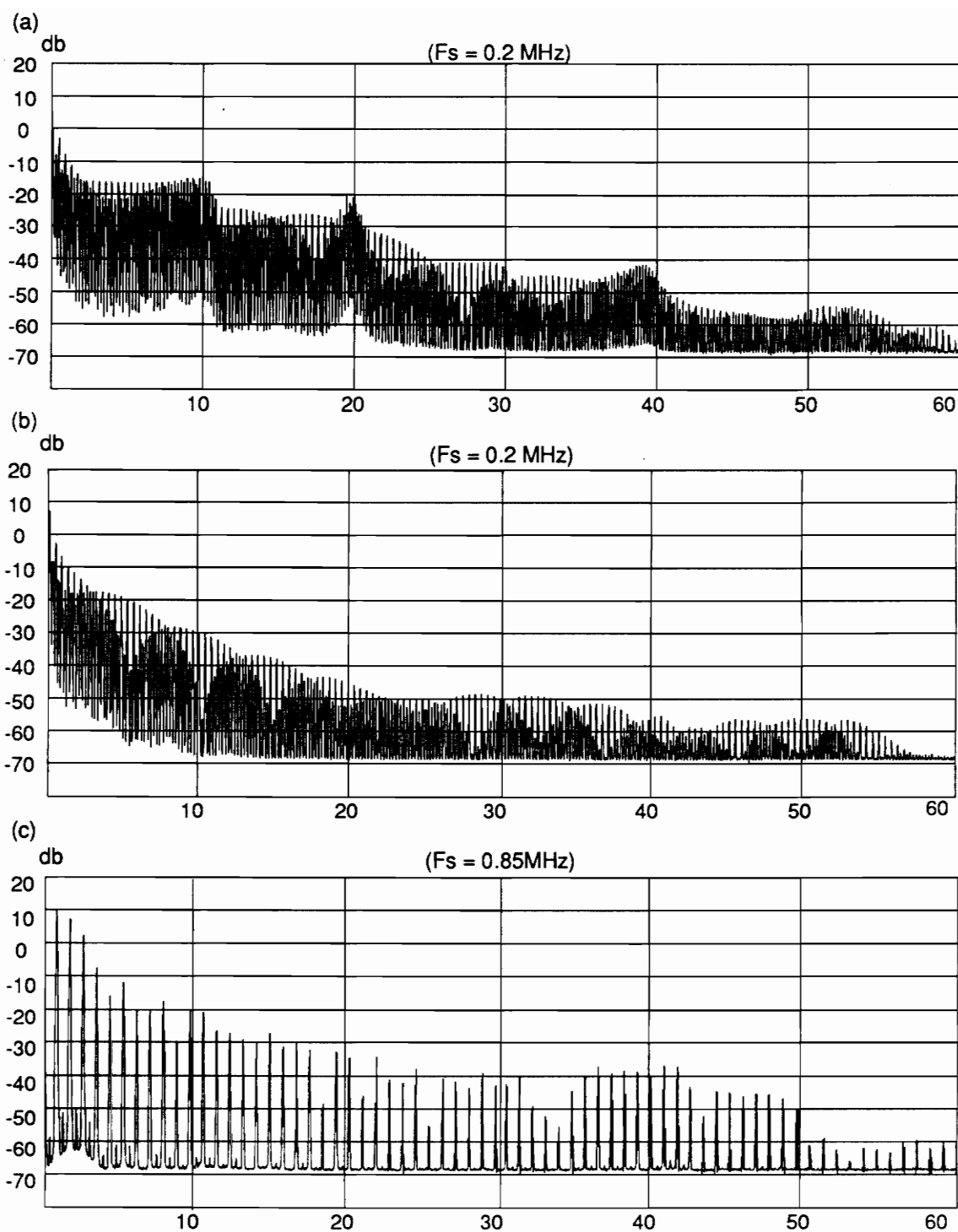
Figure 5.26. Input current spectral plots for several converters: (a) the snubberless PWM converter, (b) the snubbered PWM converter, and (c) the ZCS-QRC
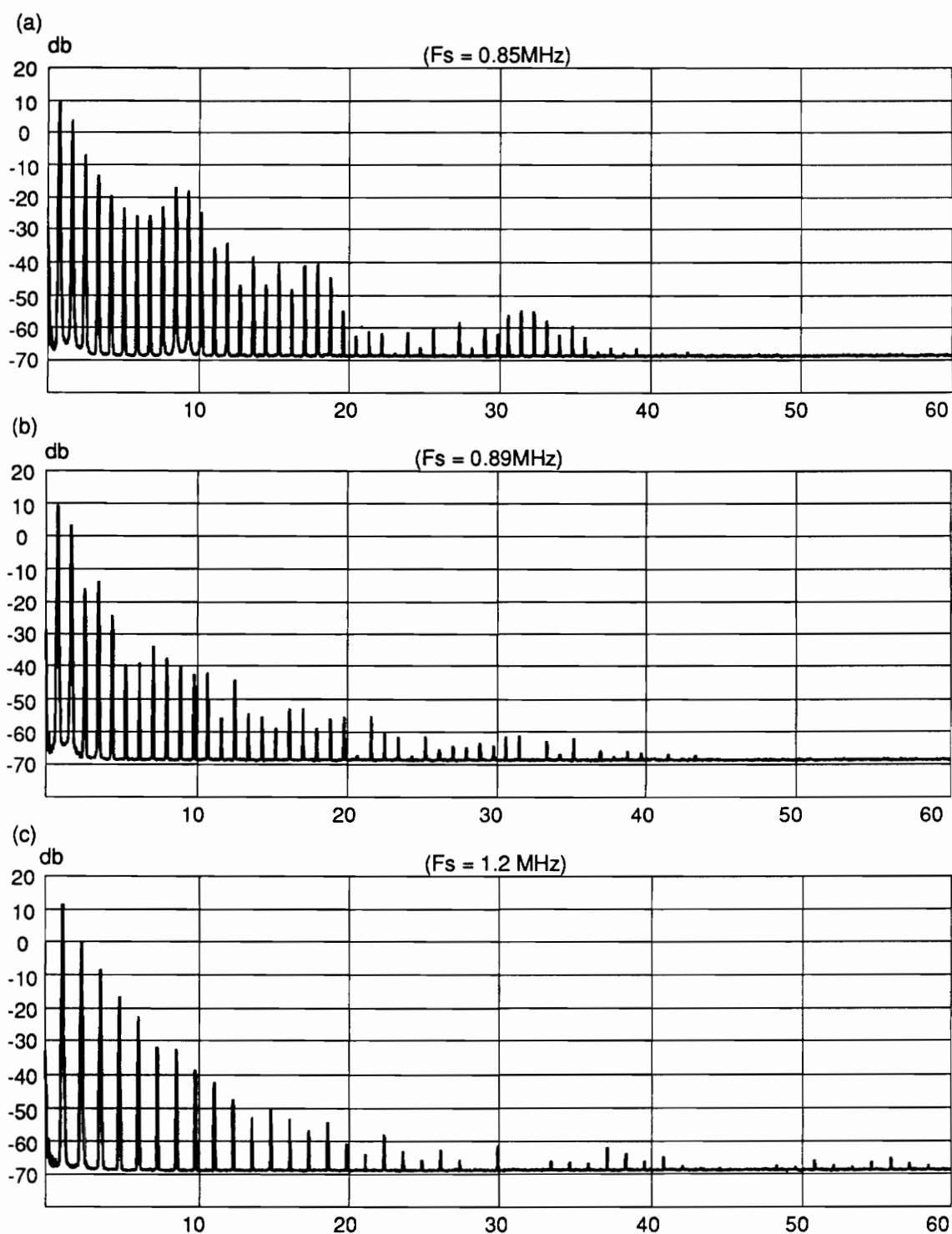
Figure 5.27. Input current spectral plots for several converters: (a) the snubberless ZVS-QRC, (b) the snubbered ZVS-QRC, and (c) the ZVS-MRC

Chapter 6

Summary and Conclusions

In Chapters 2 through 4, a brief review of the operation of the flyback PWM, ZCS-QRC, and ZVS-QRC converters was offered. This review also included equations that describe the input current for each of the converters. The input current spectrum was derived for each of the three converters by way of a Fourier analysis of the input current waveform description. The final forms of these equations were written so that the inductor current term was factored out. This sets up a basis for normalized characteristics of the converter; that is, the equations can be plotted independent of the inductor current.

Also, for each of these converters, a common converter specification was used to determine the theoretical input current spectral components in each chapter. Six cases were plotted: low-line and light-load; low-line and full-load; nominal-line and light-load; nominal-line and full-load; high-line and light-load; and high-line and full-load. A qualitative comparison was offered. In the comparison, it was determined that the attenuation of the spectrum is more sensitive to load conditions than to line conditions. This can be seen in the analytical equations because each set of equations is directly proportional to the inductor (hence load) current.

Also, in Chapters 2-4, the derived analytical equations were tested against experimental results. For this comparison to be fair, parameters needed in the equations were determined from the oscillogram. After ascertaining the desired parameters, the values of the spectrum were calculated and compared to experimental results. Each experiment showed that the derived equations do represent an accurate description of the input current spectrum. Although the equations could be used to calculate any number of harmonics, only the first twenty harmonics were calculated. Taking parasitic ringing frequencies into account, these results compared well to experimental results. Chapter 5 expanded in more detail.

In Chapter 3, an equation was developed that will give the ratio of input current spectrum for the flyback ZCS-QRC to the input current spectrum for the flyback PWM converter for a given $M_{max} \geq 1$ and harmonic number n. This ratio was plotted and showed that there are only two cases when the magnitude of the ZCS-QRC is larger than the magnitude for a PWM converter: 1) for $m = 1$, and 2) $m = 2$. For all of the other cases, the magnitude of the PWM spectrum is larger than the magnitude of the ZCS-QRC spectrum. Also, this equation of the ratio was simplified using an approximation of the input current waveform as a raised sine wave. A final equation was offered that greatly simplifies the computation of the original equation.

Chapter 5 was used to describe in more details, the effects of the parasitics in the circuit. It was determined that any parasitic oscillation on any of the waveforms always affected the input current spectrum.

An experimental PWM circuit was tested with and without snubbers in Chapter 5, and both sets of spectral plots were shown. The effect of the snubbers on the input current spectrum was very evident in both the spectral plots and the circuit waveforms. Also, as expected, the quasi-square shape of the input current waveform contributes to significant number of higher order harmonics. This broad range of significant harmonics is the main reason why input filters are more difficult to construct. A filter to attenuate a broad range of harmonics is much harder to build than a filter to attenuate only a narrow range (as in quasi-sine waves).

Also in Chapter 5, a flyback ZCS-QRC experimental circuit was constructed, and its input current spectrum was shown. The parasitics, namely the drain to source capacitance of the FET, become very important. Because this capacitance varies during the off-time, the frequency of oscillation caused by this capacitance (and the leakage inductance) also changes. The effect of this frequency modulation is described and is the main cause of significant higher order harmonics in the spectral plot of the input current.

A flyback ZVS-QRC was also tested with and without snubbers. The effects of the parasitic oscillations on the spectrum of the circuit without a snubber was very evident when compared to the spectrum of the circuit with the snubber. Finally, in Chapter 5 a flyback ZVS-MRC was constructed and tested. The input current spectrum was also shown. Because the MRC technology utilizes most of the parasitics, the stray effects of the parasitics were minimal. The range of the significant harmonics was less than the other converters. Also, a steady attenuation of the spectrum could be seen. This shows that if after a certain harmonic number, say n, needs to be attenuated, harmonic number $n + 1$ will not be greater than n as might be the case in all of the other converters. This is one more advantage of the MRC technology.

Appendix A

Derivation of the Fourier Coefficients for the Flyback

ZCS-QRC

Section 3.4 showed the input current of the flyback ZCS-QRC (Fig. 3.1) to be:

$$I'_{in}(t) = \frac{1}{n} \cdot \begin{cases} yt & T_0 < t < T_1 \\ I_x + u \sin(\omega_0(t - T_{01})) & T_1 < t < T_2 \\ 0 & T_2 < t < T_4 \end{cases} , \qquad (A.1)$$

where all the variables were defined in that section.

The coefficients a_m and b_m can be found from the following relations [10]:

$$a_m = \int^{T_s} f(t) \cos x_m t \ dt \quad m = 0,1,2, ... \qquad (A.2)$$

$$b_m = \int^{T_s} f(t) \sin x_m t \ dt \quad m = 0,1,2, ... \qquad (A.3)$$

where

$$x_m = 2m\pi f_s \ .$$ (A.4)

This allows a function $f(t)$ to be expressed as a series of sine and cosine terms:

$$f(t) = \sum_{m=0}^{\infty} a_m \cos x_m t \ + \ b_m \sin x_m t \ .$$ (A.5)

Equations (A.2) and (A.3) represent the Fourier coefficients of the input current if $f(t) = I'_{in}(t)$. Substituting the equation of the input current ((A.1)) into (A.2) and (A.3) and integrating over one switching period (0 to T_s) will give:

$$a_m = \frac{2}{T_s} (g_{a1} + g_{a2} + g_{a3}) \ ,$$ (A.6)

$$b_m = \frac{2}{T_s} (g_{b1} + g_{b2} + g_{b3}) \ ,$$ (A.7)

where,

$$g_{a1} = \int_0^{T_1} yt \cos x_m t \ dt \ ,$$ (A.8)

$$g_{a2} = \int_{T_{01}}^{T_A} I_x \cos x_m t \ dt \ ,$$ (A.9)

$$g_{a3} = \int_{T_{01}}^{T_A} [u \sin \omega_o(t - T_{01}) \cos x_m t] \ dt \ ,$$ (A.10)

$$g_{b1} = \int_0^{T_1} yt \sin x_m t \ dt \ , \tag{A.11}$$

$$g_{b2} = \int_{T_{01}}^{T_A} I_x \sin x_m t \ dt \ , \tag{A.12}$$

$$g_{b3} = \int_{T_{01}}^{T_A} [u \sin \omega_o(t - T_{01}) \sin x_m t] \ dt \ , \tag{A.13}$$

where

$$T_A = T_{01} + T_{12} \ . \tag{A.14}$$

To help in the integration, rewrite:

$$I_x + u \sin \omega_o(t - T_{01}) \tag{A.15}$$

as

$$I_x + u(\sin \omega_o t \cos \omega_o T_{01} - \cos \omega_o t \sin \omega_o T_{01}) \ . \tag{A.16}$$

Solving for g_{a1}:

$$\begin{aligned} g_{a1} &= \frac{y}{x_m} \left(\frac{\cos x_m t}{x_m} + t \sin x_m t \right) \bigg]_0^{T_{01}} \\ &= \frac{y}{x_m} \left[\frac{1}{x_m} (\cos x_m T_{01} - 1) + T_{01} \sin x_m T_{01} \right] \ . \end{aligned} \tag{A.17}$$

Solving for g_{a2}:

$$g_{a2} = \frac{I_x}{X_m} \sin x_m t \left.\right]_{T_{01}}^{T_A}$$

$$= \frac{I_x}{X_m} (\sin x_m T_A - \sin x_m T_{01}) \quad .$$

$$(A.18)$$

Solving for g_{a3}:

$$
\begin{aligned}
g_{a3} &= \frac{u\cos\omega_o T_{01}}{2}\left[-\frac{\cos(\omega_o - x_m)t}{(\omega_o - x_m)} - \frac{\cos(\omega_o + x_m)t}{(\omega_o + x_m)}\right] \\
&\quad - \frac{u\sin\omega_o T_{01}}{2}\left[\frac{\sin(\omega_o - x_m)t}{(\omega_o - x_m)} + \frac{\sin(\omega_o + x_m)t}{(\omega_o + x_m)}\right]\Bigg]_{T_{01}}^{T_A} \\[2mm]
&= \frac{u\cos\omega_o T_{01}}{2\left(\omega_o^2 - x_m^2\right)}\left[-(\omega_o + x_m)\cos(\omega_o - x_m)t - (\omega_o - x_m)\cos(\omega_o + x_m)t\right] \\
&\quad - \frac{u\sin\omega_o T_{01}}{2\left(\omega_o^2 - x_m^2\right)}\left[(\omega_o + x_m)\sin(\omega_o - x_m)t + (\omega_o - x_m)\sin(\omega_o + x_m)t\right]\Bigg]_{T_{01}}^{T_A} \\[2mm]
&= -\frac{u\cos\omega_o T_{01}}{2\left(\omega_o^2 - x_m^2\right)}\left[(\omega_o + x_m)(\cos(\omega_o - x_m)T_A - \cos(\omega_o - x_m)T_{01})\right. \\
&\qquad\qquad\qquad\qquad \left. + (\omega_o - x_m)(\cos(\omega_o + x_m)T_A - \cos(\omega_o + x_m)T_{01})\right] \\[2mm]
&\quad - \frac{u\sin\omega_o T_{01}}{2\left(\omega_o^2 - x_m^2\right)}\left[(\omega_o + x_m)(\sin(\omega_o - x_m)T_A - \sin(\omega_o - x_m)T_{01})\right. \\
&\qquad\qquad\qquad\qquad \left. + (\omega_o - x_m)(\sin(\omega_o + x_m)T_A - \sin(\omega_o + x_m)T_{01})\right] \\[2mm]
&= -\frac{u\cos\omega_o T_{01}}{2\left(\omega_o^2 - x_m^2\right)}\left[(\omega_o + x_m)(\cos\omega_o T_A \cos x_m T_A + \sin\omega_o T_A \sin x_m T_A\right. \\
&\qquad\qquad\qquad\qquad - \cos\omega_o T_{01}\cos x_m T_{01} - \sin\omega_o T_{01}\sin x_m T_{01}) \\
&\qquad\qquad\qquad + (\omega_o - x_m)(\cos\omega_o T_A \cos x_m T_A - \sin\omega_o T_A \sin x_m T_A \\
&\qquad\qquad\qquad\qquad \left. - \cos\omega_o T_{01}\cos x_m T_{01} + \sin\omega_o T_{01}\sin x_m T_{01})\right] \\[2mm]
&\quad - \frac{u\sin\omega_o T_{01}}{2\left(\omega_o^2 - x_m^2\right)}\left[(\omega_o + x_m)(\sin\omega_o T_A \cos x_m T_A - \cos\omega_o T_A \sin x_m T_A\right. \\
&\qquad\qquad\qquad\qquad - \sin\omega_o T_{01}\cos x_m T_{01} + \cos\omega_o T_{01}\sin x_m T_{01}) \\
&\qquad\qquad\qquad + (\omega_o - x_m)(\sin\omega_o T_A \cos x_m T_A + \cos\omega_o T_A \sin x_m T_A \\
&\qquad\qquad\qquad\qquad \left. - \sin\omega_o T_{01}\cos x_m T_{01} - \cos\omega_o T_{01}\sin x_m T_{01})\right]
\end{aligned}
$$

$$g_{a3} = \frac{u \cos \omega_o T_{01}}{\left(\omega_o^2 - x_m^2\right)} \left[\omega_o \cos \omega_o T_A \cos x_m T_A + x_m \sin \omega_o T_A \sin x_m T_A\right.$$

$$\left. - \omega_o \cos \omega_o T_{01} \cos x_m T_{01} - x_m \sin \omega_o T_{01} \sin x_m T_{01}\right]$$

$$- \frac{u \sin \omega_o T_{01}}{\left(\omega_o^2 - x_m^2\right)} \left[\omega_o \sin \omega_o T_A \cos x_m T_A - x_m \cos \omega_o T_A \sin x_m T_A\right.$$

$$\left. - \omega_o \sin \omega_o T_{01} \cos x_m T_{01} + x_m \cos \omega_o T_{01} \sin x_m T_{01}\right]$$

$$= \frac{-u}{\left(\omega_o^2 - x_m^2\right)} \left\{ \cos \omega_o T_{01}\left[\omega_o\left(\cos \omega_o T_A \cos x_m T_A - \cos \omega_o T_{01} \cos x_m T_{01}\right)\right.\right.$$

$$\left.\left. + x_m\left(\sin \omega_o T_A \sin x_m T_A - \sin \omega_o T_{01} \sin x_m T_{01}\right)\right]\right.$$

$$+ \sin \omega_o T_{01}\left[\omega_o\left(\sin \omega_o T_A \cos x_m T_A - \sin \omega_o T_{01} \cos x_m T_{01}\right)\right.$$

$$\left.\left. + x_m\left(\cos \omega_o T_{01} \sin x_m T_{01} - \cos \omega_o T_A \sin x_m T_A\right)\right]\right\}$$

$$= \frac{-u}{\left(\omega_o^2 - x_m^2\right)} \left\{\omega_o \cos x_m T_A\left[\cos \omega_o T_{01} \cos \omega_o T_A + \sin \omega_o T_{01} \sin \omega_o T_A\right]\right.$$

$$- \omega_o \cos x_m T_{01}\left[\cos \omega_o T_{01} \cos \omega_o T_{01} + \sin \omega_o T_{01} \sin \omega_o T_{01}\right]$$

$$\left. + x_m \sin x_m T_A\left[\cos \omega_o T_{01} \sin \omega_o T_A - \sin \omega_o T_{01} \cos \omega_o T_A\right]\right\}$$

$$= \frac{-u}{\left(\omega_o^2 - x_m^2\right)} \left\{\omega_o\left[\cos x_m T_A \cos \omega_o(T_{01} - T_A) - \cos x_m T_{01}\right]\right.$$

$$\left. + x_m \sin x_m T_A \sin \omega_o(T_A - T_{01})\right\}$$

$$= \frac{-u}{\left(\omega_o^2 - x_m^2\right)} \left\{\omega_o\left[\cos x_m T_A \cos \omega_o T_{12} - \cos x_m T_{01}\right]\right.$$

$$\left. + x_m \sin x_m T_A \sin \omega_o T_{12}\right\}$$

$$= \frac{-u}{\left(\dfrac{\omega_o^2}{x_m^2} - 1\right)x_m} \left\{ \frac{\omega_o}{x_m}\left[\cos x_m T_A \cos \omega_o T_{12} - \cos x_m T_{01}\right]\right.$$

$$\left. + \sin x_m T_A \sin \omega_o T_{12}\right\} \quad .$$

(A.19)

Solving for g_{b1}:

$$g_{b1} = \frac{y}{x_m} \left(\frac{\sin x_m t}{x_m} - t \cos x_m t \right) \Bigg]_0^{T_{01}}$$

$$= \frac{y}{x_m} \left[\frac{\sin x_m T_{01}}{x_m} - T_{01} \cos x_m T_{01} \right] \quad . \tag{A.20}$$

Solving for g_{b2}:

$$g_{b2} = -\frac{I_x}{x_m} \cos x_m t \Bigg]_{T_{01}}^{T_A}$$

$$= \frac{I_x}{x_m} (\cos x_m T_{01} - \cos x_m T_A) \quad . \tag{A.21}$$

Solving for g_{b3}:

$$g_{b3} = \frac{u \cos \omega_o T_{01}}{2} \left[\frac{\sin(\omega_o - x_m)t}{(\omega_o - x_m)} - \frac{\sin(\omega_o + x_m)t}{(\omega_o + x_m)} \right]$$

$$- \frac{u \sin \omega_o T_{01}}{2} \left[\frac{\cos(\omega_o - x_m)t}{(\omega_o - x_m)} - \frac{\cos(\omega_o + x_m)t}{(\omega_o + x_m)} \right] \Big]_{T_{01}}^{T_A}$$

$$= \frac{u \cos \omega_o T_{01}}{2(\omega_o^2 - x_m^2)} [(\omega_o + x_m) \sin(\omega_o - x_m)t - (\omega_o - x_m) \sin(\omega_o + x_m)t]$$

$$- \frac{u \sin \omega_o T_{01}}{2(\omega_o^2 - x_m^2)} [(\omega_o + x_m) \cos(\omega_o - x_m)t - (\omega_o - x_m) \cos(\omega_o + x_m)t] \Big]_{T_{01}}^{T_A}$$

$$= \frac{u \cos \omega_o T_{01}}{2(\omega_o^2 - x_m^2)} [(\omega_o + x_m)(\sin(\omega_o - x_m)T_A - \sin(\omega_o - x_m)T_{01})$$

$$- (\omega_o - x_m)(\sin(\omega_o + x_m)T_A - \sin(\omega_o + x_m)T_{01})]$$

$$- \frac{u \sin \omega_o T_{01}}{2(\omega_o^2 - x_m^2)} [(\omega_o + x_m)(\cos(\omega_o - x_m)T_A - \cos(\omega_o - x_m)T_{01})$$

$$- (\omega_o - x_m)(\cos(\omega_o + x_m)T_A - \cos(\omega_o + x_m)T_{01})]$$

$$= \frac{u \cos \omega_o T_{01}}{2(\omega_o^2 - x_m^2)} [(\omega_o + x_m)(\sin \omega_o T_A \cos x_m T_A - \cos \omega_o T_A \sin x_m T_A$$

$$- \sin \omega_o T_{01} \cos x_m T_{01} + \cos \omega_o T_{01} \sin x_m T_{01})$$

$$- (\omega_o - x_m)(\sin \omega_o T_A \cos x_m T_A + \cos \omega_o T_A \sin x_m T_A$$

$$- \sin \omega_o T_{01} \cos x_m T_{01} - \cos \omega_o T_{01} \sin x_m T_{01})]$$

$$- \frac{u \sin \omega_o T_{01}}{2(\omega_o^2 - x_m^2)} [(\omega_o + x_m)(\cos \omega_o T_A \cos x_m T_A + \sin \omega_o T_A \sin x_m T_A$$

$$- \cos \omega_o T_{01} \cos x_m T_{01} - \sin \omega_o T_{01} \sin x_m T_{01})$$

$$- (\omega_o - x_m)(\cos \omega_o T_A \cos x_m T_A - \sin \omega_o T_A \sin x_m T_A$$

$$- \cos \omega_o T_{01} \cos x_m T_{01} + \sin \omega_o T_{01} \sin x_m T_{01})]$$

$$g_{b3} = \frac{u \cos \omega_o T_{01}}{\left(\omega_o^2 - x_m^2\right)} [x_m \sin \omega_o T_A \cos x_m T_A - \omega_o \cos \omega_o T_A \sin x_m T_A$$

$$- x_m \sin \omega_o T_{01} \cos x_m T_{01} + \omega_o \cos \omega_o T_{01} \sin x_m T_{01}]$$

$$- \frac{u \sin \omega_o T_{01}}{\left(\omega_o^2 - x_m^2\right)} [x_m \cos \omega_o T_A \cos x_m T_A + \omega_o \sin \omega_o T_A \sin x_m T_A$$

$$- x_m \cos \omega_o T_{01} \cos x_m T_{01} - \omega_o \sin \omega_o T_{01} \sin x_m T_{01}]$$

$$= \frac{u}{\left(\omega_o^2 - x_m^2\right)} \{ \cos \omega_o T_{01}[x_m(\sin \omega_o T_A \cos x_m T_A - \sin \omega_o T_{01} \cos x_m T_{01})$$

$$+ \omega_o(\cos \omega_o T_{01} \sin x_m T_{01} - \cos \omega_o T_A \sin x_m T_A)]$$

$$- \sin \omega_o T_{01}[x_m(\cos \omega_o T_A \cos x_m T_A - \cos \omega_o T_{01} \cos x_m T_{01})$$

$$+ \omega_o(\sin \omega_o T_A \sin x_m T_A - \sin \omega_o T_{01} \sin x_m T_{01})]\}$$

$$= \frac{u}{\left(\omega_o^2 - x_m^2\right)} \{x_m \cos x_m T_A[\cos \omega_o T_{01} \sin \omega_o T_A - \sin \omega_o T_{01} \cos \omega_o T_A]$$

$$+ \omega_o \sin x_m T_{01}[\cos \omega_o T_{01} \cos \omega_o T_{01} + \sin \omega_o T_{01} \sin \omega_o T_{01}]$$

$$- \omega_o \sin x_m T_A[\cos \omega_o T_{01} \cos \omega_o T_A + \sin \omega_o T_{01} \sin \omega_o T_A]\}$$

$$= \frac{u}{\left(\omega_o^2 - x_m^2\right)} \{x_m \cos x_m T_A \sin \omega_o(T_A - T_{01}) + \omega_o \sin x_m T_{01}$$

$$- \omega_o \sin x_m T_A \cos \omega_o(T_{01} - T_A)\}$$

$$= \frac{u}{\left(\omega_o^2 - x_m^2\right)} \{\omega_o[\sin x_m T_{01} - \sin x_m T_A \cos \omega_o T_{12}]$$

$$+ x_m \cos x_m T_A \sin \omega_o T_{12}\}$$

$$= \frac{u}{\left(\dfrac{\omega_o^2}{x_m^2} - 1\right)x_m} \left\{ \frac{\omega_o}{x_m} [\sin x_m T_{01} - \sin x_m T_A \cos \omega_o T_{12}] + \cos x_m T_A \sin \omega_o T_{12}\right\} .$$

$$(A.22)$$

Therefore, the Fourier coefficients a_m and b_m can be represented in a general equation as:

$$a_m = \frac{1}{n} a'_m \; , \tag{A.23}$$

and

$$b_m = \frac{1}{n} b'_m \; , \tag{A.24}$$

where

$$
\begin{aligned}
m\pi a'_m = \; & y\left[\frac{1}{x_m}(\cos x_m T_{01} - 1) + T_{01} \sin x_m T_{01} \right] \\
& + I_x[\sin x_m T_A - \sin x_m T_{01}] \\
& \frac{-u}{\left(\frac{\omega_o^2}{x_m^2} - 1\right)}\left\{ \frac{\omega_o}{x_m}[\cos x_m T_A \cos \omega_o T_{12} - \cos x_m T_{01}] \right. \\
& \left. + \sin x_m T_A \sin \omega_o T_{12} \right\} \; ,
\end{aligned}
\tag{A.25}
$$

and

$$
\begin{aligned}
m\pi b'_m = \; & y\left[\frac{\sin x_m T_{01}}{x_m} - T_{01} \cos x_m T_{01} \right] \\
& + I_x(\cos x_m T_{01} - \cos x_m T_A) \\
& \frac{u}{\left(\frac{\omega_o^2}{x_m^2} - 1\right)}\left\{ \frac{\omega_o}{x_m}[\sin x_m T_{01} - \sin x_m T_A \cos \omega_o T_{12}] \right. \\
& \left. + \cos x_m T_A \sin \omega_o T_{12} \right\} \; ,
\end{aligned}
\tag{A.26}
$$

Notice that each term in the above two equations has either a y, I_x, or a u in it. Recall from sections 3.2 and 3.3 that the following relations were established:

$$I_x = \frac{M}{Q}\frac{V_g}{n}\frac{(1+M)}{Z_o} \; , \tag{A.27}$$

$$y = \frac{V_g}{n} \frac{(1+M)}{Z_o} \omega_o \quad , \tag{A.28}$$

$$u = \frac{V_g}{n} \frac{(1+M)}{Z_o} \quad . \tag{A.29}$$

Rewriting y and u in terms of I_x yields:

$$y = \frac{Q}{M} I_x \omega_o \quad , \tag{A.30}$$

$$u = \frac{Q}{M} I_x \quad . \tag{A.31}$$

Using these relations, equations (A.23) - (A.26) can be rewritten as:

$$a_m = \frac{I_x}{n} a'_m \quad , \tag{A.32}$$

$$b_m = \frac{I_x}{n} b'_m \quad , \tag{A.33}$$

where

$$
\begin{aligned}
m \pi a'_m = {} & \frac{Q}{M} \left[\frac{\omega_o}{x_m} (\cos x_m T_{01} - 1) + \omega_o T_{01} \sin x_m T_{01} \right] \\
& + [\sin x_m T_A - \sin x_m T_{01}] \\
& - \frac{Q}{M} \frac{1}{d_m} \left\{ \frac{\omega_o}{x_m} [\cos x_m T_A \cos \omega_o T_{12} - \cos x_m T_{01}] \right. \\
& \left. \qquad + \sin x_m T_A \sin \omega_o T_{12} \right\} \quad ,
\end{aligned}
\tag{A.34}
$$

and

$$m\pi b'_m = \frac{Q}{M}\left[\frac{\omega_o}{x_m}\sin x_m T_{01} - \omega_o T_{01}\cos x_m T_{01}\right]$$

$$+ (\cos x_m T_{01} - \cos x_m T_A)$$

$$\frac{Q}{M}\frac{1}{d_m}\left\{\frac{\omega_o}{x_m}\left[\sin x_m T_{01} - \sin x_m T_A\cos \omega_o T_{12}\right]\right.$$

$$\left. + \cos x_m T_A\sin \omega_o T_{12}\right\}\quad . \tag{A.35}$$

Also, note that the following substitution was made:

$$d_m = \frac{\omega_o^2}{x_m^2} - 1 \quad . \tag{A.36}$$

Appendix B

Calculation of the Fourier Coefficients for the Raised

Sine Wave Approximation

Figure 3.11 shows the raised sine wave that will be used to approximate the input current for a ZCS-QRC operating at $M_{max} \geq 1$ and $Q_{min}/M_{max} \simeq 1$. The equation of that raised sine wave is:

$$f(t) = I_x + I_x \sin \omega_0 t \qquad -t_0 \leq t \leq t_1 \ , \tag{B.1}$$

where the time from $-t_0$ to t_1 is one period of the resonant cycle. The relationship between the resonant period and the switching period for a ZCS-QRC operating at $Q_{min}/M_{max} \simeq 1$ can be approximated as:

$$\frac{f_s}{f_o} \simeq \frac{M_{max}}{M_{max} + 1} \ . \tag{B.2}$$

As noted in section 3.8.2., only $M_{max} \geq 1$ is considered.

The variables t_0 and t_1 can be found by solving the following equations:

$$f(-t_0) = 0 \ , \tag{B.3}$$

$$f(0) = I_x \ , \tag{B.4}$$

$$f(t_1) = 0 \ . \tag{B.5}$$

The best solution for this system of equations is:

$$-\omega_0 t_0 = -\frac{\pi}{2} \ , \tag{B.6}$$

$$-\omega_0 t_1 = 3\frac{\pi}{2} \ . \tag{B.7}$$

Solving for t_0 and t_1:

$$t_0 = \frac{M_{max}T_s}{4(M_{max} + 1)} \ , \tag{B.8}$$

$$t_1 = \frac{3M_{max}T_s}{4(M_{max} + 1)} = 3t_0 \ . \tag{B.9}$$

The Fourier coefficients can be found by:

$$a_m = \frac{2l_x}{T_s} \int_{-t_0}^{t_1} (1 + \sin \omega_0 t) \cos x_m t \; dt$$

$$= \frac{2l_x}{T_s} \left[\frac{\sin x_m t}{x_m} + \left(\frac{-\omega_0 \cos \omega_0 t \cos x_m t - x_m \sin \omega_0 t \sin x_m t}{\omega_0^2 - x_m^2} \right) \right]$$

$$= \frac{2l_x}{T_s} \left[\frac{\sin x_m t_1 + \sin x_m t_0}{x_m} + \frac{x_m(\sin x_m t_1 + \sin x_m t_0)}{\omega_0^2 - x_m^2} \right] \Big]_{-t_0}^{t_1}$$

$$= \frac{2l_x}{T_s x_m} \left[\sin 3x_m t_0 + \sin x_m t_0 + \frac{(\sin 3x_m t_0 + \sin x_m t_0)}{\dfrac{\omega_0^2}{x_m^2} - 1} \right] \qquad (B.10)$$

$$= \frac{l_x}{m\pi} \left[4 \sin x_m t_0 - 4 \sin^3 x_m t_0 + \frac{(4 \sin x_m t_0 - 4 \sin^3 x_m t_0)}{\dfrac{\omega_0^2}{x_m^2} - 1} \right]$$

$$= \frac{4l_x}{m\pi} \left[\left(1 + \frac{1}{\dfrac{\omega_0^2}{x_m^2} - 1} \right) \left(\sin x_m t_0 - \sin^3 x_m t_0 \right) \right]$$

$$= \frac{4l_x}{m\pi} \frac{(M_{max} + 1)^2}{(M_{max} + 1)^2 - m^2 M_{max}^2} \left(\sin x_m t_0 - \sin^3 x_m t_0 \right) \quad ,$$

and

$$b_m = \frac{2l_x}{T_s} \int_{-t_0}^{t_1} (1 + \sin \omega_o t) \sin x_m t \; dt$$

$$= \frac{2l_x}{T_s} \left[\frac{-\cos x_m t}{x_m} + \left(\frac{-x_m \sin \omega_o t \cos x_m t - \omega_o \cos \omega_o t \sin x_m t}{\omega_o^2 - x_m^2} \right) \right] \Big]_{-t_0}^{t_1}$$

$$= \frac{2l_x}{T_s} \left[\frac{\cos x_m t_0 - \cos x_m t_1}{x_m} + \frac{x_m (\cos x_m t_0 - \cos x_m t_1)}{\omega_o^2 - x_m^2} \right] \Big]_{-t_0}^{t_1}$$

$$= \frac{2l_x}{T_s x_m} \left[\cos x_m t_0 - \cos 3x_m t_0 + \frac{(\cos x_m t_0 - \cos 3x_m t_0)}{\dfrac{\omega_o^2}{x_m^2} - 1} \right] \qquad (B.11)$$

$$= \frac{l_x}{m\pi} \left[4\cos x_m t_0 - 4\cos^3 x_m t_0 + \frac{(4\cos x_m t_0 - 4\cos^3 x_m t_0)}{\dfrac{\omega_o^2}{x_m^2} - 1} \right]$$

$$= \frac{4l_x}{m\pi} \left[\left(1 + \frac{1}{\dfrac{\omega_o^2}{x_m^2} - 1} \right) (\cos x_m t_0 - \cos^3 x_m t_0) \right]$$

$$= \frac{4l_x}{m\pi} \frac{(M_{max} + 1)^2}{(M_{max} + 1)^2 - m^2 M_{max}^2} (\cos x_m t_0 - \cos^3 x_m t_0) \quad .$$

Finally, the magnitude of the mth harmonic can be found by squaring a_m and b_m and then taking the square root of the sum:

$$c_m = \sqrt{a_m{}^2 + b_m{}^2}$$

$$= \frac{4l_x}{m\pi} \left(\frac{(M_{max} + 1)^2}{(M_{max} + 1)^2 - m^2 M_{max}{}^2} \right) \sqrt{\cos^2 x_m t_0 - \cos^4 x_m t_0}$$

$$= \frac{4l_x}{m\pi} \left(\frac{(M_{max} + 1)^2}{(M_{max} + 1)^2 - m^2 M_{max}{}^2} \right) \frac{\sqrt{1 - \cos 4 x_m t_0}}{2\sqrt{2}} \qquad (B.12)$$

$$= \frac{\sqrt{2}\, l_x}{m\pi} \left(\frac{(M_{max} + 1)^2}{(M_{max} + 1)^2 - m^2 M_{max}{}^2} \right) \sqrt{1 - \cos^2 \frac{2m M_{max}\pi}{M_{max} + 1}}$$

$$= \left| \frac{2l_x}{m\pi} \left(\frac{(M_{max} + 1)^2}{(M_{max} + 1)^2 - m^2 M_{max}{}^2} \right) \frac{\sin m M_{max}\pi}{M_{max} + 1} \right| \quad .$$

Note that the above relations are valid only for $\omega_o \neq x_m$; otherwise, if $\omega_o = x_m$ then a_m, b_m, and c_m need to be modified to:

$$a_m = \frac{2l_x}{T_s} \int_{-t_0}^{t_1} (1 + \sin \omega_o t) \cos \omega_o t \quad dt$$

$$= \frac{2l_x}{T_s} \left(\frac{\sin \omega_o t}{\omega_o} + \frac{\sin^2 \omega_o t}{\omega_o} \right) \Big]_{-t_0}^{t_1} \qquad (B.13)$$

$$= 0 \quad ,$$

and

$$b_m = \frac{2I_x}{T_s} \int_{-t_0}^{t_1} (1 + \sin \omega_0 t) \sin \omega_0 t \quad dt$$

$$= \frac{2I_x}{T_s} \left(\frac{\cos \omega_0 t}{\omega_0} + \frac{t}{2} - \frac{\sin 2\omega_0 t}{4\omega_0} \right) \left. \right]_{-t_0}^{t_1}$$

$$= \frac{2I_x}{T_s} \frac{t_1 + t_0}{2}$$

$$= I_x \frac{M_{max}}{M_{max} + 1} \qquad . \tag{B.14}$$

Therefore, c_m is:

$$c_m = I_x \frac{M_{max}}{M_{max} + 1} \qquad . \tag{B.15}$$

The final form of the Fourier coefficients for the raised sine wave represented by $f(t)$ in

equation (B.1) can be written as:

$$c_m = \begin{cases} \left| \dfrac{2I_x}{m\pi} \dfrac{(M_{max} + 1)^2}{(M_{max} + 1)^2 - m^2 M_{max}^2} \sin\left(\dfrac{m\pi M_{max}}{M_{max} + 1} \right) \right| & m \neq \dfrac{M_{max} + 1}{M_{max}} \\[4ex] I_x \dfrac{M_{max}}{M_{max} + 1} & m = \dfrac{M_{max} + 1}{M_{max}} \end{cases} \qquad . \tag{B.16}$$

Appendix C

Derivation of the Fourier Coefficients for the Flyback ZVS-QRC

Section 4.4 showed the input current of the flyback converter (Fig. 4.1) to be:

$$I'_{in}(t) = \frac{1}{n} \cdot \begin{cases} 0 & T_{01} < t < 0 \\ -I_x + I_x \cos \omega_o t & 0 < t < T_{12} \\ I_x(\cos \alpha - 1) + y(t - T_{12}) & T_{12} < t < T_{12} + T_{23} \\ 0 & T_{12} + T_{23} < t < T_s + T_{01} \end{cases} \quad , \quad (C.1)$$

where

$$T_{01} < 0 \quad . \tag{C.2}$$

The Fourier coefficients, a_m and b_m, are defined so that a function $f(t)$ can be written as a collection of sine and cosine terms. Mathematically this can be expressed as [10]:

$$f(t) = \sum_{m=0}^{\infty} a_m \cos x_m t + b_m \sin x_m t \quad . \tag{C.3}$$

It can be shown [10], that for this equation to be valid, a_m and b_m must be defined as:

$$a_m = \frac{2}{T_s} \int^{T_s} f(t) \cos(x_m t) dt \quad m = 0, 1, 2, \ldots \tag{C.4}$$

$$b_m = \frac{2}{T_s} \int^{T_s} f(t) \sin(x_m t) dt \quad m = 0, 1, 2, \ldots \tag{C.5}$$

In the above equations, the following relation holds:

$$x_m = 2m\pi f_s \quad . \tag{C.6}$$

Equations (C.4) and (C.5) yield the Fourier coefficients of the input current if $f(t) = I'_{in}(t)$. Substituting the representation of I'_{in} ((C.1)) for $f(t)$ in (C.4) and (C.5) and integrating over one switching period (T_{01} to $T_s + T_{01}$) will give:

$$a_m = \frac{2}{T_s} (g_{a1} + g_{a2}) \quad , \tag{C.7}$$

$$b_m = \frac{2}{T_s} (g_{b1} + g_{b2}) \quad , \tag{C.8}$$

where

$$g_{a1} = \int_0^{T_{12}} (-I_x + I_x \cos \omega_o t) \cos x_m t \, dt \quad , \tag{C.9}$$

$$g_{a2} = \int_{T_{12}}^{T_A} [I_x(\cos\alpha - 1) + y(t - T_{12})] \cos t \, dt \quad , \tag{C.10}$$

$$g_{b1} = \int_0^{T_{12}} (-I_x + I_x \cos\omega_0 t) \sin x_m t \, dt \quad , \tag{C.11}$$

$$g_{b2} = \int_{T_{12}}^{T_A} [I_x(\cos\alpha - 1) + y(t - T_{12})] \sin x_m t \, dt \quad . \tag{C.12}$$

Also, T_A is defined as:

$$T_A = T_{12} + T_{23} \quad . \tag{C.13}$$

Solving for g_{a1}:

$$g_{a1} = -\frac{I_x}{x_m}\sin x_m t + \frac{I_x}{2}\left[\frac{\sin(\omega_o - x_m)t}{(\omega_o - x_m)} + \frac{\sin(\omega_o + x_m)t}{(\omega_o + x_m)}\right]\Bigg]_0^{T_{12}}$$

$$= -\frac{I_x}{x_m}\sin x_m T_{12} + \frac{I_x}{2}\left[\frac{\sin(\omega_o - x_m)T_{12}}{(\omega_o - x_m)} + \frac{\sin(\omega_o + x_m)T_{12}}{(\omega_o + x_m)}\right]$$

$$= -\frac{I_x}{x_m}\sin x_m T_{12}$$

$$+ \frac{I_x}{2(\omega_o^2 - x_m^2)}\left[(\omega_o + x_m)\sin(\omega_o - x_m)T_{12} + (\omega_o - x_m)\sin(\omega_o + x_m)T_{12}\right]$$

$$= -\frac{I_x}{x_m}\sin x_m T_{12}$$

$$+ \frac{I_x}{2(\omega_o^2 - x_m^2)}\left[(\omega_o + x_m)(\sin \omega_o T_{12}\cos x_m T_{12} - \cos \omega_o T_{12}\sin x_m T_{12})\right]$$

$$+ \frac{I_x}{2(\omega_o^2 - x_m^2)}\left[(\omega_o - x_m)(\sin \omega_o T_{12}\cos x_m T_{12} + \cos \omega_o T_{12}\sin x_m T_{12})\right]$$

$$= -\frac{I_x}{x_m}\sin x_m T_{12}$$

$$+ \frac{I_x}{(\omega_o^2 - x_m^2)}\left[\omega_o \sin \omega_o T_{12}\cos x_m T_{12} - x_m \cos \omega_o T_{12}\sin x_m T_{12}\right]$$

$$= -\frac{I_x}{x_m}\sin x_m T_{12}$$

$$+ \frac{I_x}{x_m\left(\dfrac{\omega_o^2}{x_m^2} - 1\right)}\left[\frac{\omega_o}{x_m}\sin \omega_o T_{12}\cos x_m T_{12} - \cos \omega_o T_{12}\sin x_m T_{12}\right] \quad .$$

$$(C.14)$$

Solving for g_{a2}:

$$g_{a2} = \left[\frac{I_x(\cos\alpha - 1) - yT_{12}}{x_m} \right] \sin(x_m t) + y \left[\frac{\cos x_m t}{x_m^2} + \frac{t \sin x_m t}{x_m} \right] \Big]_{T_{12}}^{T_A}$$

$$= \left[\frac{I_x(\cos\alpha - 1) - yT_{12}}{x_m} \right] (\sin x_m T_A - \sin x_m T_{12})$$

$$+ \frac{y}{x_m} \left[\frac{\cos x_m T_A - \cos x_m T_{12}}{x_m} + T_A \sin x_m T_A - T_{12} \sin x_m T_{12} \right]$$

$$= \left[\frac{I_x(\cos\alpha - 1)}{x_m} \right] (\sin x_m T_A - \sin x_m T_{12})$$

$$+ \frac{yT_{23}}{x_m} \sin x_m T_A + \frac{y}{x_m^2} (\cos x_m T_A - \cos x_m T_{12}) \quad .$$

<div align="right">(C.15)</div>

Solving for g_{b1}:

$$
\begin{aligned}
g_{b1} &= \frac{I_x}{x_m} \cos x_m t + \frac{I_x}{2}\left[-\frac{\cos(x_m - \omega_o)t}{(x_m - \omega_o)} - \frac{\cos(\omega_o + x_m)t}{(\omega_o + x_m)} \right] \Bigg]_0^{T_{12}} \\
&= \frac{I_x}{x_m}(\cos x_m T_{12} - 1) + \frac{I_x}{2}\left[\frac{\cos(\omega_o - x_m)T_{12} - 1}{(\omega_o - x_m)} - \frac{\cos(\omega_o + x_m)T_{12} - 1}{(\omega_o + x_m)} \right] \\
&= \frac{I_x}{x_m}(\cos x_m T_{12} - 1) \\
&\quad + \frac{I_x}{2(\omega_o^2 - x_m^2)}\left[(\omega_o + x_m)(\cos(\omega_o - x_m)T_{12} - 1) \right. \\
&\qquad\qquad \left. - (\omega_o - x_m)(\cos(\omega_o + x_m)T_{12} - 1) \right] \\
&= \frac{I_x}{x_m}(\cos x_m T_{12} - 1) \\
&\quad + \frac{I_x}{2(\omega_o^2 - x_m^2)}\left[(\omega_o + x_m)(\cos \omega_o T_{12} \cos x_m T_{12} + \sin \omega_o T_{12} \sin x_m T_{12} - 1) \right] \\
&\quad - \frac{I_x}{2(\omega_o^2 - x_m^2)}\left[(\omega_o - x_m)(\cos \omega_o T_{12} \cos x_m T_{12} - \sin \omega_o T_{12} \sin x_m T_{12} - 1) \right] \\
&= \frac{I_x}{x_m}(\cos x_m T_{12} - 1) \\
&\quad + \frac{I_x}{(\omega_o^2 - x_m^2)}\left[x_m \cos \omega_o T_{12} \cos x_m T_{12} + \omega_o \sin \omega_o T_{12} \sin x_m T_{12} - x_m \right] \\
&= \frac{I_x}{x_m}(\cos x_m T_{12} - 1) \\
&\quad + \frac{I_x}{x_m\left(\dfrac{\omega_o^2}{x_m^2} - 1 \right)}\left[\cos \omega_o T_{12} \cos x_m T_{12} + \frac{\omega_o}{x_m} \sin \omega_o T_{12} \sin x_m T_{12} - 1 \right] \;.
\end{aligned}
$$

$$(C.16)$$

Solving for g_{b2}:

$$g_{b2} = -\left[\frac{I_x(\cos\alpha - 1) - yT_{12}}{x_m}\right]\cos(x_m t) + y\left[\frac{\sin x_m t}{x_m^2} + \frac{t\cos x_m t}{x_m}\right]\Big]_{T_{12}}^{T_A}$$

$$= -\left[\frac{I_x(\cos\alpha - 1) - yT_{12}}{x_m}\right](\cos x_m T_A - \cos x_m T_{12})$$

$$+ \frac{y}{x_m}\left[\frac{\sin x_m T_A - \sin x_m T_{12}}{x_m} - T_A \cos x_m T_A + T_{12}\cos x_m T_{12}\right]$$

$$= -\left[\frac{I_x(\cos\alpha - 1)}{x_m}\right](\cos x_m T_A - \cos x_m T_{12})$$

$$- \frac{yT_{23}}{x_m}\cos x_m T_A + \frac{y}{x_m^2}(\sin x_m T_A - \sin x_m T_{12}) \quad .$$

$$(C.17)$$

Each term of (C.14)-(C.17) contains either an I_x or a y. Recall that:

$$I_x = \frac{M}{Q}\frac{V_g}{n}\frac{(1+M)}{Z_o} \quad , \qquad (C.18)$$

and,

$$y = \frac{V_g}{n}\frac{(1+M)}{Z_o}\omega_o \quad , \qquad (C.19)$$

Rewriting y in terms of I_x yields:

$$y = \frac{Q}{M}I_x\omega_o \quad . \qquad (C.20)$$

Using this relation in (C.15) and (C.17) (the only equations that contain y), gives new expressions for g_{a2} and g_{b2}:

$$g_{a2} = \left[\frac{I_x(\cos\alpha - 1)}{x_m} \right] (\sin x_m T_A - \sin x_m T_{12})$$

$$+ \frac{I_x}{x_m} \frac{Q}{M} \omega_o T_{23} \sin x_m T_A + \frac{I_x}{x_m^2} \frac{Q}{M} \omega_o (\cos x_m T_A - \cos x_m T_{12}) \quad ,$$

(C.21)

and

$$g_{b2} = -\left[\frac{I_x(\cos\alpha - 1)}{x_m} \right] (\cos x_m T_A - \cos x_m T_{12})$$

$$- \frac{I_x}{x_m} \frac{Q}{M} \omega_o \cos x_m T_A + \frac{I_x}{x_m^2} \frac{Q}{M} \omega_o (\sin x_m T_A - \sin x_m T_{12}) \quad .$$

(C.22)

Finally, the Fourier coefficients take the form:

$$a_m = \frac{I_x}{n} a'_m \quad ,$$

(C.23)

and

$$b_m = \frac{I_x}{n} b'_m \quad ,$$

(C.24)

where

$$m\pi a_m' = -\sin x_m T_{12}$$
$$+ \frac{1}{d_m}\left[\frac{\omega_o}{x_m}\sin \omega_o T_{12}\cos x_m T_{12} - \cos \omega_o T_{12}\sin x_m T_{12}\right]$$
$$+ (\cos\alpha - 1)(\sin x_m T_A - \sin x_m T_{12})$$
$$+ \frac{Q}{M}\omega_o T_{23}\sin x_m T_A + \frac{Q}{M}\frac{\omega_o}{x_m}(\cos x_m T_A - \cos x_m T_{12}) \quad,$$

$$(C.25)$$

and

$$m\pi b_m' = (\cos x_m T_{12} - 1)$$
$$+ \frac{1}{d_m}\left[\cos \omega_o T_{12}\cos x_m T_{12} + \frac{\omega_o}{x_m}\sin \omega_o T_{12}\sin x_m T_{12} - 1\right]$$
$$- \frac{Q}{M}\omega_o T_{23}\cos x_m T_A$$
$$- (\cos\alpha - 1)(\cos x_m T_A - \cos x_m T_{12})$$
$$+ \frac{Q}{M}\frac{\omega_o}{x_m}(\sin x_m T_A - \sin x_m T_{12}) \quad.$$

$$(C.26)$$

Also, note that the following substitution was made:

$$d_m = \frac{\omega_o^2}{x_m^2} - 1 \quad.$$

$$(C.27)$$

Derivation of the Fourier Coefficients for the Flyback ZVS-QRC

Bibliography

[1]   K. Liu, "High Frequency Quasi-Resonant Converter Techniques," Ph.D. Dissertation, Virginia Polytechnic Institute and State University, Blacksburg, Virginia, October, 1986.

[2]   V. Vorperian, "Design and Analysis of DC-to-DC Resonant Converters," Final report for The International Business Machines Corporation, Oswego, NY, under contract 85-0513-10 to VPI&SU, June, 1986.

[3]   K.Liu, F.C. Lee, "Resonant Switches: A Unified Approach to Improving Performances of Switching Converters," INTELEC 84, IEEE Publication 84CH2073-5, pp.344-359.

[4]   A.W. Lotfi, V. Vorperian, F.C. Lee, "Comparison of Stresses Quasi-Resonant and Pulse-Width-Modulated Converters," IEEE Power Electronics Specialists' Conference Record, pp. 403-413, 1988.

[5]   W.A. Tabisz, P. Gradzki, F.C. Lee, "Zero-Voltage-Switched Quasi-Resonant Buck and Flyback Converters- Experiments at 10 MHz," IEEE Power Electronics Specialists' Conference Record, 1987, pp. 403-413.

[6]   R.E. Tarter, *Principles of Solid-State Power Conversion.*   H.W. Sams & Co., Inc., Indianapolis, Indiana, 1985, pp. 329-466.

[7]   A.W. Lotfi, V. Vorperian, F.C. Lee, "Loss Analysis in PWM, Zero-Current-Switched and Zero-Voltage-Switched Converters," Sixth Annual Power Electronics Seminar Proceedings, pp. 106-114, 1988.

[8]   G. Chryss, *High-Frequency Switching Power Supplies: Theory and Design.* McGraw Hill Book Company, New York, 1984, pp. 1-40.

[9]   W.H. Beyer, *CRC Standard Mathematical Tables, 25th Edition.* CRC Press, Inc., Boca Raton, Florida, 1978, pp. 326-384.

[10]   W.E. Boyce, R.C. DiPrima, *Elementary Differential Equations and Boundary Value Problems.* John Wiley and Sons, New York, 1977, pp. 452-490.

[11]   K. Liu, R. Oruganti, F.C. Lee, "Resonant Switches: Topologies and Characteristics." IEEE Power Electronics Specialists Conference Record, pp. 106-116, 1985.

[12]   H.W. Ott, *Noise Reduction Techniques in Electrical Systems.* John Wiley and Sons, New York, 1988, pp. 1-30.

[13]   MathCAD Manual, MathSoft, Inc., Cambridge, MS, 1988.

[14]   R. Ridley, M. Jovanovic, W. Tabisz, E. Kvalheim, "Power Electronics Professional Seminar, Course 2 - Resonant Converters," Virginia Polytechnic Institute and State University, Blacksburg, Virginia, 1990.

[15]   C.D. McGillem, G.R. Cooper, *Continuous and Discrete Signal and System Analysis.* Holt, Rinehart and Winston, New York, 1984.

[16]   L.W. Couch, *Digital and Analog Communication Systems.* Macmillan Publishing Company, New York, 1987.

[17]   H.B. Killen, *Modern Electronic Communication Techniques.* Macmillan Publishing Company, New York, 1985.

[18]   G. Kennedy, *Electronic Communication Systems.* 3rd Edition, McGraw-Hill Book Company, New York, 1985.

[19]   W.A. Tabisz, "High Frequency Multi-Resonant Conversion Techniques," Ph.D. Dissertation, Virginia Polytechnic Institute and State University, Blacksburg, Virginia, September, 1990.

Vita

The author was born January 27, 1967, in Hatboro, Pennsylvannia. After graduating from J.P. Taravella High School in Coral Springs, Florida, he enrolled in the University of Florida (*Go Gators!*) in August, 1984. The author graduated with High Honors in December, 1988, with a B.S.E.E.

In January, 1989, he enrolled at Virgina Tech (*Go Hokies!*) to study Power Electronics at the Virginia Power Electronics Center (VPEC). He received his M.S.E.E. in January, 1991.